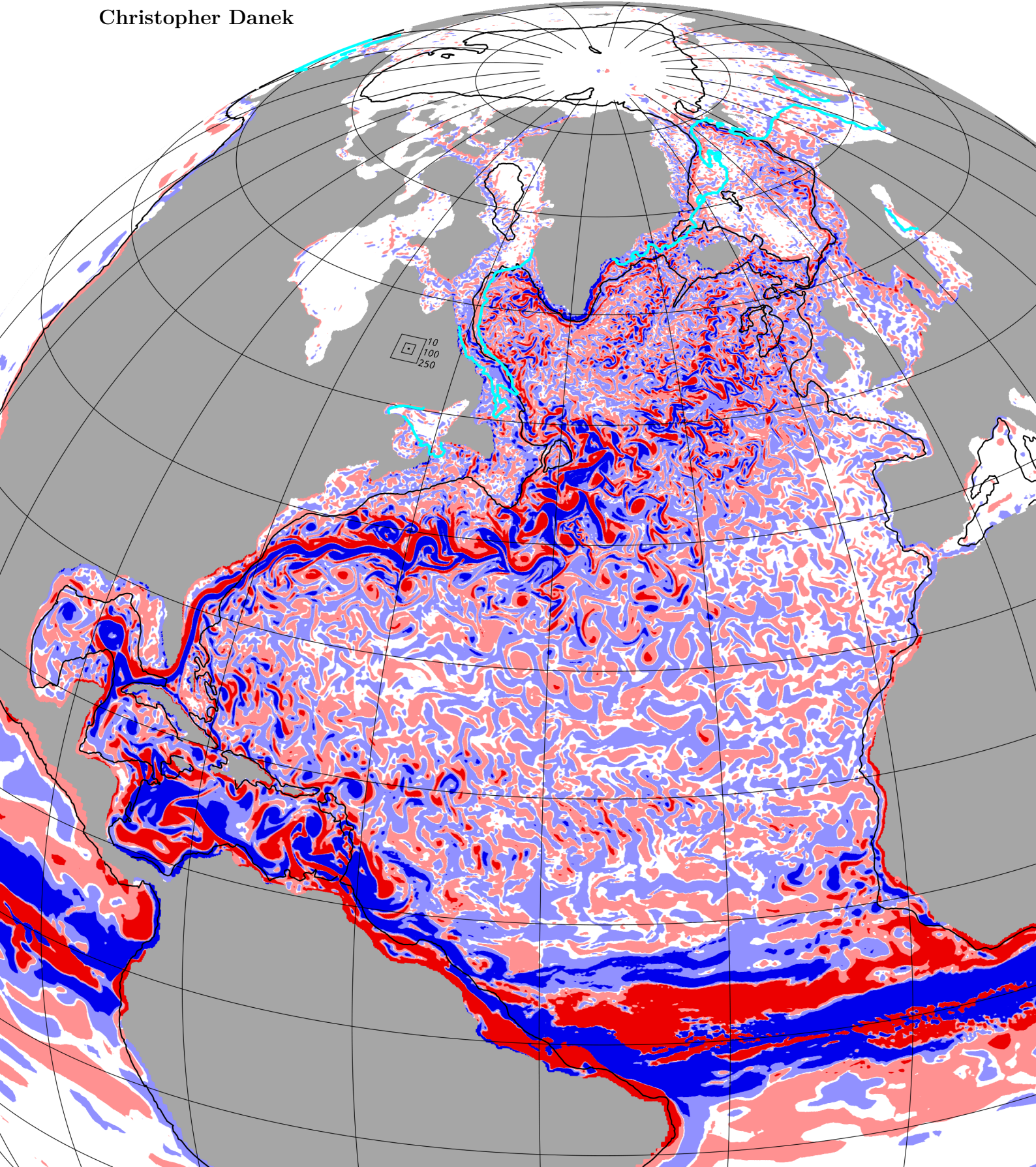


# Modeling the North Atlantic and Labrador Sea dynamics with the global high-resolution ocean model FESOM

Christopher Danek





# Modeling the North Atlantic and Labrador Sea dynamics with the global high-resolution ocean model FESOM

DISSERTATION

of

Christopher Danek

at the University of Bremen and  
the Alfred-Wegener-Institute for Polar and Marine Research

June 3, 2019

Reviewers: Prof. Dr. Gerrit Lohmann  
Prof. Dr. Sergey Danilov

Date of PhD defense: October 1, 2019



---

## Abstract

The subpolar regions of the North Atlantic ocean are crucial for the global climate in terms of deep water formation, which is a major driver for the Atlantic Meridional Overturning Circulation (AMOC) that transports heat into northern latitudes and returns cold deep water masses southward. The influence of a high horizontal resolution (5-15 km) on the general circulation and hydrography in the North Atlantic is investigated using the finite element sea ice-ocean model FESOM. A stronger shift of the upper ocean circulation and water mass properties during the model spinup is found in the high-resolution model version compared to the low-resolution ( $\sim 1^\circ$ ) control run. In quasi-equilibrium, the high-resolution model is able to reduce typical low-resolution model biases. Especially, it exhibits a weaker salinification of the North Atlantic subpolar gyre and a reduced mixed layer depth in the Labrador Sea. However, during the spinup adjustment, initially improved high-resolution features partially reduce over time: the strength of the Atlantic overturning and the path of the North Atlantic Current are not maintained, and hence hydrographic biases known from low-resolution ocean models return in the high-resolution quasi-equilibrium state. Long baroclinic Rossby waves are identified as a potential cause for the strong upper ocean adjustment of the high-resolution model. In addition, the high-resolution model is able to represent turbulent processes on the meso- and submesoscale within the Labrador Sea interior. Mesoscale eddies transport buoyant seawater into regions of strong convection, thereby contributing significantly to restratification. In particular, ageostrophic velocities associated with baroclinic instability were found to play a crucial role on length scales on the order of  $O(10)$  km. Until now, the dynamics on such scales were rarely modeled with a realistic global high-resolution ocean model in quasi-equilibrium.



# Contents

<b>1</b>	<b>Introduction</b>	<b>1</b>
1.1	Aims of this Study . . . . .	1
<b>2</b>	<b>Methods</b>	<b>3</b>
2.1	FESOMs Ocean Model Component . . . . .	3
2.1.1	Dynamic part . . . . .	4
2.1.2	Thermodynamic part . . . . .	7
2.1.3	Discretization . . . . .	10
2.1.4	Mesh refinement . . . . .	13
2.1.5	Model spinup strategy . . . . .	15
2.2	Atmospheric Forcing CORE-II . . . . .	16
2.2.1	Dynamic sea surface forcing . . . . .	17
2.2.2	Thermodynamic sea surface forcing . . . . .	20
2.3	Definition of modeled eddy fluxes . . . . .	25
2.4	Meridional overturning calculation on an irregular grid . . . . .	27
<b>3</b>	<b>Effects of high resolution and spinup time on the North Atlantic circulation</b>	<b>31</b>
3.1	General circulation . . . . .	31
3.2	Long Rossby Wave Propagation . . . . .	37
3.3	Hydrography . . . . .	39
3.4	Labrador Sea mixed layer restratification . . . . .	47
3.5	Discussion . . . . .	52
3.6	Conclusions . . . . .	56
<b>4</b>	<b>Decadal variability of eddy temperature fluxes in the Labrador Sea</b>	<b>59</b>
4.1	Labrador Sea eddy temperature fluxes . . . . .	59
4.1.1	Mean state . . . . .	60
4.1.2	Decadal variability . . . . .	64
4.2	Ambiguous salinity budget . . . . .	68
4.3	Discussion . . . . .	69
4.4	Conclusions . . . . .	72
<b>5</b>	<b>Eddy kinetic energy and mixed layer instabilities</b>	<b>73</b>
5.1	Wavenumber Spectrum of a limited area . . . . .	74
5.1.1	Spatial detrending . . . . .	74
5.1.2	One-dimensional wavenumber spectrum . . . . .	75
5.1.3	Modeled kinetic energy wavenumber spectra . . . . .	76
5.2	EKE variability . . . . .	78
5.3	Discussion . . . . .	81

*Contents*

---

5.4	Conclusions . . . . .	84
<b>6</b>	<b>Conclusions &amp; Outlook</b>	<b>85</b>
	<b>Bibliography</b>	<b>87</b>
	<b>Acknowledgments</b>	<b>107</b>

# 1 Introduction

Numerical climate models operate on increasingly finer grid sizes as the performance of parallelized super computers increases. Whether a model can represent a geophysical process depends on the model formulation and discretization. Since the spatial scale of oceanic eddies is on the order of  $O(1-100)$  km (first baroclinic Rossby radius of deformation  $\lambda_{R,1}$ , [Chelton et al., 1998](#)), the ocean model grid resolution needs to be on the same order to represent these ubiquitous small-scale features ([Chelton et al., 2011](#)). Alternatively, their effects must be parameterized. This is necessary as in state-of-the-art general circulation models (GCMs) the oceanic components run on horizontal resolutions of  $\sim 1^\circ$  (e.g., [Han et al., 2016](#)).

Furthermore, a spinup is necessary to let the model adjust from initial conditions towards its own dynamics. While the geostrophic adjustment as well as boundary and Kelvin wave adjustments occur after a few model days to years, long baroclinic Rossby wave basin-crossing travel times reach several decades at high latitudes ([Cherniawsky and Mysak, 1989](#); [Chelton and Schlax, 1996](#)). Moreover, the deep ocean adjustment needs several thousand model years to reach a quasi-equilibrium state because of the slow diffusion of active tracers ([Danabasoglu et al., 1996](#); [McWilliams, 1998](#)). Due to the high computational costs, many high-resolution ocean modeling studies have much shorter simulation lengths on the order of  $O(1-20)$  years ([Treguier et al., 2005](#); [Bryan et al., 2007](#); [Rattan et al., 2010](#); [Talandier et al., 2014](#); [Marzocchi et al., 2015](#); [Dupont et al., 2015](#); [Hewitt et al., 2016](#); [Iovino et al., 2016](#)).

However, low-resolution model deficiencies such as a too weak overturning, incorrect current pathways or hydrographic biases are partially corrected using a high horizontal model resolution (e.g., [Hurlburt and Hogan, 2000](#); [Treguier et al., 2005](#); [Bryan et al., 2007](#); [Talandier et al., 2014](#); [Marzocchi et al., 2015](#)). On the other hand, incorrect circulation pathways, missing small-scale processes or an insufficient vertical model resolution lead to model biases such as a too saline subpolar gyre ([Treguier et al., 2005](#); [Brandt et al., 2007](#); [Chanut et al., 2008](#); [Rattan et al., 2010](#); [Xu et al., 2013](#); [Marzocchi et al., 2015](#)) as well as too deep mixed layer depths (MLDs) in the Labrador Sea ([Oschlies, 2002](#); [Fox-Kemper et al., 2008](#); [Danabasoglu et al., 2014, 2016](#); [Heuzé, 2017](#)).

## 1.1 Aims of this Study

In this study, the impact of a 5-15 km horizontal resolution on the modeled North Atlantic Ocean large-scale circulation and water mass structure is eval-

uated. The global finite element sea ice-ocean model FESOM (Danilov et al., 2004; Wang et al., 2014b) with the capability of a local mesh refinement is used. To achieve a quasi-equilibrium model state, the model is integrated for  $\sim 300$  model years. The combination of a high spatial resolution and a long model integration time opens the route to systematically study the effects of explicitly resolved features and the effect of spinup cycles on the large-scale circulation. The findings are presented in chapter 3.

Through the relatively high heat capacity of water, dynamic processes in the ocean such as convection or mixing are slow compared to similar processes in the atmosphere and are strongly affected by the rotation of the earth. The oceanic horizontal mesoscale ranges from tens to hundreds of km, close to the first baroclinic Rossby radius of deformation  $\lambda_{R,1}$  (McWilliams, 2008). At the same time, the length scale of maximum eddy growth rates is a function of  $\lambda_{R,1}$  (Stammer, 1997). That means that if an mesoscale eddy evolves in the ocean, its size is on the order of  $\lambda_{R,1}$ . This is an important implication for modeling mesoscale ocean dynamics since  $\lambda_{R,1}$  dictates the horizontal resolution of any ocean model with which ocean dynamics are approximated. How mesoscale eddies interact with the mean flow under enhanced forcing is investigated in chapter 4.

The vortices in the North Atlantic illustrated on the frontcover define a distinct regime of turbulence on which tracer variance is transported across spatial scales and finally dissipated via molecular diffusion. In the high-resolution model, the magnitude of the Rossby number  $Ro = \zeta |f|^{-1}$  is on the order of  $O(0.1-1)$  everywhere in the North Atlantic. Hence, the flow is all but laminar and the rotation of the flow  $\zeta$  is as equally important as the planetary vorticity  $f$ . In the low-resolution model, in contrast,  $Ro$  yields values much smaller than 0.1 in the North Atlantic interior. How energy is transported across the mesoscale and submesoscale regimes is analyzed in chapter 5.

In the following, the numerical ocean model FESOM and its boundary conditions are introduced, preceded by flow decomposition definitions. Finally, flux calculation aspects on an irregular grid are considered.

## 2 Methods

In this study the global finite element sea ice-ocean model (FESOM, [Danilov et al., 2004](#); [Wang et al., 2008](#)) version 1.4 of [Wang et al. \(2014b\)](#) is used in a locally eddy-resolving resolution in the North Atlantic (5-15 km, 61 vertical levels) and a  $\sim 1^\circ$  low-resolution control run (from 10-200 km, 39 vertical levels). The model code can be obtained via <https://fesom.de/models/fesom14>. FESOM consists of a dynamic-thermodynamic ocean and sea ice component. This study focuses on the ocean part, which is described in the next section. The sea ice model is presented in [Timmermann et al. \(2009\)](#).

The model is used in an ocean-only or stand-alone configuration. This means that an external atmosphere is used to force the ocean at the sea surface by momentum, mass and heat fluxes. Consequently, there are no dynamical feedbacks between the atmosphere and the ocean at every model time step. Additionally, for the initialization of the model, a global climatology of the ocean temperature and salinity is needed. Section 2.2 provides further details about the initialization and forcing data. In addition, definitions on flow composition and overturning calculation on an irregular grid are added in sections 2.3 and 2.4.

FESOM was successfully used for modeling the general oceanic circulation, variability of the North Atlantic deep-water formation rates and sea ice distribution ([Sidorenko et al., 2011](#); [Scholz et al., 2013, 2014](#)) as well as chlorophyll distributions (biogeochemical coupling, [Schourup-Kristensen et al., 2014](#)). FESOMs local mesh refinement allows for a realistic modeling of water mass properties in domains with high complexity including small spatial scales e.g. Fram Strait ([Ionita et al., 2016](#)), the Canadian Arctic Archipelago ([Wekerle et al., 2013](#)), Greenland ([Wang et al., 2012](#)) or the Ross Sea ([Wang et al., 2010](#)).

### 2.1 FESOMs Ocean Model Component

The governing equations of the ocean model component are split into two parts not to solve nonlinear dynamics and thermodynamics simultaneously ([Danilov et al., 2004](#)). In the next section the model strategy is summarized following [Danilov et al. \(2004\)](#), [Wang \(2007\)](#) and [Wang et al. \(2008, 2014b\)](#).

*Declaration: parts of this section were published in [Danek et al. \(2019\)](#).*

### 2.1.1 Dynamic part

The model performs in a three-dimensional space  $\Omega$  with an upper boundary  $\Gamma_s$  (the free surface), a lower boundary  $\Gamma_b$  (the seafloor) and closed ( $\Gamma_n$ , vertical walls) and open ( $\Gamma_o$ ) lateral boundaries such that the boundary  $\partial\Omega = \Gamma_s \cup \Gamma_b \cup \Gamma_n \cup \Gamma_o$  (Fig. 2.1). The vertical thickness  $D$  of the water column is defined as the sum of the horizontally varying depth  $H(x, y)$  and the free surface height or elevation  $\eta(x, y, t)$  which changes in both horizontal space and time, yielding  $D(x, y, t) = H(x, y) + \eta(x, y, t)$ . That means that the rigid-lid approximation,  $\partial_t \eta = 0$ , is not applied ( $\partial_t$  is short hand for the partial derivative in time  $\frac{\partial}{\partial t}$ ). The vertical coordinate  $z$  is defined such that  $z = 0$  at the sea surface  $\Gamma_s$  when the ocean is at rest and  $z = \eta$  otherwise.  $z = -H$  at the bottom  $\Gamma_b$ . Within this domain, FESOM solves differential equations for several prognostic variables, from whose additional variables are diagnosed from.

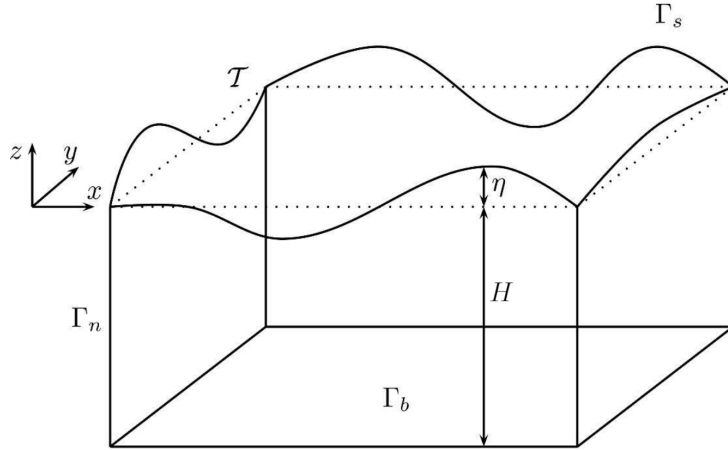


**Figure 2.1:** FESOMs three-dimensional model domain  $\Omega$  bounded by the seafloor  $\Gamma_b$ , the free sea surface  $\Gamma_s$  and lateral walls  $\Gamma_n$ . When the sea surface is not perturbed, i.e. when the ocean is at rest,  $\eta = z = 0$  as denoted by  $\mathcal{T}$  (dotted lines). Modified from [White et al. \(2008\)](#).

The first prognostic variable that is calculated in the dynamical part of the model is the ocean pressure  $p$  (in Pa =  $\text{kg m}^{-1} \text{s}^{-2}$  or dbar =  $10^4$  Pa).  $p$  is determined under the common approximation that vertical water parcel accelerations due to vertical pressure variations as well as the vertical component of the planetary vorticity are neglected (hydrostatic balance or relation, [Marshall](#)

et al., 1997). As a consequence, the vertical component of the Navier Stokes or momentum equation for a unit volume water parcel reduces to

$$\partial_z p = -g\rho \quad (2.1)$$

and vertical integration from  $z = 0$  to the ocean floor ( $z = -H$ ) yields  $p$  with the upper boundary condition  $p = 0$  on  $\Gamma_s$  ( $g$  is the gravitational acceleration in  $\text{m s}^{-2}$  and in the model  $\rho$  is implemented as the deviation from a mean density  $\rho_0$ ).

In the next step, the acceleration of the horizontal velocity component,  $\partial_t \mathbf{u}_h$ , of a unit volume water parcel is calculated by the horizontal Navier Stokes or momentum equation (from Danilov et al., 2004)

$$\partial_t \mathbf{u}_h = \underbrace{-\mathbf{u} \cdot \nabla \mathbf{u}_h}_1 - \underbrace{f \mathbf{k} \times \mathbf{u}_h}_2 - \underbrace{g \nabla_h \eta}_3 - \underbrace{\frac{1}{\rho_0} \nabla_h p}_4 + \underbrace{\nabla_h \cdot A_h \nabla_h \mathbf{u}_h}_5 + \underbrace{\partial_z A_v \partial_z \mathbf{u}_h}_6 \quad (2.2)$$

with the three-dimensional velocity vector of the ocean flow  $\mathbf{u} = \mathbf{i}u + \mathbf{j}v + \mathbf{k}w$  (in  $\text{m s}^{-1}$ ), unit vectors  $\mathbf{i}$ ,  $\mathbf{j}$ ,  $\mathbf{k}$  and the three-dimensional spatial differential operator  $\nabla = \mathbf{i}\partial_x + \mathbf{j}\partial_y + \mathbf{k}\partial_z$ .

This differential equation represents the balance between all forces acting on the water parcel (according to Newton's second law of motion) which are included in the model. Term 1 is the advection or transport of momentum. As the thermodynamic equation of state (section 2.1.2), this term introduces nonlinearities to the flow due to the product of the velocity component and its derivative. Term 2 arises due to the rotation of the earth with an angular frequency  $\omega = 2\pi \text{ (day)}^{-1}$ . The resulting inertial force is proportional to the Coriolis parameter  $f = 2\omega \sin \phi$  (in  $\text{s}^{-1}$ ) at latitude  $\phi$  (in  $^\circ$ ). The terms 3 and 4 yield horizontal velocity accelerations due to horizontal sea surface height and pressure gradients. For numerical stability in the presence of fast currents, term 5 introduces an anisotropic (larger in direction of fast flow) viscosity  $A_h$  (in  $\text{m}^2 \text{ s}^{-1}$ ) that reduces momentum. To keep this nonphysical momentum friction as small as possible, the biharmonic background value  $A_{h,0} = -3 \times 10^{13} \text{ m}^4 \text{ s}^{-1}$  is scaled that it 1) decreases with grid size to the third power ( $A_h = A_{h,0}$  at 100 km grid size), 2) doubles in a  $\pm 10^\circ$  latitude band around the equator, and 3) increases in regions of large horizontal shear (Smagorinsky, 1963; Wang, 2007; Wang et al., 2008). Similarly, term 6 applies a vertical viscosity  $A_v$  de-

rived by the KPP scheme in the thermodynamic part of the model (section 2.1.2).

Boundary conditions are necessary on all outer boundaries of  $\Omega$  to solve eq. 2.2:

$$\begin{aligned}
 A_v \partial_z \mathbf{u}_h &= \boldsymbol{\tau} && \text{on } \Gamma_s, \\
 A_v \partial_z \mathbf{u}_h + A_h \nabla_h H \cdot \nabla_h \mathbf{u}_h &= C_d \mathbf{u}_h |\mathbf{u}_h| && \text{on } \Gamma_b, \\
 \mathbf{u}_h \cdot \mathbf{n}_h &= 0 && \text{on } \Gamma_n, \\
 \mathbf{u}_h &= 0 && \text{on } \Gamma_n.
 \end{aligned} \tag{2.3}$$

The latter two imply that there is no flow normal and tangential (no-slip condition) to vertical walls with the outward pointing normal vector  $\mathbf{n}_h = \mathbf{i}n_x + \mathbf{j}n_y$ . At the sea surface, energy is introduced to the system by the horizontal wind stress vector  $\boldsymbol{\tau} = \rho_{\text{air}} C_D |\Delta \mathbf{u}_h| \Delta \mathbf{u}_h$  (in  $\text{kg m}^{-1} \text{s}^{-2}$ ) with  $\Delta \mathbf{u}_h$  as the difference between the horizontal components of the atmospheric wind velocity in 2 m height and the seawater velocity at  $z = 0$ .  $\rho_{\text{air}}$  is the air density and  $C_D$  the dimensionless atmosphere-ocean drag coefficient which increases with the horizontal wind velocity in a quadratic form (see Figure 1 and Section 2.1 of [Large and Yeager \(2004\)](#) and section 2.2). At the bottom, energy is dissipated by friction, parameterized by the bottom drag coefficient  $C_d = 0.0025$ . Since eq. 2.2 depends on the initially unknown horizontal velocity  $\mathbf{u}_h$  and sea surface height  $\eta$ , both are set to zero in the first model time step, i.e. when the model is initialized from rest.

In the next step the sea surface height  $\eta$  is calculated. For this, a seawater parcel with infinitesimal volume  $dV = dx dy dz$  (in  $\text{m}^3$ ) is considered. In the real world, the mass  $M$  (in kg) of that parcel is conserved, so that the material time derivative  $d/dt (dM) = d/dt (\rho dV) = 0$ . However, in FESOM (as in the most ocean models), the Boussinesq approximation yields the conservation of volume rather than mass and the mass continuity equation  $\partial_t \rho = -\nabla \cdot (\mathbf{u} \rho)$  (Section 4.2 of [Gill, 1982](#)) reduces to

$$\nabla \cdot \mathbf{u} = 0. \tag{2.4}$$

This simplification is due to very small dynamic horizontal density changes compared to the mean density  $\rho_0$  (on the order of 0.1%) and so the density  $\rho$  of a water parcel is taken as a constant (Section 9.3 of [Griffies and Adcroft, 2008](#)). Under this approximation, the modeled flow is non-divergent and a

change of the sea surface height  $\partial_t \eta$  is determined by depth-integration of 2.4, yielding

$$\partial_t \eta = -\nabla_{\mathbf{h}} \cdot \int_{z=-H}^{z=\eta} \mathbf{u}_{\mathbf{h}} \, dz + F_{FW}^{\text{lin. free surface}} = -\nabla_{\mathbf{h}} \cdot \int_{z=-H}^{z=0} \mathbf{u}_{\mathbf{h}} \, dz. \quad (2.5)$$

The terms  $\partial_t \eta$  and  $F_{FW}$  arise from the kinematic boundary conditions

$$\begin{aligned} w &= \partial_t \eta + \mathbf{u}_{\mathbf{h}} \cdot \nabla_{\mathbf{h}} \eta - F_{FW}^{\text{lin. free surface}} = \partial_t \eta && \text{on } \Gamma_s, \\ w &= -\mathbf{u}_{\mathbf{h}} \cdot \nabla_{\mathbf{h}} H && \text{on } \Gamma_b, \end{aligned} \quad (2.6)$$

where  $F_{FW}$  is the net freshwater volume flux per unit area due to precipitation (rain and snow), evaporation, river runoff and sea ice growth. Here, FESOM uses the linear free surface formulation which means that the sea surface height  $\eta$  can change in time with the volume of the discrete mesh kept constant (upper integration limit becomes 0 in 2.5). This arises through linearization of 2.5 based on the fact that  $\eta \ll H$  on climatic time scales (White et al., 2008). As a consequence,  $F_{FW}$  can not contribute directly to eq. 2.5 since this would induce a change in volume (Wang et al., 2014b). Instead,  $F_{FW}$  is added to the tendency equation of salinity (eq. 2.8) via the boundary condition 2.9 as a virtual salt flux (section 2.2.2).

The last dynamic model step is the derivation of the vertical velocity  $w$ . Since the modeled ocean flow is divergence-free (eq. 2.4),  $w$  is immediately given by vertical integration of eq. 2.4,

$$\partial_z w = \nabla_{\mathbf{h}} \cdot \mathbf{u}_{\mathbf{h}}, \quad (2.7)$$

with the kinematic boundary condition 2.6.

### 2.1.2 Thermodynamic part

The first thermodynamic model step is the calculation of the in-situ seawater density  $\rho(\theta, S_{\text{P}}, z)$  (in  $\text{kg m}^{-3}$ ) based on the potential temperature  $\theta$  (in  $^{\circ}\text{C}$ ) and practical salinity  $S_{\text{P}}$  (in  $\text{g kg}^{-1}$  or practical salinity units; psu) distribution by the equation of state (“EOS-80”, Fofonoff and Millard, 1983). Here,  $\theta$  is the temperature a seawater parcel would have if it was moved adiabatically from any depth  $z$  to the surface in order to remove the warming of the water parcel due to increased pressure with depth. The equation of state introduces

nonlinearities to the flow as does the horizontal advection term in eq. 2.2. This is due to diapycnal velocities (normal to lines of constant density) through e.g. cabbeling and thermobaricity (IOC et al., 2010). Note that although the EOS-80 seawater equations are deprecated and replaced by the “TEOS-10” equations (IOC et al., 2010, Intergovernmental Oceanographic Commission), the current FESOM version 1.4 still uses EOS-80. Section 2.2 provides details about the in-situ temperature  $T$  and  $S_p$  fields used to initialize the model run.

Then, the tendency for any tracer concentration  $C$  (of e.g. temperature  $T$  or salinity  $S$ ) is given by the advective and diffusive contributions (from Danilov et al., 2004)

$$\partial_t C = -\mathbf{u} \cdot \nabla C + \nabla_h \cdot K_h \nabla_h C + \partial_z K_v \partial_z C. \quad (2.8)$$

$K_h$  and  $K_v$  (in  $\text{m}^2 \text{s}^{-1}$ ) are horizontal and vertical diffusion coefficients and parameterize the dynamic effects of tracer mixing along isopycnals (“Redi diffusion”, Redi, 1982) and tracer advection due to adiabatic stirring (“GM”, an additional “bolus” velocity is added to the tracer equation, Gent and McWilliams, 1990). Since these processes occur on small spatial scales,  $K_h$  and  $K_v$  are also called eddy diffusivity coefficients. Both Redi diffusion and GM advection are formulated together as Griffies skew flux (Griffies, 1998; Griffies et al., 1998) with a background horizontal diffusion  $K_{h,0} = 1500 \text{ m}^2 \text{ s}^{-1}$  (see Section 2.9 of Wang (2007) for details about their implementation in FESOM). Boundary Conditions for  $C$  are given as

$$\begin{aligned} K_v \partial_z C &= -F_C && \text{on } \Gamma_s, \\ \nabla C \cdot \mathbf{n} &= 0 && \text{on } \Gamma_b \cup \Gamma_n. \end{aligned} \quad (2.9)$$

with the unit vector  $\mathbf{n}$  of the respective boundary. The thermodynamic surface fluxes  $F_C$  are described in section 2.2.2.

The horizontal tracer diffusivity  $K_h$  depends on the stability of the flow expressed by the Richardson Number  $Ri = N^2 [(\partial_z u)^2 + (\partial_z v)^2]^{-1}$  with the squared Brunt–Väisälä (or buoyancy) frequency  $N^2 = -g\rho^{-1} \partial_z \rho$ . In addition,  $K_h$  is scaled with the horizontal grid resolution. This scaling is limited by  $2 \text{ m}^2 \text{ s}^{-1}$  at the lower end and the background horizontal diffusion  $K_{h,0}$  above 50 km local horizontal resolution (Fig. 2.2). At grid resolutions on the order of  $O(1-10)$  km the obtained subgrid scale (SGS) flux is very small, but not disabled.

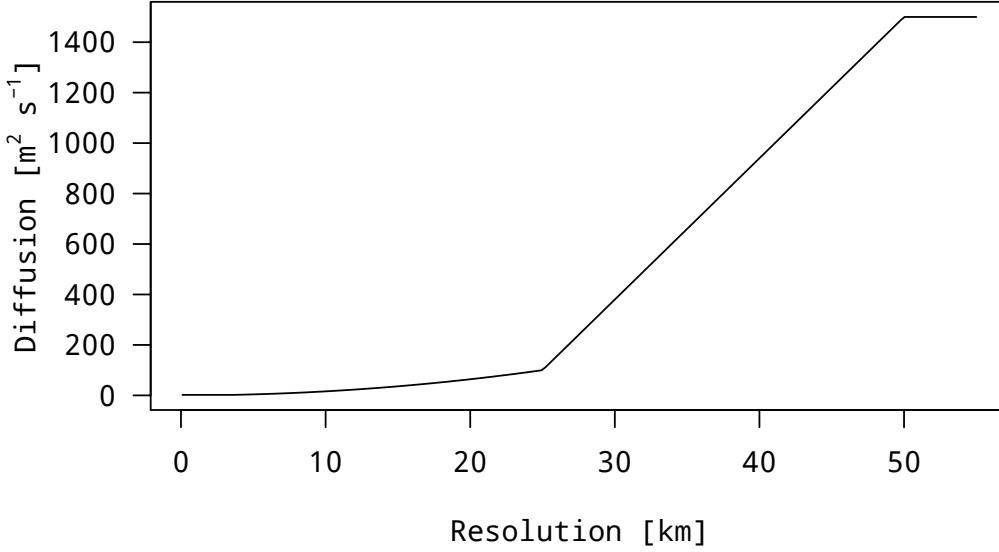


**Figure 2.2:** Scaling of Redi diffusion and GM advection with horizontal resolution (in km). The scaling is limited by  $2 \text{ m}^2 \text{ s}^{-1}$  at the lower end and the background horizontal diffusion  $K_{h,0} = 1500 \text{ m}^2 \text{ s}^{-1}$  above 50 km local horizontal resolution.

The vertical (diapycnal) mixing is implemented via the  $k$ -profile parameterization (“KPP”, Large et al., 1994). The idea behind this and most other vertical mixing parameterizations is to render the vertical turbulent (“eddy”) flux of any property  $x$  by the local property gradient, proportional to the vertical eddy diffusivity of that property  $K_v^x$ . This diffusion is assumed downgradient so that

$$\overline{w'x'} = -K_v^x \partial_z \bar{x} \stackrel{\text{KPP}}{=} -\hat{K}_v^x \partial_z (\bar{x} - \gamma_x), \quad (2.10)$$

where the overbars and primes denote the temporal mean and the deviation from that mean, respectively (see section 2.3 on how modeled eddy fluxes are defined in this study). Here,  $x$  can be any tracer (e.g.  $T$ ,  $S$ ) as well as momentum  $M$  and the last term of eq. 2.8 is implemented via this KPP formulation in FESOM.

The KPP vertical diffusivity coefficient  $\hat{K}_v^x$  is composed of boundary layer and interior diffusivities such that  $\hat{K}_v^x = f(\hat{K}_{v,\text{bl}}^x, \hat{K}_{v,\text{in}}^x)$ , where the former acts from the surface down to the depth to which boundary layer eddies can penetrate and the latter below that depth.  $\hat{K}_{v,\text{bl}}^x$  is defined via turbulent velocity scales distributed over the boundary layer via non-dimensional vertical shape functions. In our FESOM setup  $\hat{K}_{v,\text{bl}}^M \neq \hat{K}_{v,\text{bl}}^T = \hat{K}_{v,\text{bl}}^S$ . The interior contribution  $\hat{K}_{v,\text{in}}^x$  depends on 1) the stability of the flow ( $Ri$ ), 2) internal wave breaking and 3) double diffusion. In our model configuration, however, the double diffusion

contribution is disabled and in summary is  $\hat{K}_{v,\text{in}}^M \neq \hat{K}_{v,\text{in}}^T = \hat{K}_{v,\text{in}}^S$ . In addition, when  $x$  is a tracer such as temperature or salinity, a “nonlocal” transport term  $\gamma_x$  is added to eq. 2.10 that is non-zero in unstable (convective) situations and zero otherwise as well as for momentum ( $\gamma_M = 0$ , Large et al., 1994). As shown in a model study by Griffies et al. (2015, cyan lines in their Figure 12), the contribution of  $\gamma_T$  to the global vertical heat flux can be important in the upper part of the water column by transporting a part of the negative surface heat flux into the deeper cells of the boundary layer. As a consequence,  $\gamma_T$  cools the deeper levels of the boundary layer and warms the surface. Note that  $\gamma_T \neq \gamma_S$  since both depend on their respective surface fluxes provided by the atmospheric forcing (see section 2.2.2).

$A_v$  and  $\hat{K}_v^x$  are scaled from the background vertical viscosity  $A_{v,0} = 10^{-4} \text{ m}^2 \text{ s}^{-1}$  and diffusivity  $K_{v,0}$ . The latter increases from  $10^{-5} \text{ m}^2 \text{ s}^{-1}$  at the sea surface to  $10^{-4} \text{ m}^2 \text{ s}^{-1}$  at the ocean floor (see Figure 11 of Wang et al., 2014b). In case of static instability (high-density above low-density water) both coefficients equal  $1 \text{ m}^2 \text{ s}^{-1}$  to ensure a rapid mixing (convective adjustment). Vertical mixing due to tides as well as the shortwave radiation penetration module are disabled.

### 2.1.3 Discretization

In contrast to many other climate models, FESOM is spatially discretized on irregular sized triangles at the surface. These 2D triangles (“elements”) are repeated in the vertical direction ( $z$  coordinate) so that the 3D “nodes” (vertices of elements) have their horizontal position aligned with the surface nodes. The resulting prisms are cut into three tetrahedral elements, on which the model performs (Fig. 2.3 a and b). This spatial discretization allows an adjustable element size in regions of interest and along irregular terrain. Hence, an irregular “mesh“ can be constructed which is of great advantage for an ocean model due to the highly irregular structure of the ocean coast and floor. Also, no nesting of subdomains is necessary as FESOM meshes cover the global domain by default. However, this flexibility generally leads to higher numerical costs compared to FD methods (Danilov et al., 2005). The irregular meshes utilized in this study are described in section 2.1.4.

The obtained prismatic elements demand a non-standard way of numerical techniques. While most numerical ocean models approximate the introduced differential equations via finite differences (FD), FESOM utilizes a continuous

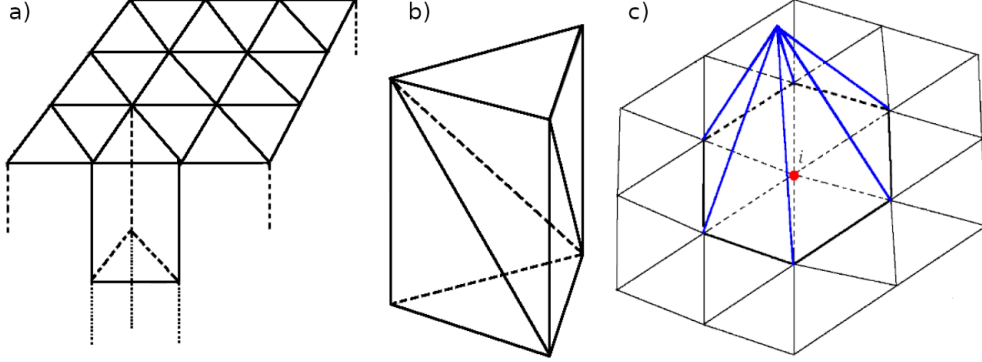


**Figure 2.3:** FESOMs irregular surface triangles (elements) are repeated in the vertical direction (a). Each of the obtained prisms is divided into three tetrahedral elements (b). A basis function equals 1 at node (or vertex)  $i$  and goes linearly to zero at neighboring horizontal and vertical vertices (blue lines in c). Modified from Wang et al. (2014b).

finite element (FE) approach with all variables placed at the nodes of an element ( $P_1 - P_1$  elements, i.e. polynomials of degree 1; Danilov, 2013). The FD equivalent would be an A-grid variable placement.

Now, following White et al. (2008), the procedure of the FE method is exemplarily described for the sea surface height  $\eta$ . First, a discrete approximation  $\Omega^h$  is chosen as a subspace of  $\Omega$  so that  $\partial\Omega^h = \Gamma_s^h \cup \Gamma_b^h \cup \Gamma_n^h \cup \Gamma_o^h$ . Then, eq. 2.5 is weighted by a "test-function"  $\tilde{\eta}$  and integrated over the  $\Gamma_s^n$  (since  $\eta$  is defined at the upper boundary only) such that

$$\int_{\Gamma_s^h} \left( \partial_t \eta + \nabla_h \cdot \int_{z=-H}^{z=0} \mathbf{u}_h dz \right) \tilde{\eta} d\tau = 0 \quad (2.11)$$

for all  $\tilde{\eta} \in \mathcal{H}$  where  $\mathcal{H}$  is a suitable functional space (e.g. Sobolev space, Wekerle, 2013) and  $\int d\tau$  is the two-dimensional integration over faces of the surface elements. Then, integration by parts of the divergence term yields

$$\int_{\Gamma_s^h} \left( \partial_t \eta \tilde{\eta} - \nabla_h \tilde{\eta} \cdot \int_{z=-H}^{z=0} \mathbf{u}_h dz \right) d\tau + \int_{\Gamma_n^h} \mathbf{u}_h \cdot \mathbf{n}_h \tilde{\eta} d\Gamma, \quad (2.12)$$

where  $\int d\Gamma$  is the two-dimensional integration over vertical faces of prisms. From the third boundary condition in 2.3 and the independence of  $\nabla_h \tilde{\eta}$  of  $z$  follows that

$$\int_{\Gamma_s^h} \partial_t \eta \tilde{\eta} d\tau - \int_{\Omega^h} \mathbf{u}_h \cdot \nabla_h \tilde{\eta} d\Omega = 0, \quad (2.13)$$

with the three-dimensional integration over prisms  $\int d\Omega$ . All  $\eta \in \mathcal{H}$ , that fulfill this variational form of 2.5, are considered weak solutions due to the use of  $\tilde{\eta}$ .

In the next step, "basis functions"  $\psi$  are defined which span a finite-dimensional subset  $\mathcal{H}^h$  of  $\mathcal{H}$ . Within  $\mathcal{H}^h$ , an approximation  $\eta^h$  of  $\eta$  is defined such that

$$\eta \simeq \eta^h = \sum_{i=1}^{n_\eta} \eta_i(t) \psi_i(x, y), \quad (2.14)$$

where  $\eta_i$  is the modeled sea surface height on node  $i \in (1, \dots, n_\eta)$  and since this is a two-dimensional variable,  $n_\eta$  equals the number of surface nodes of the irregular mesh (see section 2.1.4). In FESOM, the basis functions  $\psi$  are defined as continuous piecewise polynomials which equal 1 at node (or vertex)  $i$  and go linearly to zero at neighboring horizontal and vertical vertices (blue lines in Fig. 2.3 c).

Finally, the discrete variational form of the sea surface height equation 2.5 is obtained by the "Galerkin" method by substituting  $\eta$  with  $\eta^h$  and  $\tilde{\eta}$  with  $\psi$  in 2.13, yielding

$$\int_{\Gamma_s^h} \partial_t \eta^h \psi_i d\tau - \int_{\Omega^h} \mathbf{u}_h^h \cdot \nabla_h \psi_i d\Omega = 0, \quad (2.15)$$

for all  $i \in (1, \dots, n_\eta)$ . This equation yields a set of linear functions for the model values  $\eta_i$  at surface node  $i$ . In principle, the same procedure is applied to the momentum and tracer equations 2.2 and 2.8 to obtain  $\mathbf{u}_h^h$  and  $C^h$ , whose dimensions  $n_{\mathbf{u}_h}$  and  $n_C$  equal the number of 3D nodes of the irregular mesh.

The FE method comes with a number of additional necessary considerations in order to discretize the governing equations. For example, the vertical velocity  $w$  is solved column-by-column via the velocity potential  $\partial_z \Phi = w$ . This involves the vertical derivative which is defined in element-space and so  $w$  is approximated as the mean over neighboring elements. The horizontal momentum equation 2.2 is solved in several steps via an auxiliary velocity  $\mathbf{u}_h^*$  due to semi-implicit and implicit treatment of the Coriolis and vertical diffusion terms. Furthermore, numerous stabilization schemes are necessary to obtain a numerically stable solution. Danilov et al. (2004), Wang (2007) and Wang et al. (2008) provide details on these numerical aspects. The described procedure of FESOMs ocean model component and the wall clock time needed for each operation (based on 20 150 model time steps) is shown in Fig. 2.4.

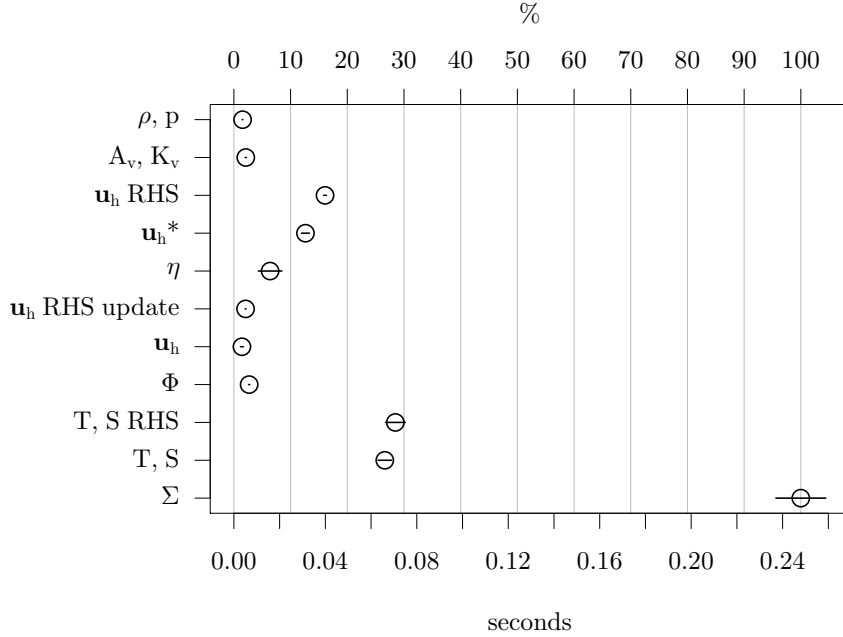


**Figure 2.4:** Operations of FESOMs ocean component in one model time step with the first operation in the top row and so on. Circles indicate each components average wall clock time in seconds (lower axis) and as % (upper axis) of the total time used by the ocean component (bottom row). Horizontal bars show  $\pm 1$  standard deviation ( $n_{\text{steps}} = 20\,150$ , the number of surface nodes of the used mesh  $n_{\text{n2D}} = 800\,260$  and  $n_{\text{CPU}} = 1\,920$ ). When the model is initialized,  $\rho$  is obtained from a  $T$  and  $S$  climatology and the dynamic components  $\mathbf{u}_h$  and  $\eta$  are set to zero. The model procedure is described in sections 2.1.1 and 2.1.2.

#### 2.1.4 Mesh refinement

In this study I used two different mesh configurations with locally refined resolutions (low- and high-resolution, Fig. 2.5). Both model grids have an increased resolution along the coastline and at the equator to ensure that oceanic currents along the coastline as well as coastal and equatorial upwelling processes can be adequately simulated. Furthermore, the low-resolution model mesh (Fig. 2.5 a) has an increased resolution in the northern hemispheric deep water formation areas and is described in Scholz et al. (2013, 2014).

The high-resolution model configuration (Fig. 2.5 b) features additionally increased resolution in the subpolar North Atlantic and in areas with 1) enhanced sea surface height (SSH) variability as measured by satellite altimeter data (AVISO), 2) steep bathymetric slopes based on ETOPO1 (Amante and

Eakins, 2009), and 3) high horizontal temperature gradients in 200 m depth (World Ocean Atlas 2013, Locarnini et al., 2013).

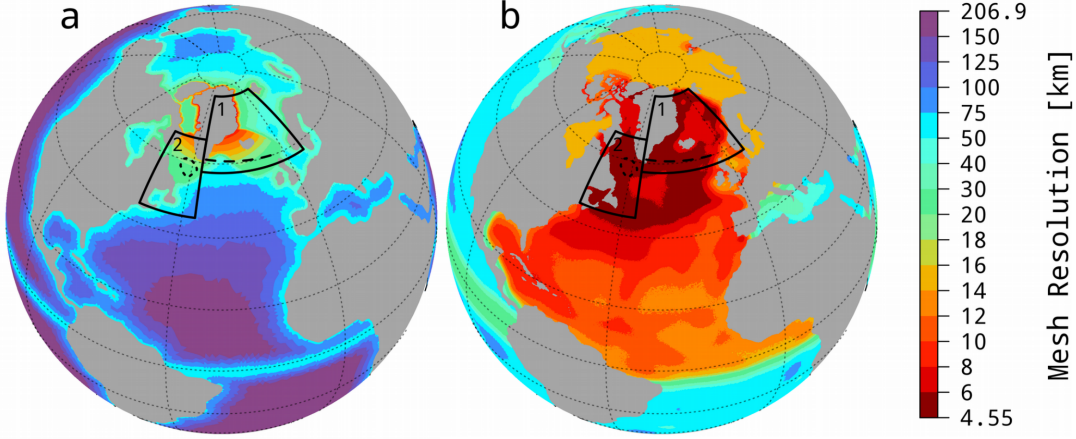


**Figure 2.5:** Horizontal mesh resolution (in km) of the low- (a) and high- (b) resolution models. The resolution is increased at the boundaries, the equator, in the subpolar gyre (a and b) and in areas of high SSH variability, steep bathymetry and high horizontal temperature gradients as detected by observations (b only, see methods). The two boxes show Nordic Sea (1) and Labrador Sea (2) areas for sea ice extent time series and the dashed lines mark the index area in the Labrador Sea and the  $\sim 60^\circ$  N cross section in the eastern North Atlantic.

This high-resolution mesh exhibits horizontal resolutions ( $\Delta_i = \sqrt{\sqrt{3} A_{e2D_i}}$  with the area  $A_{e2D_i}$  of 2D element  $i$ ) of  $\sim 10$  km along the North Atlantic coastline ( $\sim 5$  km along Greenland and Labrador), an increased resolution along the equator (from  $\sim 45$  km at  $10^\circ$  S to  $\sim 14$  km at  $20^\circ$  N) and a varying resolution of  $\sim 8$ - $15$  km in the subtropical gyre. The average resolution of the subpolar gyre is  $\sim 5$  km up to the Fram Strait.

**Table 2.1:** Characteristics of the two irregular FESOM meshes.

	Low	High
surface nodes	53 882	800 260
3D nodes	1 070 276	29 518 037
vertical $z$ levels	39	61
smallest $\Delta t$ (min)	30	10
CPUs	192	1 920

The Arctic Ocean is resolved by  $\sim 15$  km grid size. With this mesh configuration which has a resolution in the Atlantic that is close to the deformation radius of eddies we ensured that the model is able to resolve important oceanic currents along the coast line as well as energetic fronts. The model time step  $\Delta t$  is determined by the

smallest mesh element (see section 5.3 of Wang et al., 2018). Table 2.1 summarizes the main characteristics of the two utilized irregular meshes. In both models the vertical resolution is finer in the upper 200 meter to better resolve the boundary layer and becomes coarser with depth. The high-resolution model exhibits 61 vertical levels and therefore resolves the first baroclinic mode of the ocean (Stewart et al., 2017). In contrast, the low-resolution control model is discretized on 39 vertical levels, not capturing this mode. The depth intervals range from 10 to 300 m in the low- and from 10 to 150 m in the high-resolution model.

The influence of the irregular mesh refinement on the modeled SGS fluxes as described in section 2.1.2 becomes clear by comparing Fig. 2.5 with Fig. 2.6. The depth-integrated total horizontal SGS temperature flux is several orders of magnitude weaker when the high-resolution mesh is used, compared to the low-resolution mesh. In addition, areas of different dynamics may be identified. For example, the SGS flux is larger in the high-resolution western boundary current along the Greenland coast compared to the Labrador Sea interior, although the horizontal mesh resolution does not differ between these areas. It is rather the vertical shear associated with the fast boundary current that leads to higher SGS fluxes in this region through scaling by the Richardson number  $Ri$  (see section 2.1.2).

### 2.1.5 Model spinup strategy

Previous FESOM studies of Sidorenko et al. (2011); Wang et al. (2012); Scholz et al. (2013) have shown that a spinup time of 250-300 years is necessary to bring the upper and intermediate ocean into a quasi-equilibrium state. For that reason I performed five consecutive spinup cycles each with a length of 62 years in order to reach a quasi-equilibrium model state (310 years in total, monthly model output was saved). For each spinup cycle the last output of the preceding spinup was used as a new initialization as it is suggested in the CORE and CORE-II protocols (Griffies et al., 2012; Danabasoglu et al., 2014) and applied in other ocean modeling studies (Lohmann et al., 2009; Karspeck et al., 2017; He et al., 2016).

Hereafter, the performed model experiments are named L1, L2, ..., L5 and H1, H2, ..., H5 for the combination of the two model resolutions ('L'ow and 'H'igh, Fig. 2.5) and the number of the spinup cycle (1-5). If time average

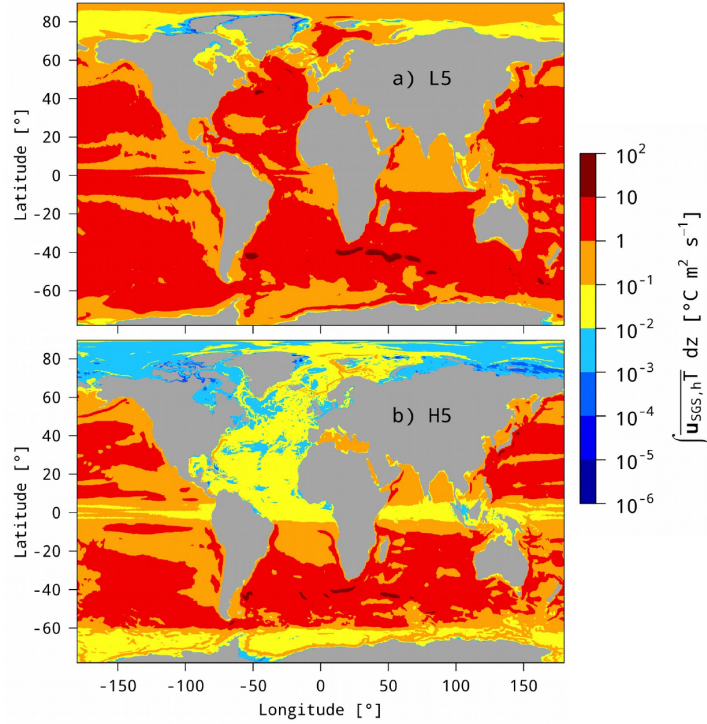


**Figure 2.6:** Norm of the average (1948-2009) depth-integrated total horizontal subgrid scale (SGS) temperature flux (in  $^{\circ}\text{C m}^2 \text{s}^{-1}$ ) of the low- (a) and high-resolution (b) models. The product of the eddy-induced velocity  $\mathbf{u}_{\text{SGS},h}$  and potential temperature  $T$  was calculated at every model time step (see section 2.3).

periods are not given explicitly, the whole spinup period 1948-2009 (62 years) is used.

## 2.2 Atmospheric Forcing CORE-II

The model runs were initialized from the Polar Science Center Hydrographic Climatology (PHC3, [Steele et al., 2001](#), temperature and salinity on  $1^{\circ}$  horizontal resolution and 33 depth levels). Sea surface fluxes for momentum and tracers (boundary conditions 2.3 and 2.9) were provided by the atmospheric re-analysis dataset "CORE-II" (Coordinated Ocean Research Experiments [Large and Yeager, 2009](#)) covering the period 1948-2009 on a T62 grid ( $\sim 1.875^{\circ}$  horizontal resolution). Among others, this forcing data was used in a model intercomparison by [Danabasoglu et al. \(2014\)](#) and [Danabasoglu et al. \(2016\)](#). CORE-II provides the following atmospheric variables:

- every six hours: horizontal wind direction and velocity (in  $\text{m s}^{-1}$ ), air temperature (in K) and specific humidity (in  $\text{kg kg}^{-1}$ ) at 10 m height
- every day: downward shortwave (or solar) and longwave radiation (in  $\text{W m}^{-2}$ )
- every month: rain and snow (in  $\text{kg m}^{-2} \text{ s}^{-1}$ )

In addition, the continental river runoff into the ocean is provided by a global  $1^\circ$  monthly climatology of Dai et al. (2009) (that means the runoff in January is the same for all modeled years). The next sections summarize the implementation of the forcing data into FESOM to obtain the dynamic and thermodynamic boundary conditions for the ocean model. Information about the sea ice model component can be found in Timmermann et al. (2009) and Wekerle (2013).

### 2.2.1 Dynamic sea surface forcing

Fig. 2.7 shows the average (1948-2009) atmospheric circulation pattern in the North Atlantic sector as well as the average winter (JFM) sea surface heat flux  $Q_{\text{net}}$  (in  $\text{W m}^{-2}$ , negative values indicate a heat loss of the ocean) for the low- and the high-resolution. A westerly geostrophic flow between a low pressure system over Greenland and a high pressure system over the subtropical North Atlantic gyre is the dominant atmospheric wind pattern. The center of the low ( $\sim 1000$  hPa) is located between the southern tip of Greenland and Iceland. During winter a heat transfer from the ocean to the atmosphere on the order of 100 to 200  $\text{W m}^{-2}$  occurs throughout the North Atlantic.

The largest heat loss occurs in the vicinity of the Gulf Stream, the Nordic Seas, the Irminger Sea and the Labrador Sea. On average, the latter loses more than 375  $\text{W m}^{-2}$  each winter. Generally, the obtained net surface heat fluxes of the low- and high-resolution models are similar. A notable exception is a warm spot around  $40^\circ$  W and  $45^\circ$  N, that is pronounced in the low- but absent in the high-resolution model. For illustration, the average (1979-2009) winter (JFM) sea ice extent (sea ice concentration  $> 15\%$ ) as observed (dashed, Cavalieri et al., 1996) and modeled (solid) is added as red lines. The interactions between the modeled surface circulation and sea ice are described in section 3.4.

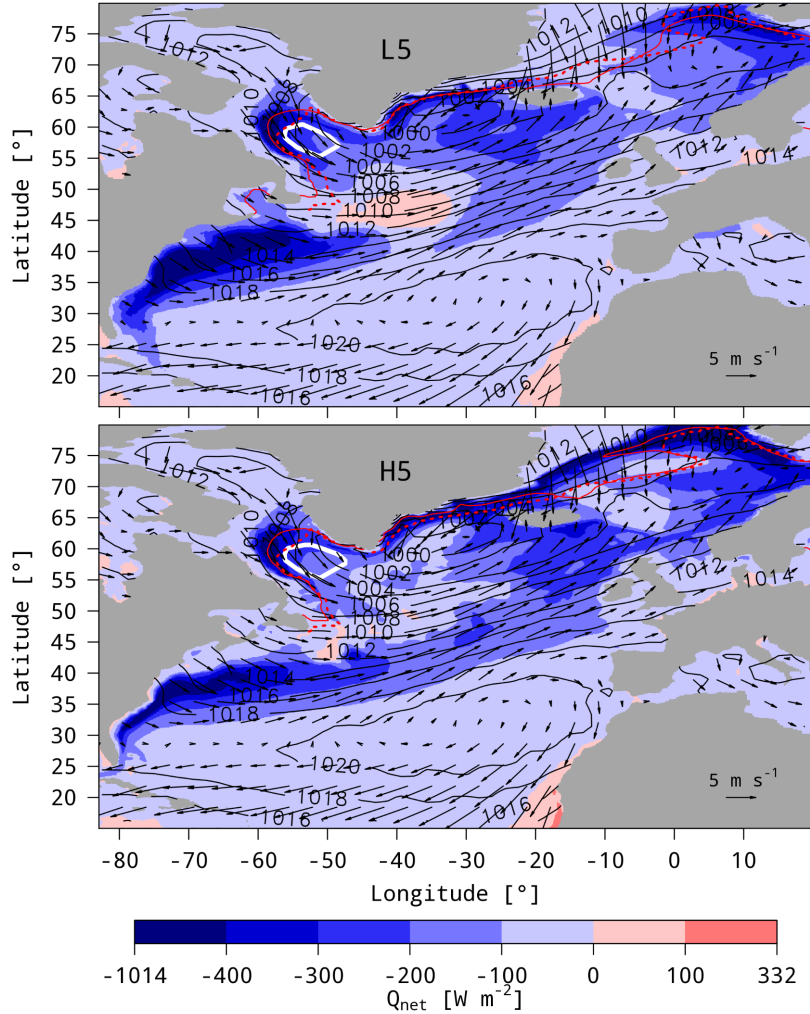


**Figure 2.7:** Average (1948-2009) winter (JFM) sea level pressure (in hPa, contours) and horizontal wind velocity (in  $\text{m s}^{-1}$ ) and direction (arrows) at the sea surface as provided by CORE-II (Large and Yeager, 2009) and applied to the low- (top) and high-resolution (bottom) models (5th spinup cycle). Colors show the average winter net sea surface heat flux  $Q_{\text{net}}$  derived by the bulk formulae of Large and Yeager (2004) (in  $\text{W m}^{-2}$ , negative values indicate a heat flux from the ocean to the atmosphere). The observed (Cavaleri et al., 1996) and modeled average (1979–2009) winter sea ice concentration of 15% is shown as dashed and solid red lines, respectively. White index areas show Labrador Sea interior regions.

Figure 2.8 a shows the 3-year low-pass filtered temporal evolution of the globally averaged horizontal wind velocity  $|\mathbf{u}_{\text{h,wind}}|$  at the sea surface for the 1st and 5th model spinup cycles after (i.e. model years 1–62 and 249–310). Since the wind forcing is the same in every cycle, there are no differences between the first and fifth spinup cycles in both models.

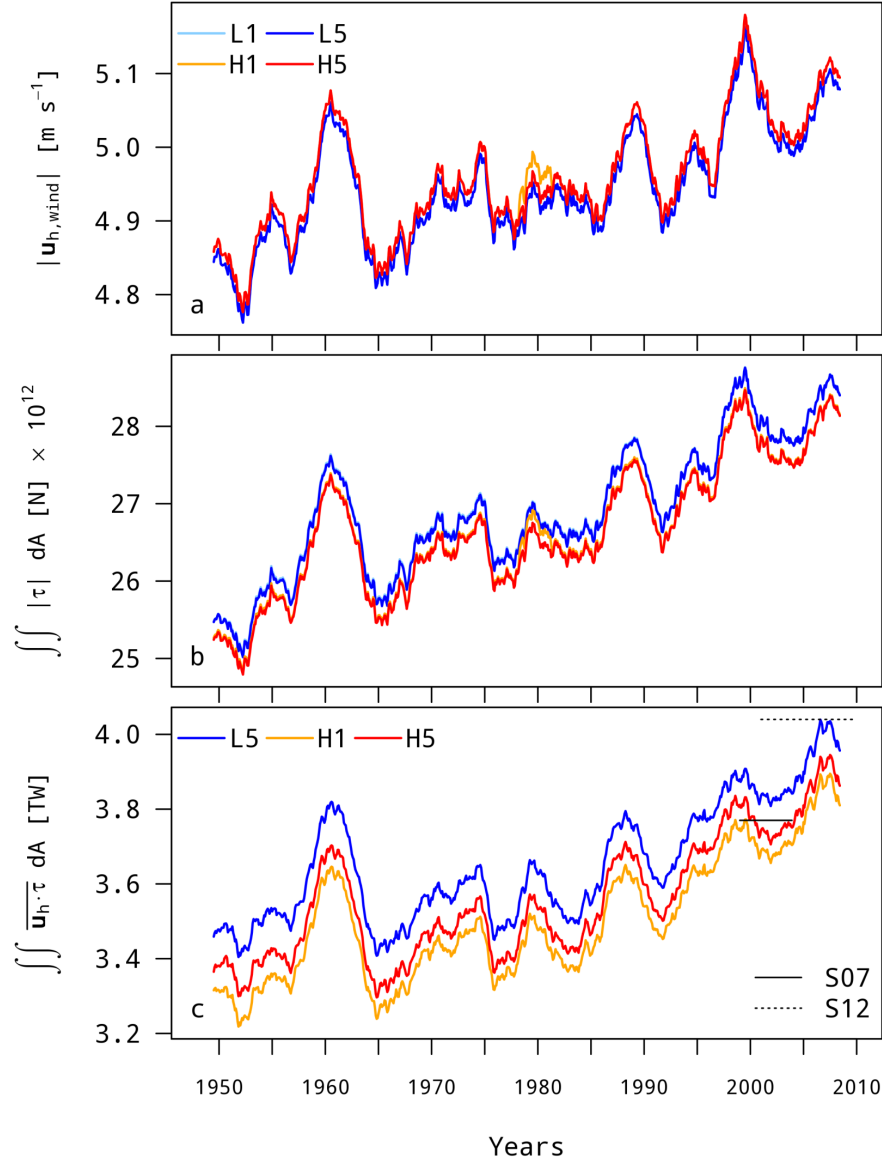


**Figure 2.8:** Globally averaged norm of horizontal wind velocity at the sea surface  $\mathbf{u}_{h,\text{wind}}$  (in  $\text{m s}^{-1}$ , a), globally integrated norm of wind stress  $\boldsymbol{\tau} = \rho_{\text{air}} C_D |\Delta \mathbf{u}_h| \Delta \mathbf{u}_h$  as implemented in FESOM (in  $10^{12}$  N, b) and global total kinetic energy input through the wind on the ocean surface circulation  $\overline{\mathbf{u}_h \cdot \boldsymbol{\tau}}$  (in PW, c, see section 2.3 for how a total flux is decomposed in a temporal mean and temporal varying eddy part) of the 1st and 5th spinup cycles of the low- (blue) and high- (red) resolution models. In c, black solid and dashed lines show estimates of the model studies of von Storch et al. (2007, 2012). All monthly time series are low pass filtered by a 3-year running mean.

The high-resolution model, however, exhibits differences between H1 and H5 around the year 1980. It is unclear to us what caused this deviation but the

effect on the model solution is likely to be small as indicated in Fig. 2.8 c. A spatial interpolation between the regular CORE-II grid and the irregular FESOM meshes is necessary to provide the atmospheric forcing at each corresponding ocean mesh node. Despite the large horizontal FESOM mesh resolution range from a few km up to a few hundred km, as well as the locally large differences between the fine FESOM mesh and the coarse CORE-II grid, the obtained wind forcing is very similar over the different low- and high-resolution setups (blue against red lines in Fig. 2.8 a).

The force that acts on the sea surface is modeled via the wind stress  $\boldsymbol{\tau}$  (defined in sec. 2.1.1) and provides momentum at the upper boundary via drag (see boundary condition 2.3). Fig. 2.8 b indicates the direct proportionality between  $\mathbf{u}_{h,\text{wind}}$  and the globally integrated  $\boldsymbol{\tau}$  as well as their similarity between the used FESOM meshes. The global total kinetic energy input through the wind on the general ocean surface circulation  $\overline{\mathbf{u}_h \cdot \boldsymbol{\tau}}$  is shown in Fig. 2.8 c. Here, the total flux of  $\boldsymbol{\tau}$  includes contributions from time scales ranging from the model time step  $\Delta t$  to months, the model output interval (see section 2.3 for how a total flux is decomposed in a temporal mean and temporal varying eddy part in this study). Note that the total  $\boldsymbol{\tau}$  flux was not saved in the first spinup of the low-resolution model (L1) and is therefore not shown. Again,  $\overline{\mathbf{u}_h \cdot \boldsymbol{\tau}}$  generally follows the atmospheric forcing  $\mathbf{u}_{h,\text{wind}}$ . The spinup adjustment leads to a slight increase of the high-resolution energy input from H1 to H5. Here, the anomaly in  $\mathbf{u}_{h,\text{wind}}$  between H1 and H5 was filtered out due to the interaction with the general ocean circulation. The total kinetic energy input is similar for both the low- and high-resolution models. The black solid and dashed lines in Fig. 2.8 c show similar global estimates of the modeling studies by von Storch et al. (2007) and von Storch et al. (2012) using, respectively, the ocean models OFES and MPI-OM with a  $0.1^\circ$  horizontal resolution and the NCEP/NCAR atmospheric forcing.

### 2.2.2 Thermodynamic sea surface forcing

Sea surface temperature and salinity fluxes determine the dynamically meaningful density field at the sea surface via the boundary condition 2.9. Temperature changes at the sea surface occur directly through a change in  $Q_{\text{net}}$ , the sum of the downwelling shortwave (or solar) and longwave radiation,  $Q_{S,\text{dn}}$  and  $Q_{L,\text{dn}}$  as well as turbulent sensible and latent heat fluxes  $Q_H$  and  $Q_E$  and the upwelling longwave radiation  $Q_{L,\text{up}}$  (all in  $\text{W m}^{-2}$ ,  $\text{W} = \text{kg m}^2 \text{s}^{-3}$ ). The

former two are provided by the CORE-II forcing and the latter were calculated using the bulk formulae following [Large and Yeager \(2004\)](#), yielding the sea surface temperature flux  $F_T$  as

$$F_T = \frac{1}{\rho c_p} (Q_{S,\text{dn}} + Q_{L,\text{dn}} + Q_H + Q_E + Q_{L,\text{up}}) = \frac{Q_{\text{net}}}{\rho c_p}. \quad (2.16)$$

Here,  $F_T$  is expressed as a heat flux in  $\text{K m s}^{-1}$  via sea surface density  $\rho$  and the specific heat capacity of sea water at constant pressure  $c_p$  (in  $\text{m}^2 \text{s}^{-2} \text{K}^{-1}$ ).

The sea surface salinity (SSS) only changes through the growth and decay of sea ice. A surface freshwater flux  $F_{FW}$ , in addition, changes the salt concentration of a sea water parcel through a volume change due to e.g. precipitation or evaporation. However, the Boussinesq approximation is applied (see section [2.1.1](#)) and a direct volume change is not allowed since the used FESOM mesh is constant in time and eq. [2.4](#) must hold true (an adaptive mesh whose surface elements may change in time was not used). Thus, freshwater effects on the salinity concentration are provided via a "virtual salinity" flux  $F_{VS}$  that adds a negative salinity to the right hand side (RHS) of the salinity equation [2.8](#) while conserving the volume. In this study, surface freshwater fluxes  $F_{FW}$  arise through precipitation  $P$  in form of rain and snow, evaporation  $E$  (all provided by CORE-II), continental river runoff  $R$  ([Dai et al., 2009](#)) and the growth or decay of sea ice  $G$  as provided by FESOMs sea ice model component (all in  $\text{m s}^{-1}$ ). These freshwater fluxes are converted to the virtual salt flux via

$$F_{VS}^* = S_{\text{ref}} (P + E + R + G) = S_{\text{ref}} F_{FW}, \quad (2.17)$$

where every freshwater component is defined such that it is positive if freshwater is added to the sea surface. Here, the reference sea surface salinity  $S_{\text{ref}}$  (in psu) is chosen to be the modeled SSS at the respective surface node. With this formulation, the local effect of freshwater on the SSS is captured. However, since  $S_{\text{ref}}$  is not a constant, the global integral of [2.17](#) is not necessarily zero even if the global integral of  $F_{FW}$  would be and global salt conservation may not be given ([Wang et al., 2014b](#)). Hence, the global mean of [2.17](#) is subtracted, yielding the corrected virtual salt flux

$$F_{VS} = F_{VS}^* - \frac{\int_{\Gamma_s} F_{VS}^* d\Gamma_s}{\int_{\Gamma_s} d\Gamma_s}. \quad (2.18)$$

In addition, a SSS relaxation (or restoring)  $F_{SR}$  towards the climatology with a typical piston velocity  $v_p = 50 \text{ m (300 days)}^{-1} \approx 1.93 \times 10^{-6} \text{ m s}^{-1}$  is applied for numerical stability, yielding

$$F_{SR}^* = v_p (S_{\text{clim}} - S). \quad (2.19)$$

If this unphysical term restoring is disabled, the SSS becomes unrealistically high at single nodes around Greenland (not shown), possibly due to missing sea ice-ocean interactions as noted in [Marsh et al. \(2010\)](#) (the restoring is largest in the presence of sea ice). The same correction as for the virtual salt flux is applied here:

$$F_{SR} = F_{SR}^* - \frac{\int_{\Gamma_s} F_{SR}^* d\Gamma_s}{\int_{\Gamma_s} d\Gamma_s}. \quad (2.20)$$

In summary, the upper boundary condition for the salinity tracer (in  $\text{psu m s}^{-1}$ , eq. 2.9) is given by the sum of the virtual salinity and salinity relaxation fluxes,

$$F_S = F_{VS} + F_{SR}. \quad (2.21)$$

Further details on how the turbulent fluxes as well as the sea ice contributions to the SSS forcing are implemented in FESOM can be found in [Wekerle \(2013\)](#).

After [Josey \(2003\)](#), the sea surface heat and salt fluxes can be expressed as the sea surface density flux  $F_\rho$  in  $\text{kg m}^2 \text{ s}^{-1}$  as

$$F_\rho = -\rho \left( \alpha \frac{Q_{\text{net}}}{\rho c_p} - \frac{\beta S}{1 - S/1000} (E - P) \right), \quad (2.22)$$

with the thermal expansion and haline contraction coefficients  $\alpha$  and  $\beta$  in  $\text{K}^{-1}$  and  $\text{psu}^{-1}$  and  $S$  short hand notation for SSS. Inserting the modeled heat and freshwater fluxes introduced above as well as adding the salinity relaxation term (as done in [Scholz, 2012](#); [Scholz et al., 2014](#)) yields

$$F_\rho = \rho \left( -\alpha F_T + \frac{\beta S}{1 - S/1000} F_{FW} + \beta F_{SR} \right). \quad (2.23)$$

Fig. 2.9 summarizes these thermal and haline upper boundary conditions that drive the sea surface density via eq. 2.9 exemplarily for the interior region of the Labrador Sea (index region shown in Fig. 2.7) as modeled by the 5th spinup cycle of the high-resolution model run (H5). A positive contribution to

$F_\rho$  indicates an increase of the sea surface density. To a first order, the total sea surface density change (black line) is determined by the thermal sea surface flux contributions (first term in 2.23). Downwelling short- and longwave radiation during summer lead to a buoyancy gain at the sea surface which is opposed by the upward longwave radiation as well as a heat loss induced through the turbulent sensible and latent heat fluxes (Fig. 2.9 a). In addition, the haline contribution due to evaporation increases the sea surface density. Precipitation (rain and snow) and the unphysical salinity relaxation, in contrast, lead to a sea surface buoyancy gain. The contribution of continental runoff is negligible in this Labrador Sea interior region where coastal areas are excluded.

The temporal evolution of all contributions to  $F_\rho$  over the whole forcing period 1948-2009 is shown in Fig. 2.9 b (here, the monthly time series in are low pass filtered by a 3-year running mean). Approximately the same balance is obtained as for the average annual cycle. The total surface density tendency is negative, indicating a sea surface buoyancy gain throughout the forcing period. During the 1970s, 1980s, and 1990s, however, this balance is shifted towards a sea surface density increase due to the turbulent sensible and latent heat flux contributions. These events are aligned with positive North Atlantic Oscillation (NAO) phases as indicated by gray bars in Fig. 2.9 b (Hurrell, 2003). During positive NAO events, increased differences in air pressure over the subtropical and subpolar North Atlantic gyres lead to enhanced horizontal wind velocities in the westerly flow (see Fig. 2.7). Thereby, cold air is advected over the relatively warm sea surface that leads to an increased heat loss due to sensible and latent heat fluxes. Note that these effects vanish if the components of  $F_\rho$  were integrated globally. Then, all contributions to  $F_\rho$  are rather constant in time (not shown).

To validate the methodology described above,  $F_\rho$  can alternatively be obtained by the saved output surface forcing variables `qnet`, `virtual_salt` and `relax_salt`, which represent the introduced variables  $Q_{\text{net}}$  (eq. 2.16),  $F_{VS}$  (eq. 2.18) and  $F_{RS}$  (eq. 2.20), respectively. Then, eq. 2.23 may be written as

$$\hat{F}_\rho = -\frac{\alpha}{c_p} \text{qnet} + \rho \beta (\text{virtual\_salt} + \text{relax\_salt}). \quad (2.24)$$

The comparison of eq. 2.23 and eq. 2.24 yields two differences between the haline contributions (2nd terms in both equations). First, the reference salinities used for converting the freshwater into a salinity flux are the sea surface

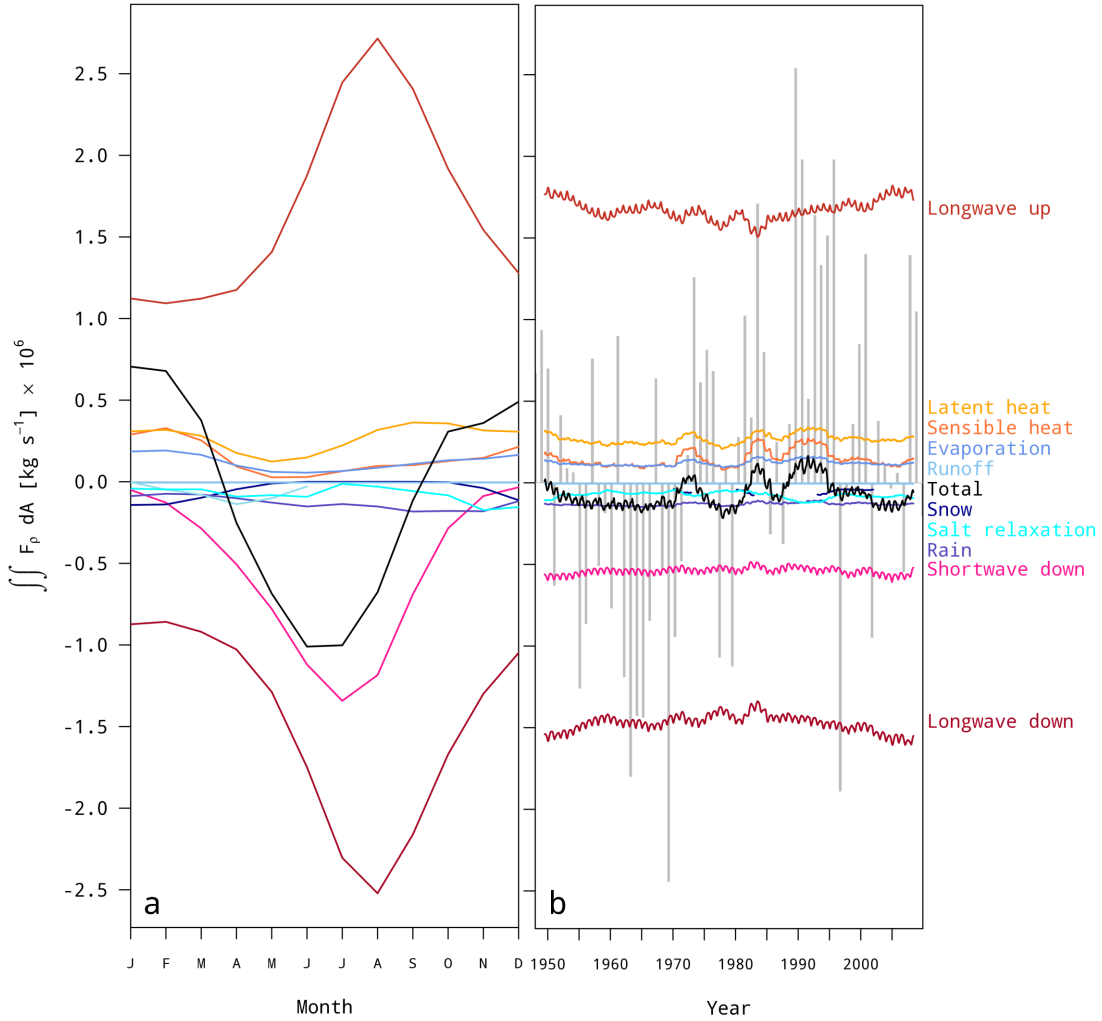


**Figure 2.9:** Average (1948-2009) annual cycle (a) and temporal evolution (b) of thermal and haline surface density forcing flux  $F_\rho$  components (colors) and their sum (black, all in  $10^6 \text{ kg s}^{-1}$ , see eq. 2.23) as modeled by the H5 run, area-integrated over the Labrador Sea interior region indicated in Fig. 2.7 b. Positive values represent a sea surface density increase. The blue line in a, that ends in June, represents the haline sea surface density contribution from the growth/decay of sea ice. All monthly time series in b are low pass filtered by a 3-year running mean and gray bars show the NAO index on an arbitrary scale (Hurrell, 2003).

salinity of the local model node in the former and  $S(1 - S/1000)^{-1}$  in the latter ( $S$  also being the modeled SSS Josey, 2003). Second, the global mean of the virtual salinity flux was removed in the  $\hat{F}_\rho$  formulation before saving `virtual_salt` on disk. This correction step was not done in the  $F_\rho$  calculation. Fig. 2.10 exemplarily compares  $F_\rho$  and  $\hat{F}_\rho$  as modeled by the H5 run. Here,  $F_\rho$  (black line) is the same as in Fig. 2.9 b. Generally, both derivations

of the sea surface density flux yield similar results. The two differences stated above lead to higher sea surface densities when the  $F_\rho$  formulation is used compared to  $\hat{F}_\rho$ . However, these differences are considered negligible for the temperature budget calculations in chapter 4.

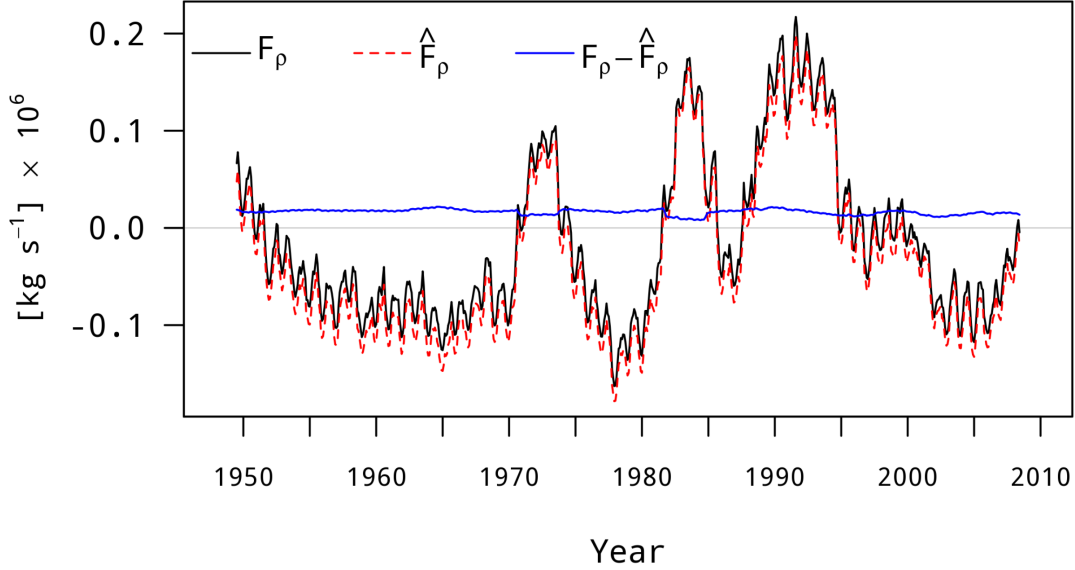


**Figure 2.10:** Comparison of sea surface density forcing  $F_\rho$  obtained by eq. 2.23 (black, same as in Fig. 2.9 b) against  $\hat{F}_\rho$  (eq. 2.24, red dashed). The anomaly  $F_\rho - \hat{F}_\rho$  is shown in blue. Positive values indicate an increase of the sea surface density. Results are from the H5 run, area-integrated over the Labrador Sea interior region indicated in Fig. 2.7 b.

## 2.3 Definition of modeled eddy fluxes

Since the ocean circulation takes place on a variety of spatial and temporal scales, modeling results as well as observations of oceanographic variables are obtained in an averaged way. In the high-resolution FESOM setup used in this study, for example, the smallest model time step  $\Delta t$  equals 10 minutes (see Tab. 2.1). This implies that a process on time scales shorter than 10 minutes can not be modeled. This is also the case for very long time scales as well as for the spatial dimension of the modeled processes. It is thus convenient to represent the modeled or observed variable of interest  $C$  as a temporal or spatial average  $\bar{C}$  and a deviation from that average,  $C'$ , with the condition

that  $\overline{C'} = 0$ . This yields the "Reynolds" averaging (see e.g. chapter 11 of Vallis, 2017)

$$C = \overline{C} + C'. \quad (2.25)$$

Based on this rationale, the average "total" transport of the tracer  $C$ , that arises through the advection term of the Boussinesq thermodynamic tracer equation 2.8 in flux form,  $\nabla \cdot \mathbf{u}C$ , may be written as

$$\overset{\text{model}}{\mathbf{u}C} = \overline{\mathbf{u}C} = \overline{(\overline{\mathbf{u}} + \mathbf{u}')(\overline{C} + C')} = \overline{\overline{\mathbf{u}}\overline{C}} + \overline{\overline{\mathbf{u}}C'} + \overline{\mathbf{u}'\overline{C}} + \overline{\mathbf{u}'C'} = \overline{\mathbf{u}}\overline{C} + \overline{\mathbf{u}'C'}, \quad (2.26)$$

where the condition  $\overline{C'} = 0$  and the equalities  $\overline{\overline{C}} = \overline{C}$  and  $\overline{A+B} = \overline{A} + \overline{B}$  were used. Hence, the average total transport  $\overline{\mathbf{u}C}$  occurs through an average mean part ( $\overline{\mathbf{u}}\overline{C}$ ) and an average varying ("eddy"<sup>1</sup>) part ( $\overline{\mathbf{u}'C'}$ ).

This composition raises a constraint on the model strategy since the average eddy transport

$$\overline{\mathbf{u}'C'} = \overline{\mathbf{u}C} - \overline{\mathbf{u}}\overline{C}, \quad (2.27)$$

in turn, requires the knowledge of the average total flux  $\overline{\mathbf{u}C}$ . Earlier observational and model studies, e.g. Stammer and Wunsch (1999); Penduff et al. (2004), defined the eddy part as a deviation of a longer time-mean so that eq. 2.27 becomes

$$\overline{\mathbf{u}'C'}^{\text{mon}} = \overline{\mathbf{u}_{\text{mon}}C_{\text{mon}}}^{\text{year}} - \overline{\mathbf{u}_{\text{mon}}}^{\text{mon}}\overline{C_{\text{mon}}}^{\text{mon}}, \quad (2.28)$$

if, for example, only monthly realizations of  $C = C_{\text{mon}}$  are available ( $\overline{C_{\text{mon}}}^{\text{mon}} = C_{\text{mon}}$ ). In this case, the monthly averaged eddy transport would arise as the deviation from the annually averaged total transport. In contrast, this study follows e.g. von Storch et al. (2012) by calculating the necessary total transport of  $C$  in every time step during the model run and subsequent saving its monthly mean. With the notation above this yields

$$\overline{\mathbf{u}'C'}^{\text{mon}} = \overline{\mathbf{u}_{\Delta t}C_{\Delta t}}^{\text{mon}} - \overline{\mathbf{u}_{\Delta t}}^{\text{mon}}\overline{C_{\Delta t}}^{\text{mon}}, \quad (2.29)$$

with  $C_{\Delta t}$  being the model realization of  $C$  over the model time step  $\Delta t$  (see Tab. 2.1). Hence, a monthly-averaged eddy quantity defined as in eq. 2.28 contains variations on time scales from a month to a year, while formulation 2.29 captures the variability from the model time step to a month. This is

---

<sup>1</sup>Already Stokes (1845) (p. 304) used this terminology.

important to note since Rieck (2014) showed that the influence of the used averaging period on the obtained eddy quantity may be large. Figure 2 from Rieck (2014) is shown here to illustrate this behavior (Fig. 2.11). Results from the ocean model ORCA in a  $1/12^\circ$  configuration indicate that a larger averaging period generally leads to a larger eddy contribution as shown for the modeled horizontal eddy kinetic energy  $EKE = 0.5 \overline{\mathbf{u}'_h{}^2}$  in the Gulf Stream region (black lines in Fig. 2.11).

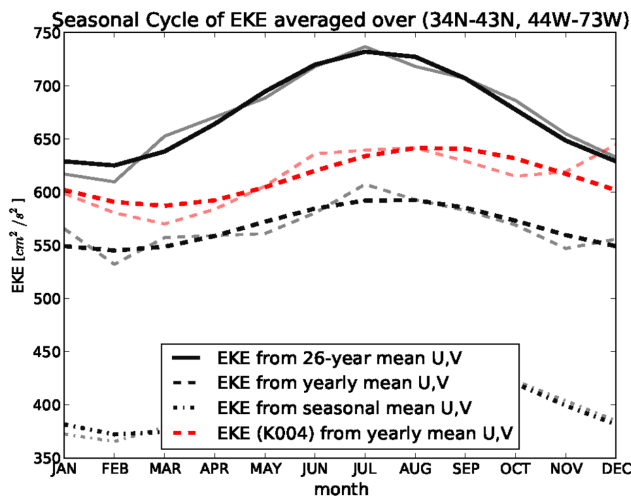


**Figure 2.11:** Figure 2 from Rieck (2014) to illustrate the influence of the used averaging period on the obtained eddy quantity. A larger averaging period, e.g. 26 years (solid), a year (dashed) or a season (dot-dashed black lines), generally leads to a larger eddy contribution.

## 2.4 Meridional overturning calculation on an irregular grid

The meridional overturning circulation (MOC), i.e. the total northward (or southward) transport in an ocean basin integrated from west to east induced through external forcing (e.g. wind) as well as internal density differences (thermohaline circulation) can be described via a *stream function*  $\psi$  (Olbers et al., 2012). For a steady ( $\partial_t \mathbf{u} = 0$ ) and incompressible ( $\nabla \cdot \mathbf{u} = 0$ ) fluid, lines of constant  $\psi$  (*stream lines*) show the direction of the velocity at a fixed time point. Let  $d\mathbf{r}_s = \mathbf{j} dy + \mathbf{k} dz$  be an element of the stream line  $s$  of infinitesimal length pointing in the same direction as the local 2-dimensional velocity vector  $\mathbf{u}_\psi = \mathbf{j}v + \mathbf{k}w$  in the  $y$ - $z$ -plane (Fig. 2.12).

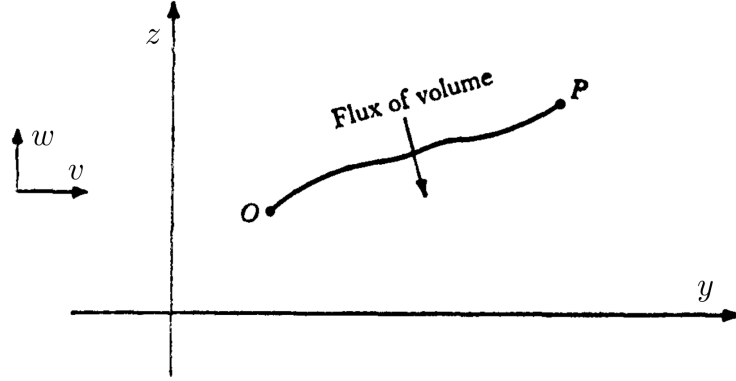


**Figure 2.12:** The stream function  $\psi$  results from the volume flux integrated over the curve from  $O$  to  $P$ . Modified from [Batchelor \(2000\)](#).

In cartesian coordinates  $\mathbf{dr}_s \times \mathbf{u}_\psi = 0$  and hence

$$w \, dy - v \, dz = 0. \quad (2.30)$$

Defining a total (or exact) differential  $d\psi(y, z) = w \, dy - v \, dz$  ensures the existence of  $\psi$  related to  $v$  and  $w$  if  $d\psi(y, z) = \partial_y \psi(y, z) \, dy + \partial_z \psi(y, z) \, dz$ . As already noted by [Lagrange \(1781\)](#) (p. 720), this is ensured due to the incompressibility of the flow<sup>2</sup> and it follows that

$$v = -\partial_z \psi \quad \text{and} \quad w = +\partial_y \psi. \quad (2.31)$$

Note that the  $+$  and  $-$  signs solely depend on the choice of the total differential  $d\psi$  and may be interchanged by starting from  $\mathbf{u}_\psi \times \mathbf{dr}_s = 0$  instead.

To obtain a measure for the complete northward (southward) meridional transport, the zonally integrated velocity from west ( $x = x_W$ ) to east ( $x = x_E$ )

$$\begin{aligned} \mathbf{U}_\psi(y, z) &= \mathbf{j} V(y, z) + \mathbf{k} W(y, z) \\ &= \mathbf{j} \int_{x_W}^{x_E} v(x, y, z) \, dx + \mathbf{k} \int_{x_W}^{x_E} w(x, y, z) \, dx \end{aligned} \quad (2.32)$$

<sup>2</sup> $d\psi(y, z) = w(y, z) \, dy - v(y, z) \, dz$  (I) is a total (or exact) differential if  $d\psi(y, z) = \partial_y \psi(y, z) \, dy + \partial_z \psi(y, z) \, dz$  (II). This is the case if  $w(y, z) = \partial_y \psi(y, z)$  and  $v(y, z) = -\partial_z \psi(y, z)$  (III). Because of the incompressibility of the flow ( $\partial_y v = -\partial_z w$ ) and Schwarz's theorem ( $\partial_{yz}^2 \psi(y, z) = \partial_{zy}^2 \psi(y, z)$ ), (III) is true.  $v$  and  $w$  (2.31) are found by comparing (I) and (II).

is used. Integration along the ocean basin (e.g. from bottom to the surface or from south to north) provides the solution for the transport  $\psi(y, z)$  in  $\text{m}^3 \text{s}^{-1}$  as

$$\psi(y, z) = \psi_0 + \int_O^P (W \, dy - V \, dz), \quad (2.33)$$

where  $\psi_0$  is a constant and most often set to zero (e.g. Lamb, 1916, p. 60; Batchelor, 2000, p. 76). The flux along a line of constant  $\psi > 0$  is clockwise in the  $y$ - $z$ -plane and anticlockwise if  $\psi < 0$ .

Through FESOMs irregular mesh, however, the described method poses numerical difficulties as described by Sidorenko et al. (2009) and its implementation is not straight forward. Alternatively,  $\psi$  may be determined via the relative vorticity  $\zeta$  of the flow in the  $y$ - $z$ -plane defined as

$$\zeta(y, z) = \mathbf{i} \cdot \nabla(y, z) \times \mathbf{U}_\psi(y, z) = \partial_y W(y, z) - \partial_z V(y, z) = \nabla^2(y, z) \psi(y, z), \quad (2.34)$$

where subsequent solving yields  $\psi$ . This, however, involves interpolation of the irregular data onto a regular grid. Another approach is the calculation of the overturning stream function by "binning". For this, the ocean basin of interest is segmented in latitudinal bins from south  $y_S$  to north  $y_N$  by a constant  $\Delta y$ . Then, the meridionally cumulative sum of the element area  $A$  weighted element-averaged vertical velocity  $\langle w \rangle$ , summed over all 3D-elements within latitude bin  $y_i$  at depth level  $z_j$ , yields

$$\begin{aligned} \psi^*(y_i, z_j) &= \sum_{\text{e3D} \in (y_i, z_j)} A_{\text{e3D}} \langle w \rangle_{\text{e3D}} \\ \psi(y_i, z_j) &= \sum_{k=1}^i \psi^*(y_k, z_j). \end{aligned} \quad (2.35)$$

This is possible through the regular vertical alignment of the nodes (Sidorenko et al., 2009) and no interpolation onto a regular grid is necessary. The stream function calculation via eq. 2.35 was performed with the program `fpost` by Dmitry Sidorenko (<https://fesom.de/tools/fpost/>) and analyses of  $\psi$  are provided in chapter 3.



### 3 Effects of high resolution and spinup time on the North Atlantic circulation

The North Atlantic circulation as modeled with the low- and high-resolution FESOM setups as introduced in the preceding chapter is presented here. The high-resolution general circulation, long Rossby wave propagation as well as deep convection variability in the Labrador Sea are compared to the low-resolution control run. The results are then discussed in terms of the combined effect of the high horizontal model resolution (see section 2.1.4) and a long spinup time (see section 2.1.5).

*Declaration: this chapter was published in Danek et al. (2019).*

#### 3.1 General circulation

The average (1961-2009) modeled horizontal North Atlantic barotropic circulation is composed of a clockwise rotating subtropical and anti-clockwise rotating subpolar gyre, separated by the Gulf Stream and its extension the North Atlantic Current (NAC, Fig. 3.1, in Sverdrup,  $1 \text{ Sv} = 10^6 \text{ m}^3 \text{ s}^{-1}$ ). The high-resolution model exhibits a stronger subpolar and subtropical gyre transport, as well as enhanced small scale features when compared to the low-resolution control run. After the first spinup cycle (L1 and H1, Fig. 3.1 a, b) the high-resolution Gulf Stream separates from the North American coast several degrees further south, is of narrower shape and exhibits transports around 100 Sv (peak values around 120 Sv), around twice the transports of the low-resolution Gulf Stream. North of the Gulf Stream (south of Newfoundland) an anticlockwise re-circulation cell of 30-40 Sv is present in the H1 run but almost absent in the L1 run. Further downstream, the high-resolution model shows a distinct transition behavior between the Gulf Stream and its extension the North Atlantic Current comprising a North West Corner-like circulation pattern. The average (1993-2009) position of zero SSH as derived by satellite altimetry (AVISO) in Fig. 3.1 (thick black line) indicates the observed boundary between the subtropical and subpolar gyres. The subpolar gyre is also intensified in the high-resolution model with enhanced transports in the Labrador, Irminger, Iceland and Nordic Seas.

The gyre structures change from the 1st to the 5th spinup cycles (i.e. after  $\sim 300$  model years, Fig. 3.1 c, d) in the high-resolution model, whereas remain rather unchanged in the low-resolution control run. The anticlockwise re-circulation cell north of the Gulf Stream axis decreased by  $\sim 50\%$  to 15 Sv.

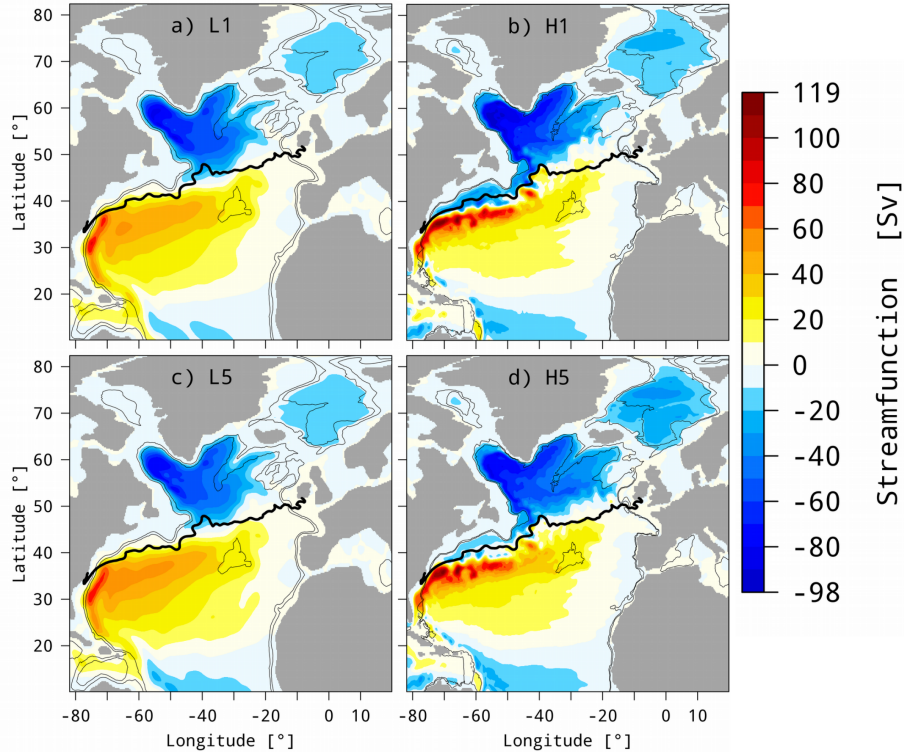


**Figure 3.1:** Average (1961-2009) horizontal barotropic stream function (colors, in Sv,  $1 \text{ Sv} = 10^6 \text{ m}^3 \text{ s}^{-1}$ , positive clockwise,  $10 \text{ Sv}$  contour interval) of 1st (a, b) and 5th (c, d) spinups of low- (left column) and high- (right column) resolution models. Thick black line shows the average (1993-2009) zero sea surface height (SSH) as derived by satellite altimetry (AVISO). Thin black lines are 1 and 2 km isobaths.

The transition area between Gulf Stream and North Atlantic Current including the North West Corner exhibits reduced transports with increasing number of spinup cycles. Although the general shape and strength of the Gulf Stream west of  $\sim 50^\circ \text{ W}$  persists through the spinup cycles, the current penetrates further east in H5 compared to H1 (Fig. 3.1 b, d) – the Gulf Stream becomes more zonal with spinup time. The high-resolution North Atlantic Current shows a similar behavior: the anticlockwise transports in the Iceland Basin (south of Iceland) increased around  $20 \text{ Sv}$  meaning that the North Atlantic Current shifted from its northeast direction in the 1st spinup to a more eastward directed flow in the 5th spinup. Similarly, the cyclonic circulation in the Greenland Iceland Norwegian (GIN) Seas increases by  $\sim 10 \text{ Sv}$ . In contrast, the cyclonic circulations in the Labrador and Irminger Sea decrease with spinup time by  $10\text{-}15 \text{ Sv}$ . The low resolution model does not show these changes of the horizontal barotropic stream function with spinup time.

The average (1961-2009) Atlantic meridional overturning circulation (AMOC, in Sv, Fig. 3.2) shows generally increased maximum transports in the high- compared to the low-resolution model. In particular, the maximum of the upper clockwise circulation cell in H1 ( $\sim 23$  Sv) approximately doubles compared to L1 ( $\sim 13$  Sv). An anticlockwise circulation cell in the deep ocean is almost absent in both models in the 1st model spinup. After 5 spinup cycles the upper clockwise circulation maxima decreased to 11 Sv in L5 (15 % reduction), and 16 Sv in H5 (30 % reduction) respectively.

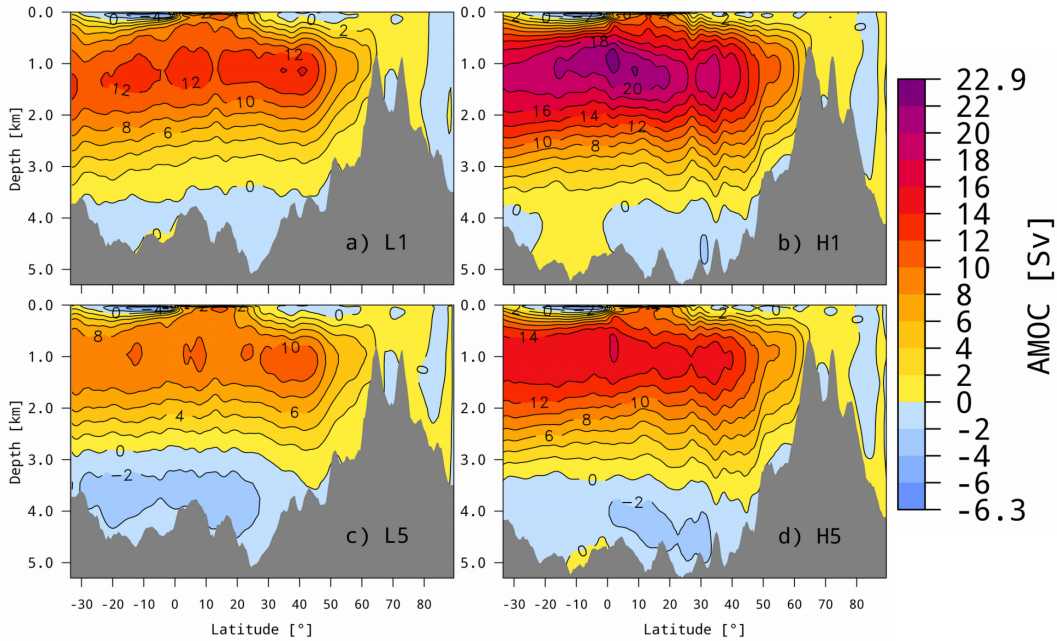


**Figure 3.2:** Average (1961-2009) Atlantic Meridional Overturning Circulation (AMOC, in Sv, positive clockwise, 2 Sv contour interval) of 1st (a, b) and 5th (c, d) low- (left column) and high- (right column) resolution models. A local smoothing window was applied for plotting.

In contrast, the strength of the lower anticlockwise circulation cell increased from  $-1$  to  $-3$  Sv in both models and is stronger in the low-resolution model. This change is also reflected in a shallower interface between both circulation cells from 3.8 km (L1) to 3 km (L5) and from 3.8 km (H1) to 3.4 km (H5) in the tropics and sub-tropics.

The decadal evolution of the overturning maxima at different latitudes shows a similar variability in time, independent of model resolution and number of spinup cycles (Fig. 3.3). Generally, the overturning maxima are increased by  $\sim 50$  (15) % in the high- compared to the low-resolution model at  $26.5^\circ$  ( $41^\circ$ )

N. From the 1st to the 5th spinup cycles the average (1948-2009) overturning decreases around 20 % in both models and at both latitudes towards quasi-equilibrium. The low-resolution overturning reduces by 14 (12), 10 (8.5) and 2.5 (1.8) % from the 1st to 2nd to 3rd to 4th spinup cycle at 26.5° (41°) N. Similar values are obtained for the high-resolution model with 12 (15), 6.6 (6.7) and 1.6 (0.5) % at 26.5° (41°) N.

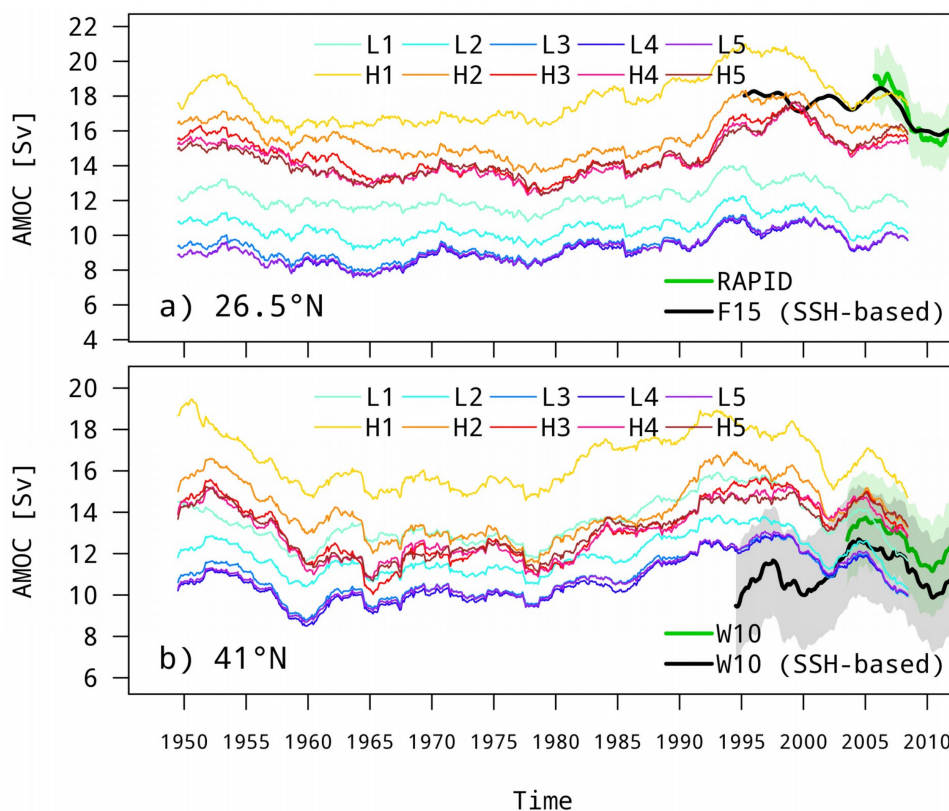


**Figure 3.3:** Decadal evolution of AMOC maximum at 26.5° N (a) and 41° N (b) of all 5 spinups of low- and high-resolution models. In a), thick green and black lines show respectively overturning rates as observed (RAPID, Smeed et al. (2017), shading shows uncertainty given by authors) and an updated version of the SSH-based estimate of Frajka-Williams (2015). In b), they are an updated version of measured and SSH-based overturning rates from Willis (2010) (shading shows one standard deviation). All time series are low pass filtered by a 3-year running mean.

In both models this spinup adjustment “converges” after 4 spinup cycles (248 model years) in the sense that the change from the 4th to the 5th cycle changes sign and is of similar magnitude as the change from the 3rd to the 4th: 0.8 (1.2) and 0.7 (0.4) % increase in the low- and high-resolution models respectively at 26.5° (41°) N. At 26.5° N, the overturning of the H1 run shows an overlap from the years 2004-2009 with observations of the RAPID array (Smeed et al.,

2017, green line in Fig. 3.3 a) as well as an SSH-based estimate of Frajka-Williams (2015) (black line in Fig. 3.3 a). However, the spinup adjustment leads to transports weaker than observed at that latitude. At 41° N the situation is different: here, the high-resolution maximum overturning rates exceed these measured by Willis (2010) even after the spinup adjustment (within the observed upper uncertainty bounds). Initially, the L1 run exhibits the best agreement with the observations (green line in Fig. 3.3 b). The L5 run, however, underestimates the overturning within the observed lower uncertainty bounds.

The total meridional North Atlantic Ocean heat transport

$$\text{OHT} = \rho_{\text{ref}} c_p \int_{\text{West}}^{\text{East}} \int_{\text{Bottom}}^{\text{Surface}} \overline{v\theta} dz dx \quad (3.1)$$

is shown in Fig. 3.4 (in PW, 1 PW = 10<sup>15</sup> W, positive northward, overbar denotes the temporal mean, with meridional velocity  $v$  in m s<sup>-1</sup>, potential temperature  $\theta$  in °C, constant reference density  $\rho_{\text{ref}} = 1027$  kg m<sup>-3</sup> and the specific heat capacity of sea water  $c_p = 3985$  m<sup>2</sup> s<sup>-2</sup> K<sup>-1</sup>, the product  $v\theta$  was calculated at every model time step, see section 2.3). The high-resolution OHT increases by 50-70 % compared to the low-resolution model with largest transports up to 1.2 PW in the subtropics in the H1 run.

The spinup adjustment leads to an average OHT reduction of ~0.2 PW in both models. H1 covers the observed OHT range at 26.5° N from Johns et al. (2011), a total heat flux  $\overline{v\theta}$  estimate taking spatial covariabilities of  $v$  and  $\theta$  into account (diamond in Fig. 3.4), while all other heat transports are too weak. At 47° N, in contrast, H1 overestimates the OHT and H3 and H5 show the best agreement with an inverse estimate from Ganachaud and Wunsch (2003), which is a mean heat flux  $\overline{v\theta}$  where correlated temporal variations are neglected (triangles in Fig. 3.4). At 30° S, all high-resolution model runs overestimate the Ganachaud and Wunsch (2003) solution while the low-resolution model runs are in the observed OHT range. North of 55° N until the pole the differences between the spinup runs of the respective models diminish.

The observed average (1993-2009) geostrophic surface velocity as derived by satellite altimetry (AVISO, Fig. 3.5 a) shows a vigorous extension of the Gulf Stream in form of fast (> 25 cm s<sup>-1</sup>) and narrow meanders. From the North West Corner around 44° W and 51° N the North Atlantic Current flows eastward and further downstream northeastward in the Iceland Basin (with ~15 cm s<sup>-1</sup>).

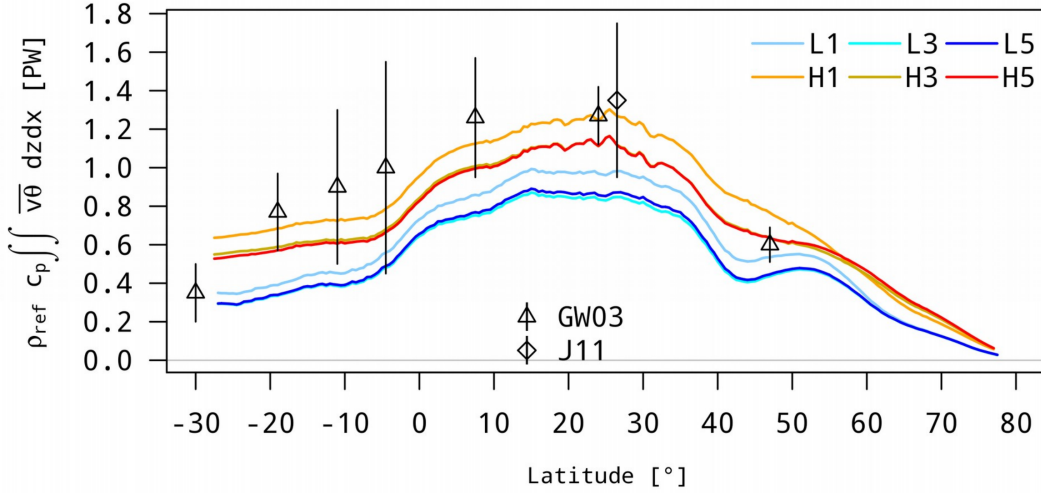


**Figure 3.4:** Average (1961-2009) total North Atlantic meridional heat transport (in PW,  $1 \text{ PW} = 10^{15} \text{ W}$ , positive northward) of low- and high-resolution spinup runs (colored lines). GW03 (triangles) shows the inverse estimate of Ganachaud and Wunsch (2003) (uncertainties given by authors) and J11 (diamond) the observation at  $26.5^\circ$  North (MOCHA, Johns et al., 2011, uncertainty is one standard deviation). In the models, the product  $v\theta$  was calculated at every time step (see section 2.3).

H1 shows a Gulf Stream extension with features similar in strength, shape, and position as observed (Fig. 3.5 b, full and not geostrophic modeled velocities are used since the results apply to both, not shown). The North West Corner, however, is half as strong as observed and the North Atlantic Current corresponds with the measured position but is stronger than observed (up to  $\sim 25 \text{ cm s}^{-1}$ ). Similarly, the Western Boundary Current (WBC) exhibits larger velocities along the coasts of Greenland and Newfoundland. After 5 spinup cycles the modeled high-resolution North West Corner is hardly visible and the whole Gulf Stream extension structure is shifted to the southeast with large ( $> 15 \text{ cm s}^{-1}$ ) northeastward directed velocities east of  $40^\circ \text{ W}$  (Fig. 3.5 d). The low-resolution model, in contrast, exhibits neither narrow and fast meanders as Gulf Stream extension nor a North West Corner-like structure (Fig. 3.5 c; here, only the 5th spinup is shown since the differences to the 1st spinup are negligible). The Gulf Stream extension is broad, slow and almost entirely eastward directed. From  $40^\circ \text{ W}$  the current continues eastward more than twice as fast as measured (similar as in H5). At around  $33^\circ \text{ W}$  the broad and slow current in L5 turns northeastward into the North Atlantic Current.

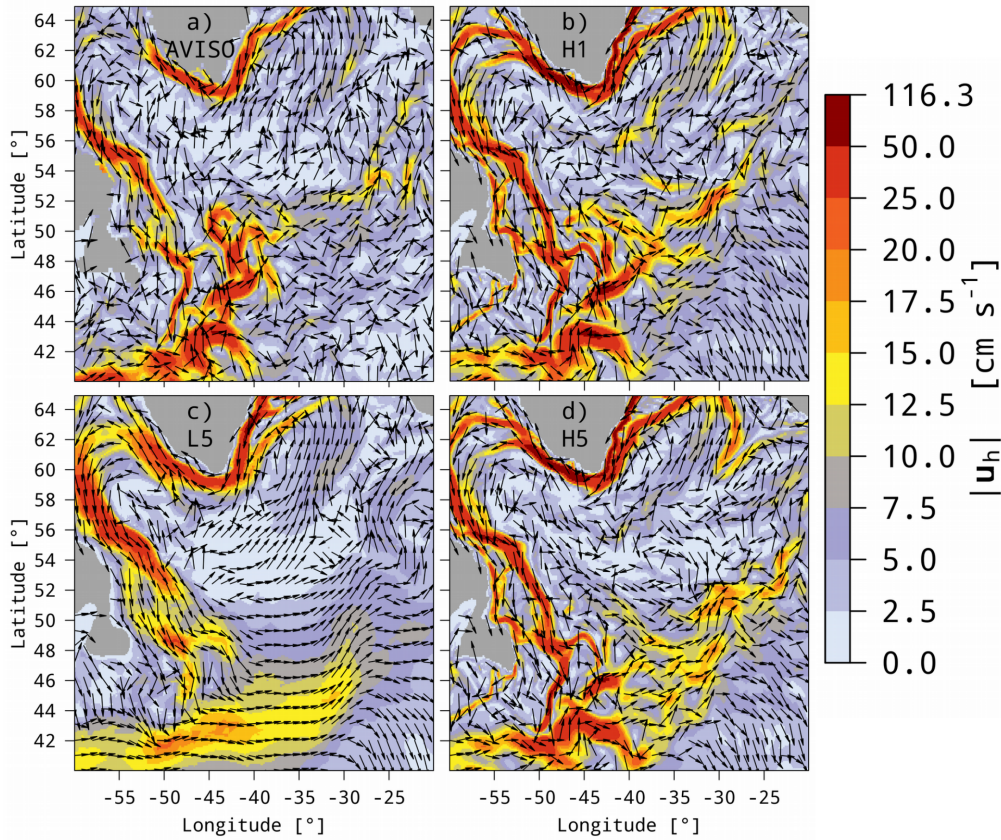


**Figure 3.5:** Average (1993-2009) horizontal surface velocity norm (in  $\text{cm s}^{-1}$ , irregular levels) and direction (arrows of constant length, not all plotted). a) shows geostrophic velocities as derived by satellite altimetry (AVISO), b) the 1st spinup of the high-resolution model and c) and d) the 5th spinups of low- and high-resolution models respectively (differences between 1st and 5th low-resolution spinups are negligible). For the models the full (not geostrophic) velocities are shown.

## 3.2 Long Rossby Wave Propagation

Fig. 3.6 shows depth anomalies of the  $17^\circ\text{C}$  isotherm across the North Atlantic basin at  $30^\circ\text{N}$  of the 5th spinups of both models as a function of longitude and time (in m; seasonal mean 1948-2009 removed; positive values indicate deeper depths). On average, this isotherm is located at approximately 250 m depth in both models. Depth anomaly contours of several tens of meters travel westward in the high-resolution model throughout the forcing period with a velocity of  $3.12 \pm 0.07 \text{ cm s}^{-1}$  as inferred by Radon transform (straight line starting from the lower right in Fig. 3.6 b; see chapter 6.4 of Robinson (2010) and references therein for a description of the Radon transform; the velocity uncertainty was derived via equation A3 of Alvera-Azcárate et al. (2009), dotted lines in b).

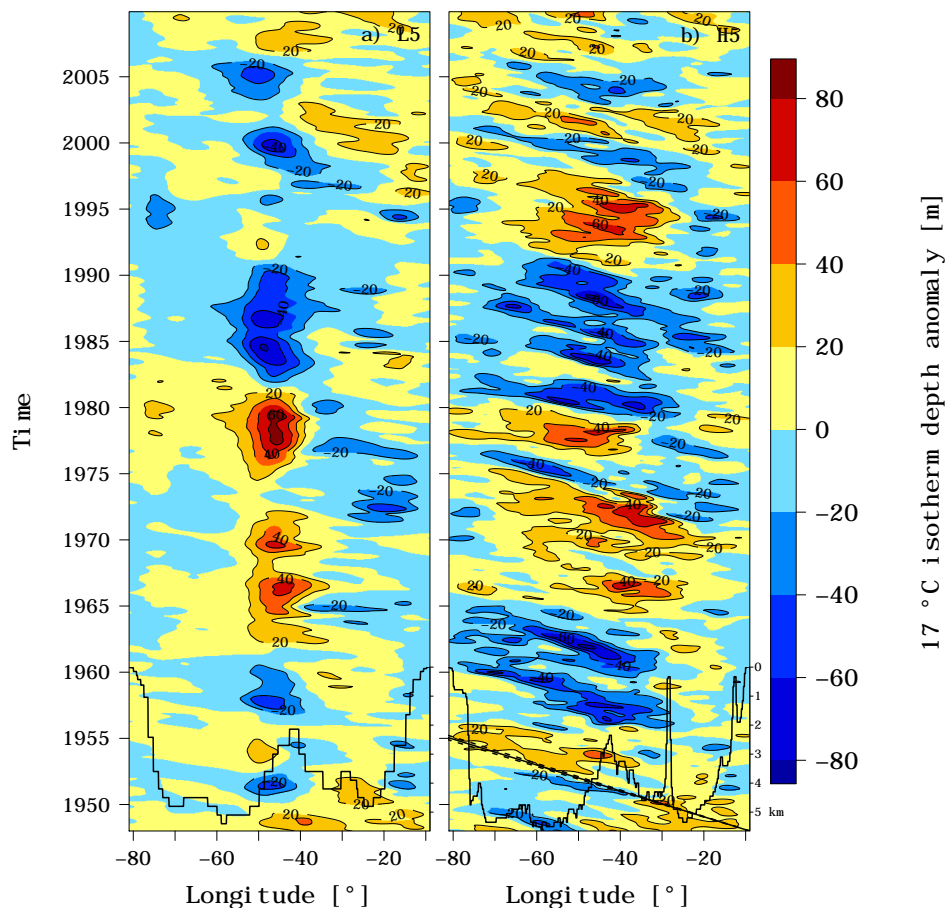


**Figure 3.6:** 17 °C isotherm depth anomalies of the 5th spinups of low- (a) and high-resolution (b) models as a function of longitude and time along 30° N in the Atlantic (colors, in m, seasonal mean 1948-2009 removed, positive values indicate deeper depths). The anomalies were smoothed with a Gaussian Nadaraya–Watson filter with a bandwidth of 3° in longitude direction. The model bathymetry is added as black line (in km; axis on the lower right of b). The straight black and dotted lines in b show a westward velocity of  $3.12 \pm 0.07 \text{ cm s}^{-1}$  as determined by Radon transform (see text for details). The average (1948-2009) depth of the 17 °C isotherm is around 250 m in both models.

In the low-resolution model, in contrast, vertical isotherm displacements west of the Mid-Atlantic-Ridge (MAR) are rather stationary in space (Fig. 3.6 a; the model bathymetry in km is added as black line with corresponding axis on the lower right of b). The isotherm depth anomalies were filtered with a Gaussian Nadaraya–Watson filter (Fan and Gijbels, 1996) with a bandwidth

of  $3^\circ$  in longitude direction to reduce small-scale noise as used similarly in e.g. Abe et al. (2016).

Furthermore, similar westward wave propagations of several cm magnitude can be detected in the SSH anomalies (not shown) as well as in the first  $m$  baroclinic WKB approximated horizontal velocity modes

$$R_m \stackrel{\text{WKB}}{\approx} c_{g,m} N S_{0,m} g^{-1} \cos\left(c_{g,m}^{-1} \int_{-H}^z N(z) dz\right), \quad (3.2)$$

where  $c_{g,m} \stackrel{\text{WKB}}{\approx} (m\pi)^{-1} \int_{-H}^0 N(z) dz$  represents the  $m$ -th baroclinic gravity wave speed with buoyancy frequency  $N = (-g\rho^{-1} \partial_z \rho)^{1/2}$ , acceleration due to gravity  $g$  and in situ density  $\rho$ .  $S_{0,m} = (c_{g,m} N^{-1})^{1/2}$  serves as a dimensionless normalization constant (see equation 3.72 on page 117 in Vallis, 2017).

These modes represent wave solutions to the horizontal part of the linearized quasigeostrophic potential vorticity equation of a flat bottom ocean with zero background flow and associated vertical wave number  $m$  (equation 3.56 on page 115 in Vallis, 2017). Further information can be found in section 6.11 of Gill (1982). The average vertical structure of  $R_m$ , showing a surface intensification and  $m$  zero crossings of each  $m$ -th mode, does not differ much between the models as shown in Fig. 3.7. Similarly as in Fig. 3.6, Fig. 3.8 shows exemplarily  $R_1$  and  $R_2$  in 500 meters depth as a function of longitude and time. Spatio-temporal anomalies (seasonal mean 1948-2009 removed) are much larger in the high- compared to the low-resolution model, travel westward with a similar propagation velocity as the isotherm depth anomalies ( $3.4 \pm 0.02 \text{ cm s}^{-1}$ ) and are enhanced west of the MAR. With increasing wave number  $m$ , the differences between the two models diminish (not shown).

### 3.3 Hydrography

The average (1965-2004) upper ocean (0-100 m) temperature difference to the World Ocean Atlas 2013 (WOA, Locarnini et al., 2013) shown in Fig. 3.9 (in  $^\circ\text{C}$ ; model minus WOA) features warm as well as cold biases in the modeled North Atlantic. L1 exhibits a large ( $> 5$  up to  $8 \text{ }^\circ\text{C}$ ) warm bias north of the Gulf Stream axis and a large ( $< -5$  up to  $-9.5 \text{ }^\circ\text{C}$ ) cold bias at the Gulf Stream extension around  $40^\circ \text{ W}$  (Fig. 3.9 a). The Irminger Sea and the area of the Labrador Sea boundary current is  $\sim 2 \text{ }^\circ\text{C}$  warmer than observed. The Nordic

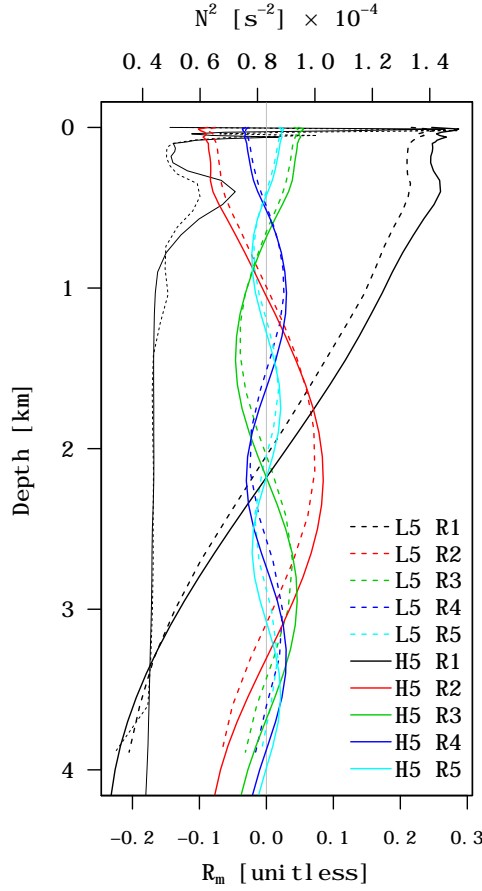
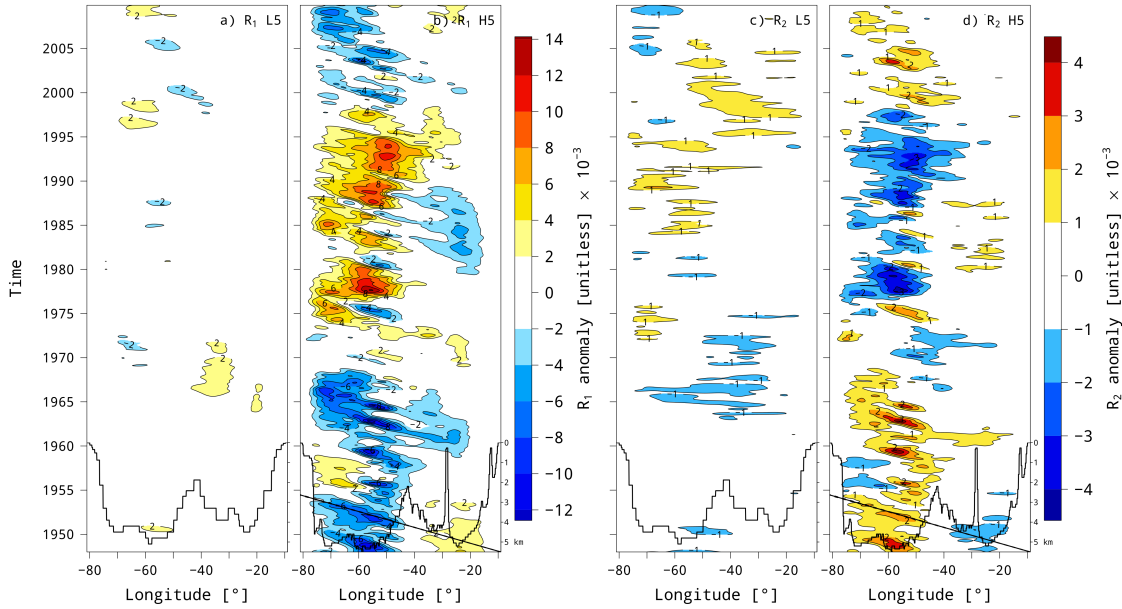


**Figure 3.7:** Exemplary stratification  $N^2 = g\rho^{-1} \partial_z \rho$  (in  $\text{s}^{-2} \times 10^{-4}$ , upper axis, thin black lines) and associated first five WKB approximated baroclinic horizontal velocity mode amplitudes  $R_m$  (unitless, lower axis, eq. 3.2) of 5th spinups of the low- (dashed) and high- (solid) resolution models in the North Atlantic at  $47.4^\circ \text{N}$  and  $20^\circ \text{W}$  of the modeled year 1983.

Seas (between Greenland and Norway) show a dipole of too cold ( $-4^\circ \text{C}$  at  $70^\circ \text{N}$ ) and too warm ( $2^\circ \text{C}$  at  $75^\circ \text{N}$ ) anomalies.

In H1, the mentioned large biases at the Gulf Stream and its extension are not visible (Fig. 3.9 b). In contrast, the vicinity of the North Atlantic Current (around  $30^\circ \text{W}$  and  $55^\circ \text{N}$ ) is  $2\text{-}3^\circ \text{C}$  warmer than observed as well as the East- and West Greenland Current and Labrador Current. A similar cold bias as in L1 exists in the Greenland Sea that is surrounded by a too warm boundary current ( $3^\circ \text{C}$ ) along the coastline of Norway, Spitzbergen, and Greenland.

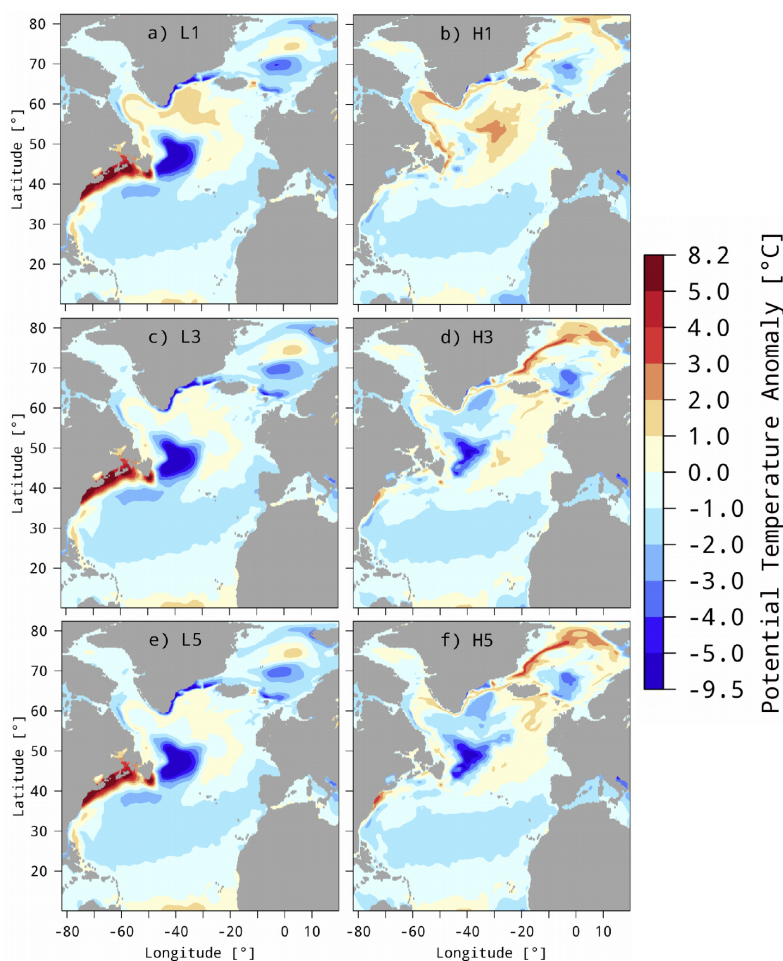
The temperature anomaly structure of the low-resolution model does not change with additional spinup cycles (Fig. 3.9 c, e). Only the warm bias



**Figure 3.8:** Anomalies of the 1st (a, b) and 2nd (c, d) WKB approximated baroclinic horizontal velocity mode amplitudes  $R_1$  and  $R_2$  in 500 m depth of the 5th spinups of low- (a, c) and high-resolution (b, d) models as a function of longitude and time along  $30^\circ$  N in the Atlantic (colors, unitless  $\times 10^{-3}$ , seasonal mean 1948–2009 removed, eq. 3.2). The anomalies were smoothed with a Gaussian Nadaraya–Watson filter with a bandwidth of  $3^\circ$  in longitude direction. The model bathymetry is added as black line (in km; axes on the lower right of b and d). The straight black and dotted lines in b and d show a westward velocity of  $3.4 \pm 0.02$  cm  $s^{-1}$  as determined by Radon transform performed in the area west of the Mid-Atlantic-Ridge.

of the subpolar gyre reduces by  $\sim 1$   $^\circ\text{C}$  from L1 to L5. The solution of the high-resolution model, in contrast, shows several changes during the spinup procedure. The North Atlantic Current warm bias in H1 vanishes in favor of a large ( $< -5$   $^\circ\text{C}$ ) cold bias in the Gulf Stream extension around  $40^\circ$  W from the 1st to the 3rd model spinup comparable with the one of the low-resolution control runs (Fig. 3.9 a, c).

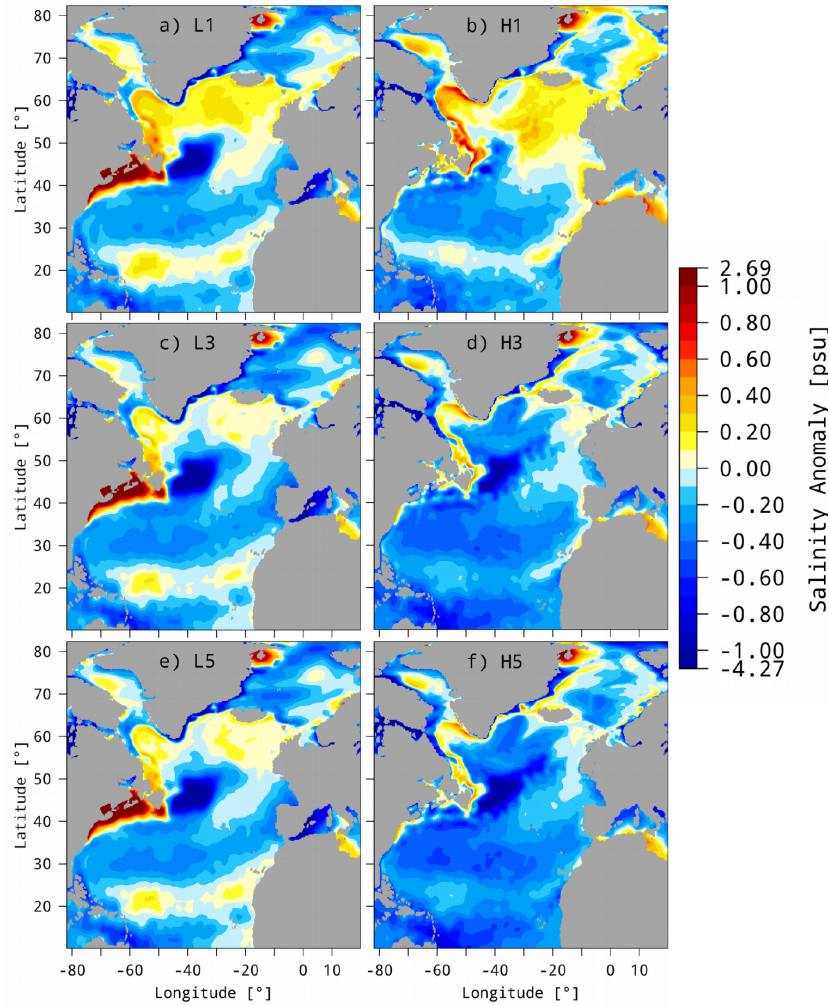
This behavior continues with spinup time and reaches very cold temperature anomalies up to  $-9$   $^\circ\text{C}$  similar as the low-resolution model (Fig. 3.9 e). The warmer than observed temperature anomalies in the northern Nordic Seas also increase with spinup time by up to a  $4$   $^\circ\text{C}$ . As in the low-resolution model, the Irminger and Labrador Sea become colder with spinup time and exhibit larger cold anomalies in the high-resolution model ( $-2$  to  $-3$   $^\circ\text{C}$ ). Large scale salinity anomalies (observations from Zweng et al. 2013) show similar model



**Figure 3.9:** Average (1965-2004, 0-100 meters) potential temperature anomalies (model minus observation, in °C) of low- (left column) and high- (right column) resolution models. Observations are from World Ocean Atlas 2013 (Locarnini et al., 2013). 1st (2nd, 3rd) row shows anomalies of 1st (3rd, 5th) model spinup minus observations.

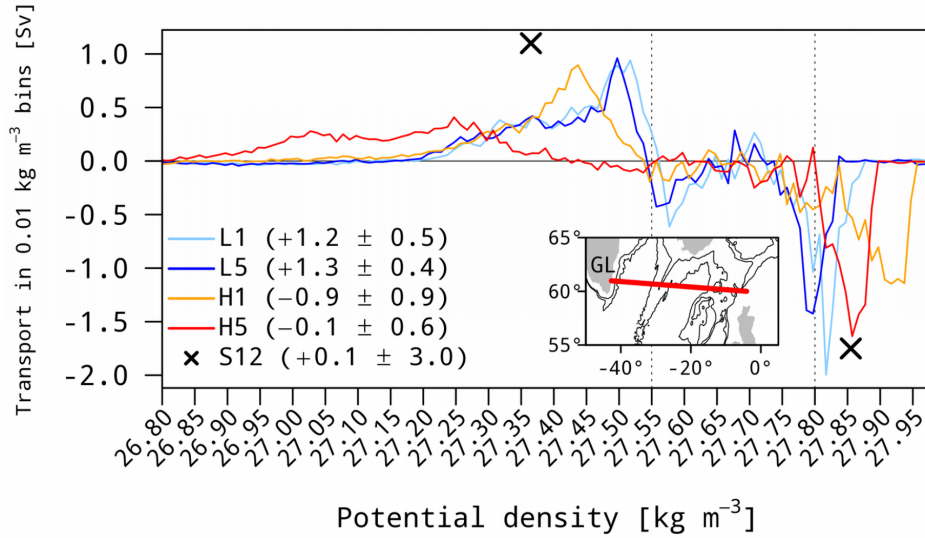
resolution- and spinup length dependencies as described for temperature (Fig. 3.10).

Fig. 3.11 shows the average summer (June-July, 2002-2008) potential density  $\sigma_\theta$  distribution of the north- and southward flowing water masses across  $\sim 60^\circ$  N in the North Atlantic (integrated in  $0.01 \text{ kg m}^{-3}$  potential density bins, northward positive). All models transport light water masses northward above a southward directed high-density water flow. The low-resolution (L1, L5) northward flow peaks around  $\sigma_\theta = 27.50 \text{ kg m}^{-3}$ , with the peak in L1 slightly shifted towards denser water masses in the 5th spinup cycle.



**Figure 3.10:** Average (1965-2004, 0-100 meters) salinity anomalies (model minus observation, in psu) of low- (left column) and high- (right column) resolution models. Observations are from World Ocean Atlas 2013 (Zweng et al., 2013). 1st (2nd, 3rd) row shows anomalies of 1st (3rd, 5th) model spinup minus observations.

In contrast, the H1 northward transport has a maximum at  $\sigma_\theta = 27.425 \text{ kg m}^{-3}$  and exhibits a transition towards a broad range of lighter water masses due to colder and fresher conditions from H1 to H5. L1, L5, and H1 resemble the observed northward flow (Sarafanov et al., 2012, black crosses) in magnitude but are shifted towards denser water masses compared to the observations. H5 is generally lighter and distributed over a broader density range (smaller amplitude) than observed. All modeled dense southward flows exhibit noticeable peaks and become lighter with spinup time. H5 matches the observed maximum southward transport at  $\sigma_\theta = 28.85 \text{ kg m}^{-3}$ , while H1 being denser and L1 and L5 both being lighter. No clear pattern exists in the intermediate waters



**Figure 3.11:** Average summer (June-July, 2002-2008) transports (in Sv, integrated in  $0.01 \text{ kg m}^{-3}$  bins, positive northward) across  $\sim 60^\circ \text{ N}$  in the eastern North Atlantic (red line in inset; black lines show 1 and 2 km isobaths). Black crosses show density and strength of observed maximum northward and southward transports (Sarafanov et al., 2012). Dashed vertical lines indicate the observed boundaries between upper northward ( $\sigma_\theta < 27.55 \text{ kg m}^{-3}$ ), deep southward ( $\sigma_\theta > 27.8 \text{ kg m}^{-3}$ ), and intermediate waters in between. Numbers in parenthesis show net transport across the section and uncertainties (in Sv, given by authors for the observation and one standard deviation of this 14-month period for the models). Note that the shape and strength of the modeled transports does not change significantly if the annual long term average (January-December, 1961-2009) is used.

( $27.55 \leq \sigma_\theta \leq 27.80 \text{ kg m}^{-3}$ ). The average (June-July, 2002-2008) observed net transport across  $\sim 60^\circ \text{ N}$  has no distinct direction ( $0.1 \pm 3 \text{ Sv}$ , the rather large uncertainties are due to combination of different data sets, Sarafanov et al., 2012). All model solutions lie within these error bars. However, the H1 and H5 runs tend to show similar small net southward transports of  $-0.9 \pm 0.9 \text{ Sv}$  and  $-0.1 \pm 0.6 \text{ Sv}$  as the observations in contrast to the generally stronger L1 and L5 northward transports  $+1.2 \pm 0.5 \text{ Sv}$  and  $+1.3 \pm 0.4 \text{ Sv}$ , respectively. Here, the model uncertainty is given by one standard deviation of the same 14-month period as the observations. Note that these density distributions (Fig. 3.11) do not change the general results if the long term average (January-December 1961-2009) is used (not shown).

Fig. 3.12 shows the southward directed deep Denmark Strait overflow ( $v < 0 \text{ m s}^{-1}$ ,  $\sigma_\theta > 27.8 \text{ kg m}^{-3}$ ) through a section from Iceland to  $\sim 29^\circ \text{ W}$  (solid lines) as well as through a section from Iceland to Greenland (dashed lines).

The observed Denmark Strait overflow from Jochumsen et al. (2017) through a section from Iceland to 29° W is shown as reference (black and gray lines). The overflow transport through the section from Iceland to 29° W of L1 (light blue solid line) features a mean value of  $\sim -2$  Sv, while the corresponding transport in H1 shows an enhancement by  $\sim 75\%$  to a mean value of  $\sim -3.5$  Sv. With ongoing spinup the overflow transport is decreasing from L1 to L5 and from H1 to H5 by  $\sim 0.3$  Sv and  $\sim 0.6$  Sv, respectively. There is a larger variability on interannual time scales in the high-resolution model including periods of weaker (e.g. late 60s and late 70s) and stronger (e.g. mid 70s, mid 80s, and 2000s) transports in H5 compared to L5. In the late 90s, H5 exhibits a pronounced deep overflow increase of  $\sim 1$  Sv in a few years, followed by a slower  $\sim 0.75$  Sv decrease in the years 2000-2010 (the  $\sim 0.75$  Sv reduction is also seen in the low-resolution model). This rather steep overflow increase is somewhat weaker in the observations of Jochumsen et al. (2017) (black solid line) and accompanied by a much larger variability. The high-resolution overflows are in the range of the observations being approximately in the upper (H5) and lower (H1) bounds of the observed variability (20-day low pass filtered measurements, gray line in Fig. 3.12). Taking the deep overflow over the Greenland shelf into account (i.e. the full transport across Denmark Strait, dashed lines in Fig. 3.12), additional  $\sim 0.5-1$  Sv are transported southward. In general, no further temporal variability is added if the whole cross section is considered compared to the section from Iceland to 29° W. In H5, however, the eastern branch (from Iceland to 29° W) contributes almost entirely to the total overflow during phases of low overflow (e.g. late 60s and late 70s), which is not the case in H1.

Neither significant trends nor a seasonal cycle exist in the Denmark Strait overflow observations between 1996 and 2016 (Fig. 3.12 b). Linear trends between 1996 and 2009 of the modeled dense overflow (monthly time series) exhibit small p-values, indicating a significant trend. However, the corresponding coefficients of determination,  $R^2$ , are all close to zero why we reject the hypothesis that there are statistical significant trends (not shown). The high-resolution modeled overflow transport indicates a clear seasonal cycle with a maximum transport in winter and a minimum transport in summer (Fig. 3.12 b). With ongoing spinup, the H5 run shows an enhanced transport in February, March as well as in October and a minimum around June. The seasonal cycle of the overflow transport in L1 and L5 indicates a much weaker variability and resembles better the negligible seasonal cycle of the observed overflow

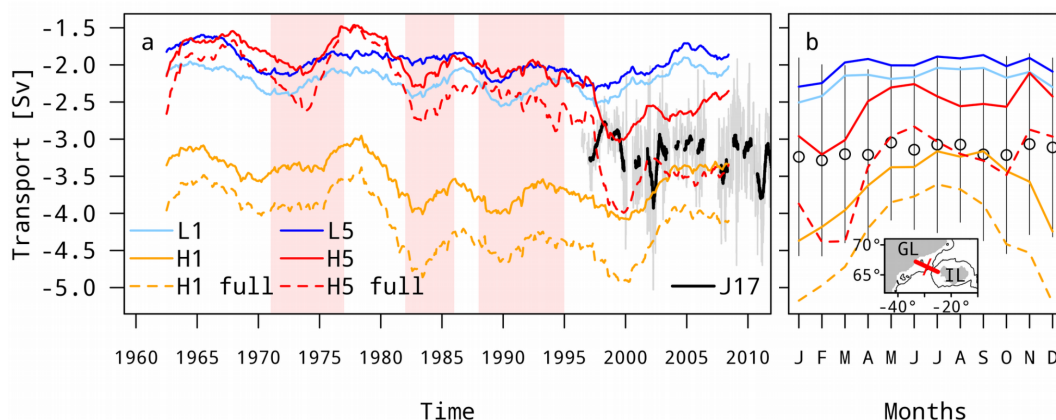


**Figure 3.12:** Deep overflow (in Sv, negative southward,  $\sigma_\theta > 27.8 \text{ kg m}^{-3}$ ) across Denmark Strait from Iceland to  $29^\circ \text{ W}$  (solid) and the full section from Iceland to Greenland (dashed, both cross section locations shown in b, thin black line shows 500 m isobath). a) Colored lines show 3-year low pass filtered 1st and 5th low- and high-resolution model results. Gray (black) line shows 20-day (6-month) low pass filtered measurements of Jochumsen et al. (2017). b) Average (1996-2009) annual cycle of deep overflow. Black circles and lines show the mean and one standard deviation of the observations. Red bars in a) show deep Labrador Sea MLD periods of the 5th high-resolution model spinup (H5, Fig. 3.17 b).

data but at a transport strength that is around 1 Sv weaker than the observed one.

Further downstream the WBC leaves the Irminger Sea southward along the Greenland coast. Fig. 3.13 shows the southward flow across  $\sim 60^\circ \text{ N}$  decomposed in the upper light ( $v < 0 \text{ m s}^{-1}$ ,  $\sigma_\theta < 27.8 \text{ kg m}^{-3}$ ) East Greenland/Irminger Current (EGIC) and the lower deep ( $v < 0 \text{ m s}^{-1}$ ,  $\sigma_\theta > 27.8 \text{ kg m}^{-3}$ ) WBC (DWBC) in summer (June-July, 2002-2008) integrated from South Greenland until  $38^\circ \text{ W}$ .

In both models the DWBC transport decreases in favor of the EGIC from the 1st to 5th spinup (due to colder and fresher conditions, not shown). In L5, the resulting DWBC transport is weaker than observed (black cross and box, Sarafanov et al., 2012). In H5, in contrast, both the EGIC and DWBC are in the range of observations after an initial too strong DWBC in the H1 run. Note that these density distributions do not change the general results if the long term average (January-December 1961-2009) is used (not shown).

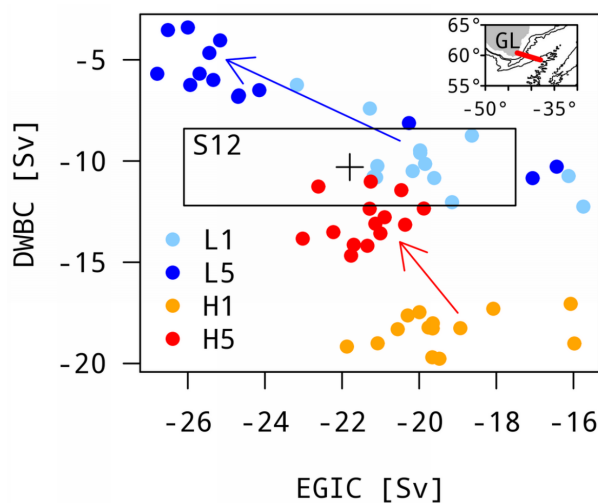


**Figure 3.13:** Monthly summer (June–July, 2002–2008) transports (in Sv, southward negative) of the East Greenland/Irminger Current (EGIC,  $\sigma_\theta < 27.8 \text{ kg m}^{-3}$ ) and Deep Western Boundary Current (DWBC,  $\sigma_\theta > 27.8 \text{ kg m}^{-3}$ ) across  $\sim 60^\circ \text{ N}$  from Southern Greenland until  $38^\circ \text{ W}$  (red line in inset; black lines show 1, 2, and 3 km isobaths). Colored arrows show transition from 1st to 5th spinups of low- (blue) and high-resolution (red) model runs. Black cross and box show mean and uncertainty of observations from (Sarafanov et al., 2012) for the same time period and location. Note that the shape of the modeled transports does not change significantly if the annual long term average (January–December, 1961–2009) is used.

### 3.4 Labrador Sea mixed layer restratification

Fig. 3.14 shows the water mass properties as a function of depth in the central Labrador Sea temporally and horizontally averaged over the period 1965–2004 and the index area shown in Fig. 2.5 and 3.15. Both models show in general denser waters than observed in almost the entire water column (Fig. 3.14 a and d, WOA13 from Locarnini et al. 2013 and Zweng et al. 2013, blue crosses; EN4 from Good et al. 2013, version 4.2.1, black dashed line). The dense biases reduce from the 1st to the 5th spinup due to colder (Fig. 3.14 b, e) and fresher (Fig. 3.14 c, f) conditions. In the upper  $\sim 100$  meter, H5 is the only run where the density as well as the salinity lie in the observed range (Fig. 3.14 a, c) although a notable cold water patch exists at the subsurface ( $\sim 50$ – $150$  m, Fig. 3.14 b).

This patch is absent in the L1 and H1 runs and weaker in L5. All other runs than H5 are too salty and too dense and exhibit a weaker stratification compared to observations. At mid-depth, L5 is closest to the observed salinity range, while all other model runs being too salty (Fig. 3.14 f). Below 2500

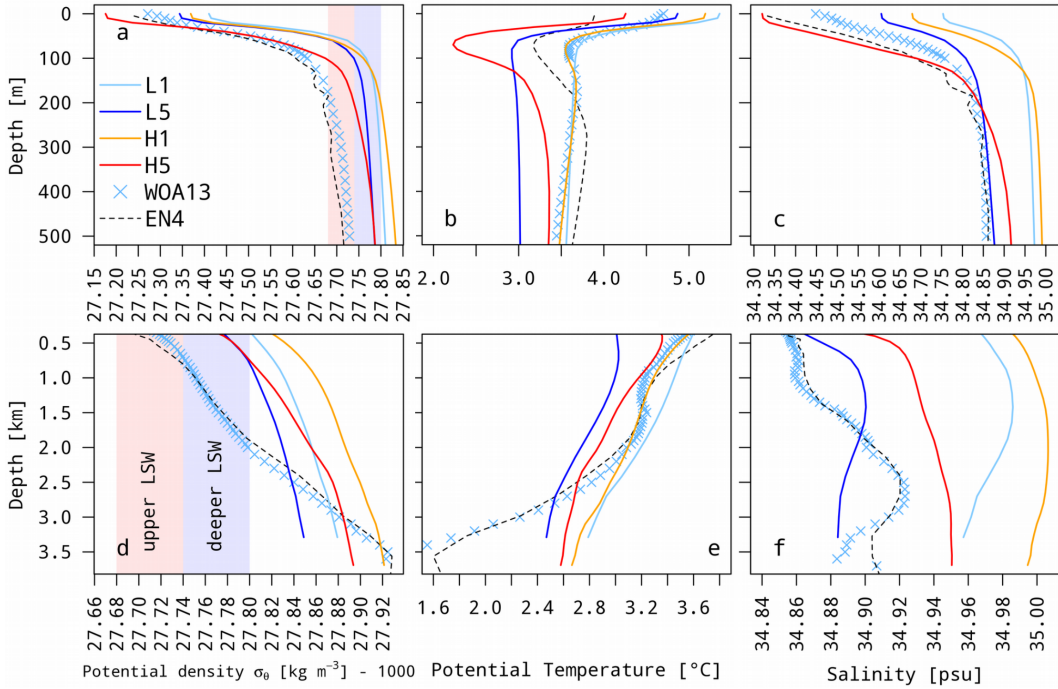


**Figure 3.14:** Average (1965-2004) upper 500 m (top row) and deeper (lower row) potential density  $\sigma_\theta$  (a and d, in  $\text{kg m}^{-3} - 1000$ ), potential temperature (b and e, in  $^\circ\text{C}$ ) and salinity (c and f, in psu) in the central Labrador Sea (white polygons in Fig. 3.15). Observations are from Locarnini et al. (2013) and Zweng et al. (2013) (both WOA13, blue crosses) and Good et al. (2013) (EN4, black dashed line) averaged over the same time period and area and linearly interpolated to regular depth levels. Red and blue shading in a) and d) shows upper and deeper (or classical) Labrador Sea Water density ranges.

meters, all models exhibit a warm bias (Fig. 3.14 e) that leads to lighter waters than observed (Fig. 3.14 d).

The average March (1961-2009) modeled North Atlantic mixed layer depth (MLD), defined as the depth at which the potential density deviates from the 10 m depth value by  $\Delta\sigma_\theta = 0.125 \text{ kg m}^{-3}$  (Monterey and deWitt, 2000; Danabasoglu et al., 2014), is confined to two areas: the Labrador Seas and the Nordic Seas (Fig. 3.15).

Observed (EN4, Good et al., 2013, Fig. 3.15 a) and modeled winter MLDs are very deep ( $> 3000 \text{ m}$  and up to bottom) in the Labrador Sea and shallower ( $\sim 2000 \text{ m}$ ) in the Nordic Seas. A longer model spinup leads to shallower MLDs in the high-resolution model (Fig. 3.15 d). The low-resolution MLD, in contrast, remains rather unchanged after 5 spinups (Fig. 3.15 c, differences

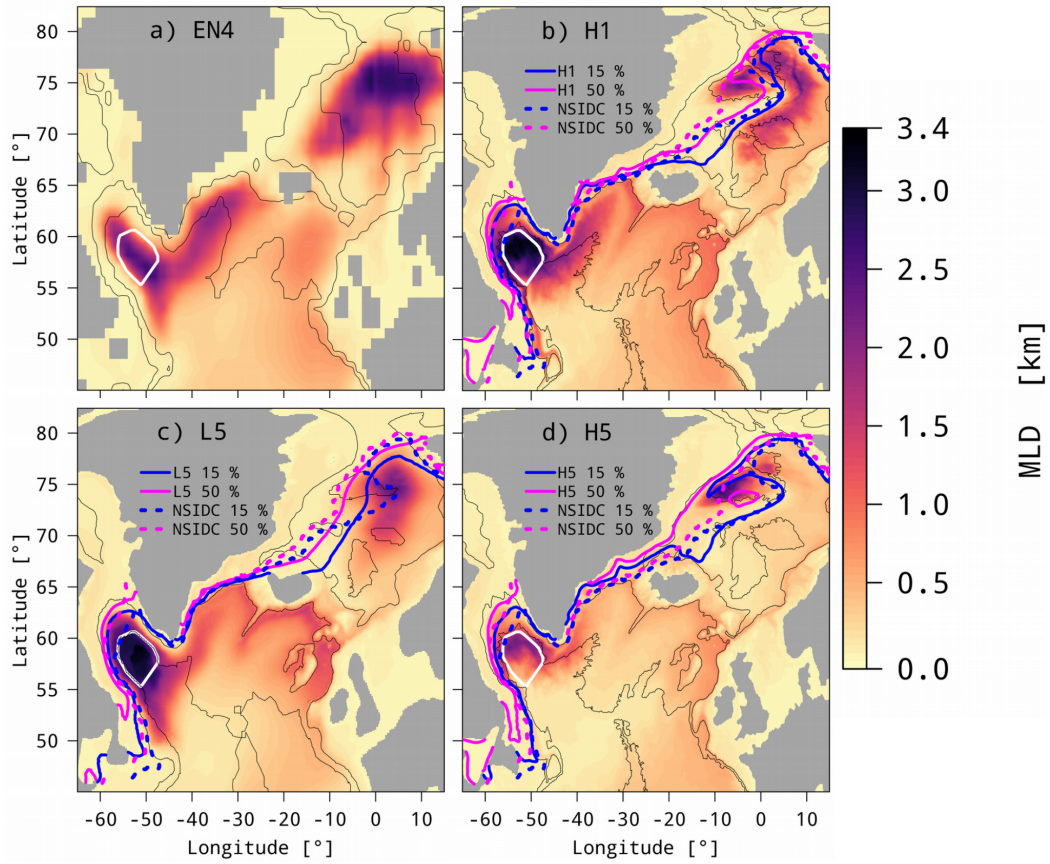


**Figure 3.15:** Average (1961-2009) March mixed layer depth (MLD, in km, defined as the depth at which the potential density  $\sigma_\theta$  deviates from its 10 m depth value by  $0.125 \text{ kg m}^{-3}$ ) of EN4 observations (a, [Good et al., 2013](#)), 1st high- (b) and 5th low- and high-resolution (c, d) spinups. Thin black lines are 1 and 3 km isobaths. Thick white polygons enclose the 3 km low-resolution model bathymetry in the Labrador Sea interior that is used for area averaging. Blue and magenta lines show the average (March, 1979-2009) 15 and 50 % sea ice concentration as modeled (solid) and measured (dashed) by satellites (NSIDC, [Cavalieri et al., 1996](#)). MLD differences between L1 and L5 are negligible and not shown.

to L1 are negligible and not shown). The average March (1979-2009) sea ice concentration (in %) as modeled (solid lines) and observed (dashed lines, NSIDC, [Cavalieri et al., 1996](#)) is added to Fig. 3.15. In both models the 15 and 50 % sea ice concentrations generally resemble those observed (Fig. 3.15 c and d). However, both models underestimate the sea ice concentration in the Labrador Sea. L5, in addition, overestimates the 15 % sea ice concentration in the Nordic Seas. A distinct sea ice change in the Nordic Seas is visible between the H1 and H5 runs, where the sea ice extent decreases with spinup time.

Especially the 50 % sea ice concentration is reduced in H5 and underestimates the one observed.

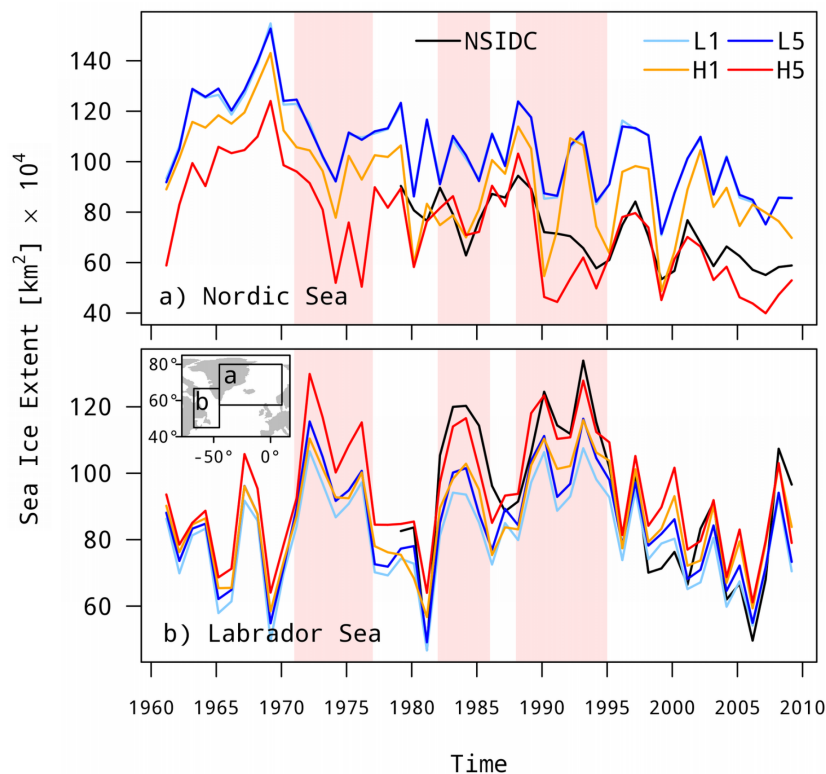


**Figure 3.16:** March sea ice extent (total area with sea ice concentration  $> 15\%$ , in  $\text{km}^2 \times 10^4$ ) in a) Nordic Sea and b) Labrador Sea basins (summation areas are shown in b). NSIDC (black line) are satellite observations from Cavalieri et al. (1996). Red bars show deep Labrador Sea MLD periods of the 5th high-resolution model spinup (H5, Fig. 3.17 b).

The March sea ice extent evolution in the Nordic Seas and the Labrador Sea is shown in Fig. 3.16 (total area with sea ice concentration  $> 15\%$ , in  $\text{km}^2 \times 10^4$ ). In both domains periods of lesser and greater sea ice extent are visible. In the Labrador Sea, periods of increased sea ice extent are in line with the modeled deep convection activity, indicated by red bars in Fig. 3.17 b. The high-resolution model exhibits a transition from the 1st to the 5th spinup: while the sea ice extent decreases in the Nordic Seas (Fig. 3.16 a), an increase is visible in the Labrador Sea especially during periods of deep convection (mid 1970s, mid 1980s, early to mid 1990s; Fig. 3.16 b). In both domains, this spinup transition yields sea ice extent as observed in the H5 run (black lines, NSIDC, Cavalieri et al., 1996). The low-resolution model, in contrast, overestimates (underestimates) the sea ice extent in the Nordic Sea (Labrador

Sea) and the spinup transition seen in the high-resolution model is almost absent.

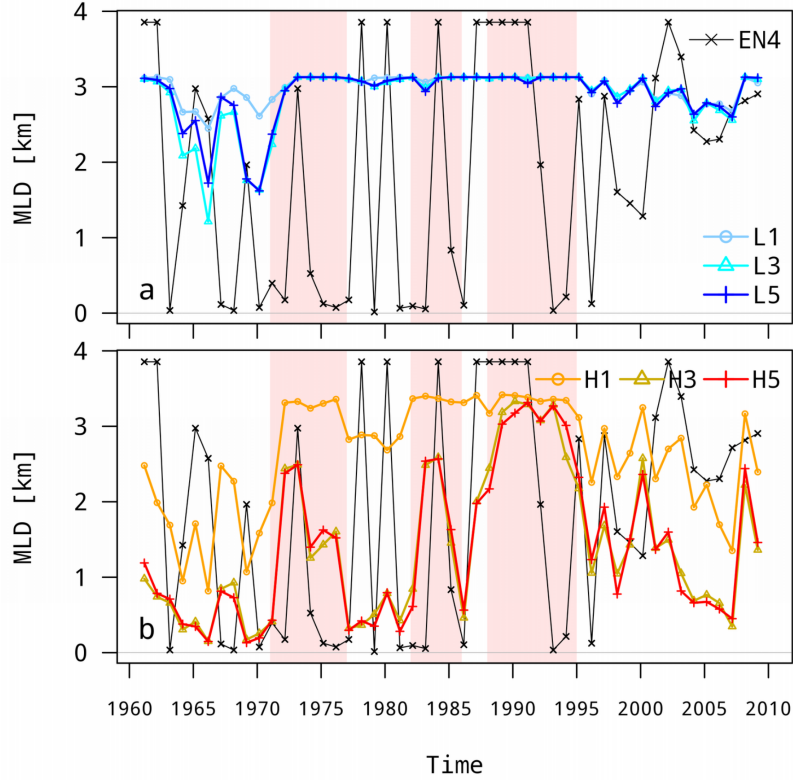


**Figure 3.17:** Decadal variability of average March MLD (in km; defined as the depth at which the potential density  $\sigma_\theta$  deviates from the 10 m depth value by  $0.125 \text{ kg m}^{-3}$ ; central Labrador Sea as indicated in Fig. 2.5 and 3.15) as modeled by low- (a) and high- (b) resolution models and observed (black, derived from EN4 data (Good et al., 2013) with the same MLD criterion as used in the models; identical in a and b; different maximum depths in the area yield different maximum MLDs compared to models). Note that a and b have the same y-axis. Red bars show deep Labrador Sea MLD periods of the 5th high-resolution model spinup (H5).

The decadal variability of the average March MLD in the Labrador Sea is shown in Fig. 3.17 (index areas indicated in Fig. 2.5 and 3.15). The modeled low-resolution winter MLD remains at great depths ( $\sim 3 \text{ km}$ ) throughout the entire simulated period and do not change with the number of spinup cycles (Fig. 3.17 a). In the high-resolution model, in contrast, a large interannual variability evolves with an increasing number of spinup cycles (Fig. 3.17 b). After 3 spinups, periods of shallow MLDs (e.g. late 1960s, around 1980, around 2005) are visible between periods of deep MLDs (e.g. early 1970s, around 1984, early 1990) indicating a restratification of the mixed layer. This restratifica-

tion is also visible in the observations (black crosses in Fig. 3.17, calculated based on the EN4, Good et al. (2013) with the same MLD criterion). Note that different maximum depths in the area yield different maximum MLDs compared to the models.

The average winter (January-March, 1965-2004) Labrador Sea hydrography is shown in Fig. 3.18. Similarly as for the annual mean (Fig. 3.14), a transition towards lighter waters is seen from the 1st to the 5th spinups in both models (Fig. 3.18 a) through colder (Fig. 3.18 b) and fresher conditions (Fig. 3.18 c).

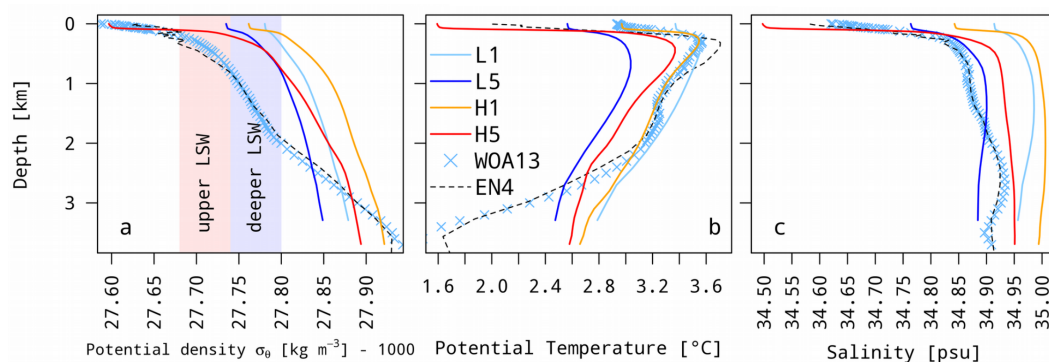


**Figure 3.18:** As Fig. 3.14 but for winter (January-March).

In particular the upper ocean pycnocline of the H5 run (red line in Fig. 3.18 a) is shallower and covers a wider density range compared to all other model runs, caused by fresh waters. Below 1 km depth the L5 run exhibits lighter conditions compared to all other runs, also caused by a lower salinity.

### 3.5 Discussion

Decreasing the horizontal model grid size down to the order of the first baroclinic deformation radius ( $O(1-10)$  km, e.g. Chelton et al., 1998) yields stronger and narrower currents with vigorous meanders in the North Atlantic Ocean compared to the low-resolution control experiment with a typical  $\sim 1^{\circ} \approx 100$  km resolution. The strength, position, and shape of the circulation in the H1 run generally resembles observations better (e.g. AMOC and total meridional oceanic heat transport; Fig. 3.3 and 3.4). The correct position of strong currents such as the Gulf Stream and North Atlantic Current (Fig. 3.5 b) leads

to distinct improvements of the upper ocean hydrography with respect to observations (Fig. 3.9 b). Similar improvements were observed in other high-resolution ocean modeling studies (e.g., Hurlburt and Hogan, 2000; Treguier et al., 2005; Bryan et al., 2007; Talandier et al., 2014; Marzocchi et al., 2015).

However, in both models (low- and high-resolution) the intermediate and deep circulation needs several spinup cycles ( $\sim 150$ -300 years) to develop (Fig. 3.2 and 3.3). During this spinup time the position of strong currents is not maintained in the high-resolution model and its positive effects seen in the H1 run partially vanish. In fact, H5 resembles the low-resolution control run L5 in terms of a too zonal Gulf Stream extension (Fig. 3.5) and upper ocean hydrographic biases (Fig. 3.9). This unexpected result was not seen in other high-resolution ocean modeling studies due to their rather short simulation lengths on the order of  $O(1-20)$  years (Treguier et al., 2005; Bryan et al., 2007; Rattan et al., 2010; Talandier et al., 2014; Marzocchi et al., 2015; Dupont et al., 2015; Hewitt et al., 2016; Iovino et al., 2016). For example, Marzocchi et al. (2015) found similar hydrographic improvements in the North Atlantic using a  $1/12^\circ$  configuration of the ocean model ORCA in a 30 years long simulation compared to a  $1^\circ$  control run (compare their Figure 4 a, c with Fig. 3.9 a, b).

The model biases in NAC and associated North Atlantic hydrography are also seen in other high-resolution ocean modeling studies (e.g., Sein et al., 2017). The incorporation of atmosphere-ocean corrections (Weese and Bryan, 2006) or feedbacks (Renault et al., 2016), on the other hand, yield realistic current paths and reduced hydrographic biases in ocean-only models. However, similar biases are known problems also in coupled atmosphere-ocean GCMs (Wang et al., 2014a; Menary et al., 2015). Wang et al. (2014a) attribute the cold bias to an AMOC reduction. We do see the same relationship (Fig. 3.3 and 3.9), however, it remains unclear why the position of the NAC is not stable throughout the spinup cycles.

Earlier studies found that the ocean model adjustment for Kelvin and Rossby waves strongly depends on the model resolution and viscosity, respectively (Cherniawsky and Mysak, 1989). In our high-resolution model, vertical displacements of several tens of meters magnitude propagate through the thermocline with a westward velocity of  $3.12 \pm 0.07 \text{ cm s}^{-1}$  (Fig. 3.6 b; similar patterns of several cm magnitude exist in the modeled high-resolution SSH field, not shown). In accordance with mid-latitude long planetary wave theory as well as observations we identify these propagations as long baroclinic Rossby

waves (Kessler, 1990; Chelton and Schlax, 1996; Chelton et al., 1998) and as a potential cause for the relatively strong upper ocean adjustment during the high-resolution model spinup. For example, the westward thermocline propagation identified in Fig. 3.6, representing the 1st baroclinic mode, would need around 8 years to cross the Atlantic (at 30° N the Atlantic basin width measures approximately 7891 km in both models). According to theory, long baroclinic Rossby waves with increasing vertical wave numbers  $m$ , each traveling with a velocity  $c_{R,m} = -\beta\lambda_{R,m}^2 \overset{\text{WKB}}{\approx} m^{-2} \{-\beta[(f\pi)^{-1} \int_{-H}^0 N(z)dz]^2\}$  where the  $m$ -th baroclinic (or internal) Rossby radius of deformation  $\lambda_{R,m} = c_{g,m}|f|^{-1}$  for latitudes  $\phi \geq 5^\circ$  with Coriolis parameter  $f$  and its meridional change  $\beta = \partial_y f$ , would exhibit a reduced speed by the factor  $m^{-2}$  (Chelton et al., 1998, a negative velocity indicates a westward directed Rossby wave). This implies that the associated 2nd and 3rd baroclinic modes already need around 32 and 72 years respectively to cross the Atlantic Ocean. In our model comparison we find that spatio-temporal propagation patterns of the first two baroclinic horizontal velocity modes  $R_1$  and  $R_2$  are of much larger amplitude in the high- compared to the low-resolution model (Fig. 3.8). Hence, in accordance with e.g. Cherniawsky and Mysak (1989); Chelton and Schlax (1996); Wunsch (1997); Clément et al. (2014) we argue that long baroclinic Rossby waves modify the upper ocean circulation and thereby lead to a stronger adjustment of the high-resolution upper ocean throughout the spinup cycles. In this context two technical aspects may need to be considered: 1) The unphysical jump, that is introduced at the beginning of every consecutive forcing cycle, may affect the wave propagation mechanism (Griffies et al., 2012). 2) The large differences between the horizontal resolutions also affect the strength the applied subgrid scale (SGS) closures for momentum and tracers. In areas of mesh refinement the average (1948-2009) depth-integrated SGS temperature flux is smaller by several orders of magnitude in the high- compared to the low-resolution model (compare Fig. 2.5 with Fig. 2.6; SGS temperature flux in  $^\circ\text{C m}^2 \text{ s}^{-1}$ ; the product of the eddy-induced velocity  $\mathbf{u}_{\text{SGS,h}}$  and potential temperature  $T$  was calculated at every model time step). The effects of the low-resolution SGS temperature fluxes on the modeled small-scale dynamics in the Labrador Sea will be described in chapter 4.

While the correctly modeled surface circulation (position and strength) of the H1 run is not maintained throughout the spinup cycles, a pronounced decadal variability of deep convection evolves in the Labrador Sea (Fig. 3.17 b), similarly to the one derived from observational EN4 data (Good et al., 2013). This variability is nearly absent in the low-resolution model and in H1 (and H2):

these runs show deep winter mixed layers through the whole forcing period (Fig. 3.17 a). Too deep winter MLDs are a typical problem of ocean general circulation models (Oschlies, 2002; Fox-Kemper et al., 2008; Danabasoglu et al., 2014, 2016; Heuzé, 2017) due to wrong current pathways, an insufficient vertical resolution, unresolved mixing processes but also an ill-defined mixed layer depth (usually via property difference to surface) through e.g. temperature-salinity compensation (Courtois et al., 2017).

Observations and models show a primarily wind-driven temporal variability of Labrador Sea deep convection (Kieke et al., 2007; Rhein et al., 2011; Yashayaev and Loder, 2016a; Scaife et al., 2014; Ortega et al., 2017). Since we use the same atmospheric forcing in all our model runs, we can conclude that the mean Labrador Sea hydrography is responsible for the agreement between the high-resolution modeled and observed MLD (Fig. 3.15 and 3.17 b). Only in the H5 run the slope of the winter (January-March) pycnocline is shallow enough (Fig. 3.18 a) to cover a density range large enough that the traditional MLD definition is meaningful (here via a potential density  $\sigma_\theta$  difference of  $0.125 \text{ kg m}^{-3}$ , Monterey and deWitt, 2000; Danabasoglu et al., 2014, see e.g. Holte and Talley (2009); Courtois et al. (2017) for an improved MLD definition based on linear fits of the full set of water mass properties, i.e. temperature, salinity, and density).

These lighter water masses in the Labrador Sea in the H5 run (Fig. 3.14 and 3.18) originate from the southeastward shifted NAC that is more zonal (Fig. 3.1 and 3.5), weaker (the maximum overturning at  $41^\circ \text{ N}$  is reduced towards observations; Fig. 3.3 b) and transports lighter water masses across  $\sim 60^\circ \text{ N}$  northward (Fig. 3.11) compared to all other model runs. As a consequence, the southward directed Denmark Strait overflow is strongly reduced from H1 to H5, but still being in the observed range (Fig. 3.12, Jochumsen et al., 2017). The low-resolution Denmark Strait overflow, in contrast, is clearly weaker than observed albeit the relatively high horizontal resolution of  $\sim 15 \text{ km}$  at the Denmark Strait (Fig. 2.5 a). This adaption of the deep overflow water with respect to lighter source water was also observed in Zhang et al. (2011). Further downstream the Western Boundary Current (WBC) leaves the Irminger Sea southward consisting of  $\sim 70 \%$  upper East Greenland/Irminger Current (EGIC,  $\sigma_\theta < 27.8 \text{ kg m}^{-3}$ ) and  $\sim 30 \%$  deep WBC (DWBC,  $\sigma_\theta > 27.8 \text{ kg m}^{-3}$ ) as observed during summer (June-July) 2002-2008 (Sarfanov et al., 2012, black cross and box in Fig. 10). This water mass distribution is represented in the H5 run after a transition from too dense waters in H1 (red

arrow in Fig. 10). The DWBC transport decreases by  $\sim 30\%$  (from  $\sim 19$  to  $\sim 13$  Sv) as the lighter EGIC transport slightly increases. This transition also exists in the low-resolution model ( $\sim 50\%$  reduction of DWBC from L1 to L5), however, in L5, the WBC is too light (blue arrow in Fig. 10).

In addition, the southeastward shift of the NAC from the H1 to the H5 run affects the Nordic Sea and Labrador Sea maximum (March) sea ice extent. While the models agree in the general spatial distribution (Fig. 3.15, blue and magenta solid and dashed lines), they generally overestimate (underestimate) the sea ice extent in the Nordic Sea (Labrador Sea) basins (Fig. 3.16). It is the H5 run that shows agreement with satellite observations in both basins (Cavalieri et al., 1996). The sea ice reduction in the Nordic Sea from H1 to H5 on the one hand and the increase in the Labrador Sea on the other results from the southeastward shift of the NAC (Fig. 3.5 b, d). In quasi-equilibrium, the NAC transports warm waters into the Nordic Seas across the sill between Iceland and Scotland which leads to a warm upper ocean temperature bias (Fig. 3.9 f) that reduces the overestimated sea ice of the H1 run (Fig. 3.16 a). At the same time the amount of heat transported along Reykjanes Ridge into the Labrador Sea decreases which leads to increased sea ice extent there (Fig. 3.16 b).

Hence, in our high-resolution model, the interplay of a long spinup adjustment and the large-scale circulation in the North Atlantic subpolar gyre seems to reduce typical model biases related to a salinification (Treguier et al., 2005; Brandt et al., 2007; Chanut et al., 2008; Rattan et al., 2010; Xu et al., 2013; Marzocchi et al., 2015) and a too deep mixed layer depth in the Labrador Sea (Oschlies, 2002; Fox-Kemper et al., 2008; Danabasoglu et al., 2014, 2016; Heuzé, 2017).

## **3.6 Conclusions**

With the global coupled finite element sea ice-ocean model FESOM we investigated the influence of a regionally increased resolution up to 5-15 km on the North Atlantic Ocean circulation and hydrography. Compared to our low-resolution ( $\sim 1^\circ$ ) control run, this high horizontal resolution leads to distinct improvements of the modeled oceanic circulation and water mass characteristics such as correctly positioned strong and narrow boundary currents, vigorous small-scale meanders and reduced upper ocean hydrographic biases. Similar

improvements were found in earlier studies (e.g., [Hurlburt and Hogan, 2000](#); [Treguier et al., 2005](#); [Bryan et al., 2007](#); [Talandier et al., 2014](#); [Marzocchi et al., 2015](#)).

However, we find that in our high-resolution model configuration, the upper ocean circulation changed considerably throughout the first three spinup cycles ( $\sim 180$  model years) before reaching a quasi-equilibrium state. During that spinup, a southeastward shift of the NAC decreases the upper ocean heat and salt transports into the Labrador Sea, leading to a reduced subpolar gyre salinification, shallower winter mixed layer depths in the Labrador Sea as well as a realistic sea ice extent. This adjustment of the upper ocean circulation was much weaker in our  $\sim 1^\circ$  control run. On the other hand, in quasi-equilibrium, the high-resolution model exhibits similar biases seen in the low-resolution model such as a too weak overturning and a pronounced North Atlantic upper ocean cold bias through the misplaced NAC.

We assume that the ocean adjustment is different for high and low model resolutions due to different representations of long baroclinic Rossby waves, consistent with earlier studies ([Cherniawsky and Mysak, 1989](#)). Slow westward wave propagations may be responsible for altering the modeled upper ocean dynamics on a decadal timescale in the high-resolution model as they are nearly absent in the low-resolution control run. Further research is necessary to identify the influence of baroclinic wave dynamics on the ocean model spinup adjustment.

Our study highlights the need of a spinup long enough to bring the model in a quasi-equilibrium state if a high horizontal resolution is used. With our current technology we are approaching high-resolution model studies in climate models (e.g., [Haarsma et al., 2016](#); [Hewitt et al., 2016](#)). Our results suggest that such experiments should be carefully compared to known low-resolution GCM deficits ([Wang et al., 2014a](#); [Menary et al., 2015](#)). As a logical next step, we will evaluate the spinup dynamics in coupled climate models.



## 4 Decadal variability of eddy temperature fluxes in the Labrador Sea

The interaction between the large-scale North Atlantic circulation and high-latitude deep convection was introduced in the preceding chapter. Here, the dynamics associated with small spatial and temporal scales is examined exemplarily for deep convection events.

*Declaration: this chapter is the final form of a manuscript that will be submitted for publication.*

### 4.1 Labrador Sea eddy temperature fluxes

Eddies are ubiquitous in the world ocean, particularly in vicinity of strong currents (e.g. Gulf Stream or North Atlantic Current, [Chelton et al., 2011](#)). Small-scale temperature  $T$  and salt  $S$  transports by mesoscale eddies modify sea water properties and thereby change the ocean circulation (i.e.  $T$  and  $S$  are “active” tracers). Similarly, biogeochemical nutrient fluxes such as chlorophyll concentrations are altered, affecting phytoplankton concentration and biomass production (e.g. [Danabasoglu et al., 1994](#); [Zhang et al., 2014](#)).

In the Labrador Sea, [Chanut et al. \(2008\)](#) and [Spall \(2004\)](#) suggest to distinguish between three different types of eddies, convective eddies (CE), boundary current eddies (BCE) and Irminger Rings (IR). The first type is directly linked to the baroclinic mixing that occurs when the weakly stratified water masses is surrounded by water masses of different densities. In this unstable situation, lateral mixing occurs and convective eddies (CE) form ([Chanut et al., 2008](#); [Lilly et al., 2003](#)). [Spall \(2004\)](#) and [Straneo \(2006\)](#) state that heat loss within a marginal sea is offset by lateral eddy fluxes originating in the boundary current. Hence, boundary current eddies (BCE) that are formed in the boundary current of the Labrador Sea such as the West Greenland Current (WGC) form the second type. The third type follows from barotropic instabilities triggered by horizontal shear of the velocity field, induced by changes of the bottom topography of the Irminger Current (IC) near Cape Desolation ([Eden and Böning, 2002](#)). In contrast to the BCE, these Irminger Rings (IR) are related to an enhanced eddy kinetic energy (EKE) and represent high energetic instabilities ([Saenko et al., 2014](#)).

To disentangle the involved dynamic and thermodynamic processes, the Boussinesq tendency eq. 2.8 for temperature  $T$  may be written in flux form as

$$\partial_t T = -\underbrace{\nabla \cdot (\mathbf{u} + \mathbf{u}_{\text{SGS}})}_{\text{Redi + GM}} T + \underbrace{\text{Forcing}}_{\text{eq. 2.16}} + \underbrace{\text{Rest}}_{\substack{\text{diffusion and} \\ \gamma_T \text{ from eq. 2.10}}} \quad (4.1)$$

To distinguish between temperature fluxes from long and short time scales, Reynolds averaging as introduced in section 2.3 and splitting the horizontal and vertical temperature flux components yields

$$\partial_t T = -\nabla_{\text{h}} \cdot (\overline{\mathbf{u}_{\text{h}}} \overline{T} + \overline{\mathbf{u}'_{\text{h}}} \overline{T'}) - \partial_z (\overline{w} \overline{T} + \overline{w'} \overline{T'}) - \nabla_{\text{h}} \cdot \overline{\mathbf{u}_{\text{SGS,h}}} \overline{T} - \partial_z \overline{w_{\text{SGS}}} \overline{T} + \frac{Q_{\text{net}}}{\rho c_p} + \text{Rest}, \quad (4.2)$$

where the overbar denotes a temporal mean and the prime a deviation from that mean (see section 2.3). As any vector transport may be given by a divergent and rotational component,  $\mathbf{u}T = (\mathbf{u}T)_D + (\mathbf{u}T)_R$  (Helmholtz theorem, see e.g. chapter 6 of Zdunkowski and Bott, 2003), using the flux form here is advantageous since the rotational part of the vector field does not affect the dynamics of the flow as noted by Marshall and Shutts (1981), Jayne and Marotzke (2002) and Fox-Kemper et al. (2003), and, by definition,  $\nabla \cdot (\mathbf{u}T)_R = 0$ , i.e. the rotational part is divergence-free. In the following, the modeled temperature budget in the dynamically important Labrador Sea is analyzed according to the relation above.

#### 4.1.1 Mean state

Since the Labrador Sea (LS) loses heat to the atmosphere through outgoing longwave radiation as well as sensible and latent heat fluxes (Fig. 4.1 c-d and Fig. 2.9), a dynamical counterpart is required by eq. 4.2. The average (1993-2009) horizontal surface circulation is characterized by the fast ( $>25 \text{ cm s}^{-1}$ ) West Greenland Current (WGC) following the southwest coast of Greenland northwestward and further downstream the eastern coast of Canada as the Labrador Current (LC) southeastward (Fig. 4.1 e-f). In contrast, the LS interior (region enclosed by the  $\sim 3 \text{ km}$  isobath) exhibits slow recirculation patterns and a southeastward directed stream at the boundary towards the open ocean. In the high-resolution model (5 km local horizontal resolution), the boundary currents are narrower and faster compared to the low-resolution control run ( $\sim 20 \text{ km}$  local horizontal resolution, Fig. 4.1 e-f). The transition

between the WGC and LC is separated into two main branches in the H5 run, while being one broad structure in the L5 run.

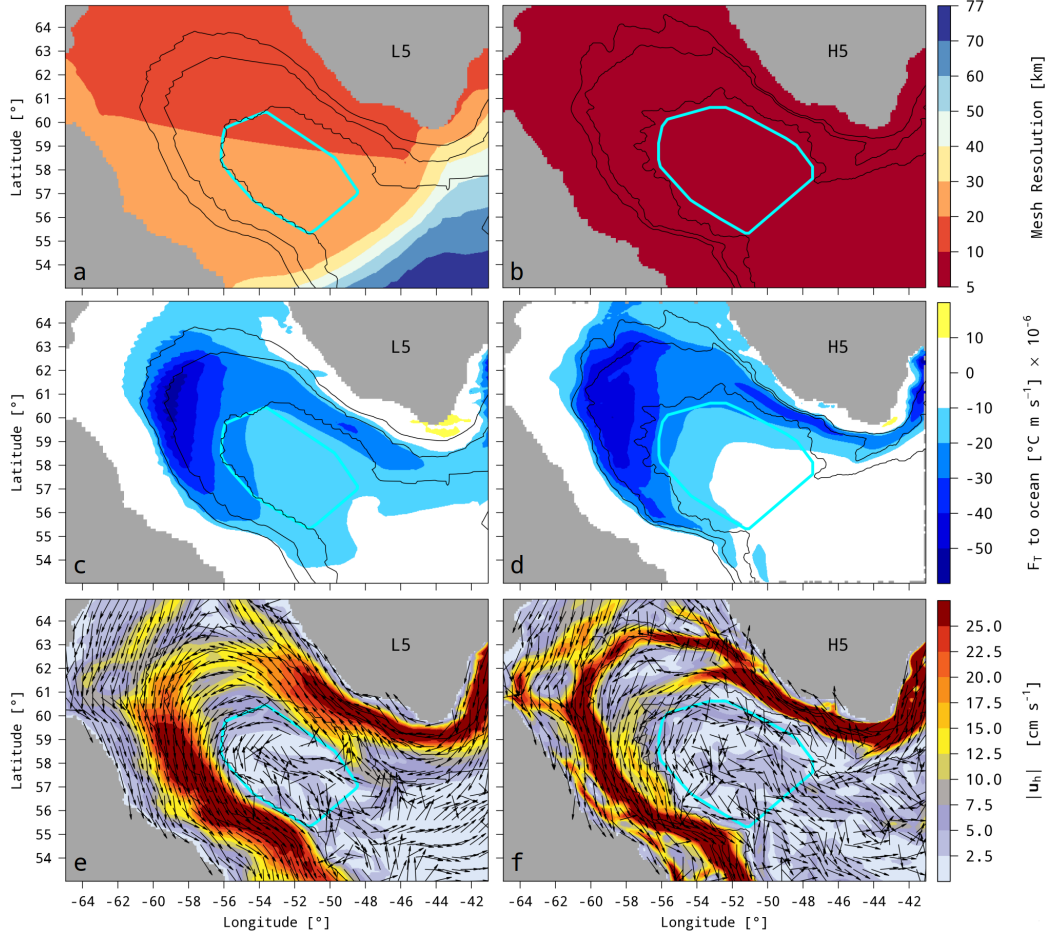


**Figure 4.1:** Horizontal mesh resolution of low- (a) and high-resolution (b) FESOM model configurations in the Labrador Sea (in km). Average (1948-2009) sea surface temperature flux  $F_T$  (eq. 2.16, negative values for temperature loss to the atmosphere in  $10^{-6} \text{ } ^\circ\text{C m s}^{-1}$ ) of 5th spinups of low- (L5, c) and high-resolution (H5, d) models. Average (1993-2009) sea surface velocity (in  $\text{cm s}^{-1}$ , colors) and direction (arrows, e-f). Blue polygon shows Labrador Sea interior index region. Black lines show the 1, 2 and 3 km model isobaths.

The average (1948-2009) depth-integrated horizontal divergence of the mean temperature advection is similarly structured as the mean circulation with main features along the coasts of Greenland and Canada (Fig. 4.2 a-b, positive values indicate negative divergence, i.e. a convergence, and hence a temperature or heat gain). The L5 run exhibits a large dipole structure of temperature loss on the onshore and temperature gain on the offshore side of the WGC. The sharp boundary between these two patches follows the mean circulation

throughout the LS basin (Fig. 4.1 e). Onshore of the LC, in addition, temperature is gained near the Canadian coast. The mean temperature advection is weaker in the LS interior compared to the boundary regions. Here, patches of heat divergence and convergence coexist next to each other. In the high-resolution model, in contrast, the mean advection exhibits a large number of heat divergence and convergence patches on relatively small spatial scales of tens to a few hundreds of km. Enhanced transports along the WGC and LC are also visible as in the L5 run. Here, however, the general structure is not as homogenous as in the low-resolution model. Several patches of heat divergence and convergence with small-scale features exist next to each other, similarly as for the mean circulation (Fig. 4.1 f). These features are nearly absent in the low-resolution model despite the relatively high horizontal model resolution of  $\sim 20$  km.

The eddy temperature advection, i.e. fluctuations of the temperature transport on temporal scales from the model time step to months (see section 2.3), is generally smaller by  $\sim 1$ -2 orders of magnitude compared to the mean temperature advection (Fig. 4.2 c-d). The largest fluctuations occur along the WGC and LC in both model setups. In the broad low-resolution WGC, temperature is lost in the region confined to the 2 and 3 km isobaths, where the mean current is located. At the on- and offshore sides of this patch, heat is gained. This feature of enhanced eddy temperature divergence/convergence is spatially limited to the WGC and weakens in magnitude directly after separation from the coast at  $\sim 53^\circ$  W. The low-resolution LC features a similar dipole as the mean advection with eddy heat convergence in the region bounded by the 1-2 km isobaths and eddy heat loss in the region of 2-3 km depth. The eddy and mean fluxes are of opposite sign in these areas (Fig. 4.2 a and c). In the LS interior, this is only the case in the southern part of the shown index area (blue line in Fig. 4.2). In the northern part of the LS interior, the mean and eddy fluxes are of the same sign. Here, similarly as for the mean advection, patches of eddy temperature flux divergence and convergence coexist. In the high-resolution model, temperature is lost due to eddy fluxes along the narrow WGC and gained on its onshore and offshore sides. In contrast to the L5 run, enhanced eddy advection persists after the separation from the coast (Fig. 4.2 d). In addition, the H5 run exhibits a second branch of enhanced eddy temperature fluxes along the WGC at  $\sim 64^\circ$  N. In contrast to the L5 run, mean and eddy advection along the high-resolution WGC and LC are of the same sign, especially along the 2 km isobath (Fig. 4.2 b and d). In the LS interior, however, mean and eddy fluxes are generally of opposite sign. As for

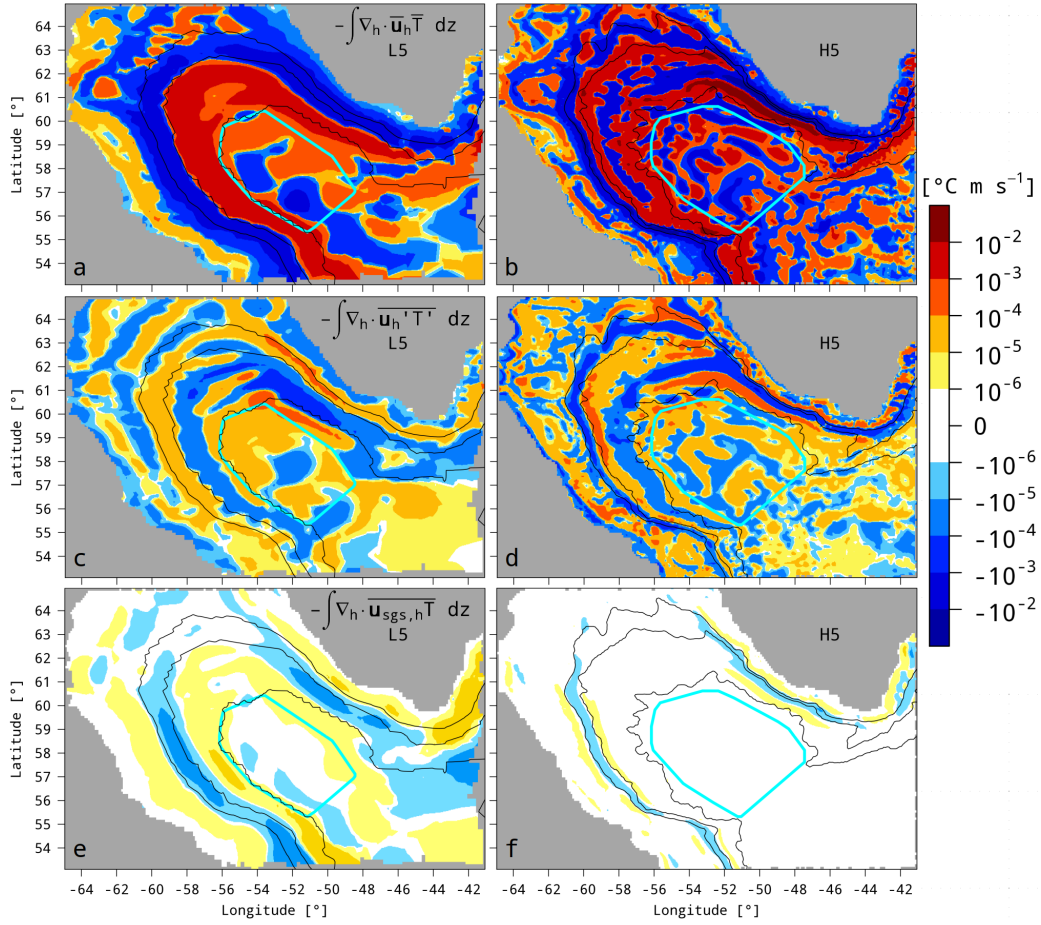


**Figure 4.2:** Average (1948-2009) depth-integrated mean (a-b), eddy (c-d) and sub-grid scale (SGS, e-f) horizontal temperature advection divergence of low- (L5, left) and high-resolution (H5, right) models in the Labrador Sea (positive values indicate temperature gain in  $^{\circ}\text{C m s}^{-1}$ ). Black lines show the 1, 2 and 3 km isobaths.

the high-resolution mean advection, numerous small-scale features are visible here as well as in the open ocean.

The temperature advection due to the parameterized sub-grid scale (SGS) fluxes is  $\sim 1$ -2 orders of magnitude smaller than the modeled eddy advection (Fig. 4.2 e-f). SGS fluxes are active along the fast boundary currents in both models and larger in amplitude in the low- compared to the high-resolution model. In both models, SGS and eddy advection have the same sign in the WGC region. In the LC region, in contrast, these fluxes are generally of opposite sign. In the LS interior, the SGS fluxes are small compared to the boundary current regions in both models.

### 4.1.2 Decadal variability

The sea surface temperature forcing  $F_T$  (eq. 2.16) in the LS interior (area-integrated over index region as shown in Fig. 4.1 and Fig. 4.2) exhibits periods of relatively strong heat loss to the atmosphere during e.g. the early 1970s, mid 1980s and early 1990s (in  $10^6 \text{ }^\circ\text{C m}^3 \text{ s}^{-1}$ , that can be considered as a volume temperature flux in  $^\circ\text{C Sv}$ , pink lines in Fig. 4.3). The modeled LS interior volume-integrated temperature tendency  $\partial_t \int T \text{ d}V$  (LHS, orange lines) directly responds to this atmospheric forcing via heat loss at the same time (negative values in Fig. 4.3). In the high-resolution model, the heat loss due to the atmospheric forcing is balanced by the volume-integrated total horizontal temperature advection (black line in Fig. 4.3 b) so that the sum of the forcing and the total advection nearly balance the modeled LHS (the negligible SGS advection is also included in the RHS). In this temperature budget, the residual between the LHS and RHS is given by the volume-integrated vertical advection, vertical SGS fluxes, horizontal and vertical diffusion as well as the non-local transport  $\gamma_T$  as introduced in section 2.1.2 and summarized in eq. 4.1 and 4.2. In the low-resolution model, in contrast, the shown equilibrium between total horizontal advection, SGS fluxes and atmospheric forcing is not given (Fig. 4.3 a). In fact, there is a large imbalance between the LHS and RHS, indicating that the diffusion and non-local transport terms play an important role in the low-resolution model run.

This imbalance arises through the horizontal mean and eddy temperature advection components (blue and red lines in Fig. 4.3). While in the H5 run the mean and eddy advection terms generally lead a temperature increase as opposed to the sea surface temperature forcing, a heat loss due to the mean advection is present in the L5 run throughout the forcing period. The temperature increasing but overall weak eddy and SGS contributions cannot compensate this heat loss (red and cyan lines in Fig. 4.3 a). In the high-resolution model, in contrast, the eddy part of the horizontal advection contributes significantly to the total advective temperature increase if volume-integrated over the whole LS interior (Fig. 4.3 b). If integrated over the mixed layer only, however, this high-resolution mean and eddy advection relationship changes. In this case, the mean temperature advection yields a temperature loss throughout the forcing period, as in low-resolution model (Fig. 4.4 b). As a consequence, eddy fluxes work against the mean circulation by providing heat to the mixed layer, yielding periods of a net advective heat gain during the mid-1980s and mid-1990s, whereas otherwise the mixed layer losses heat through advection.

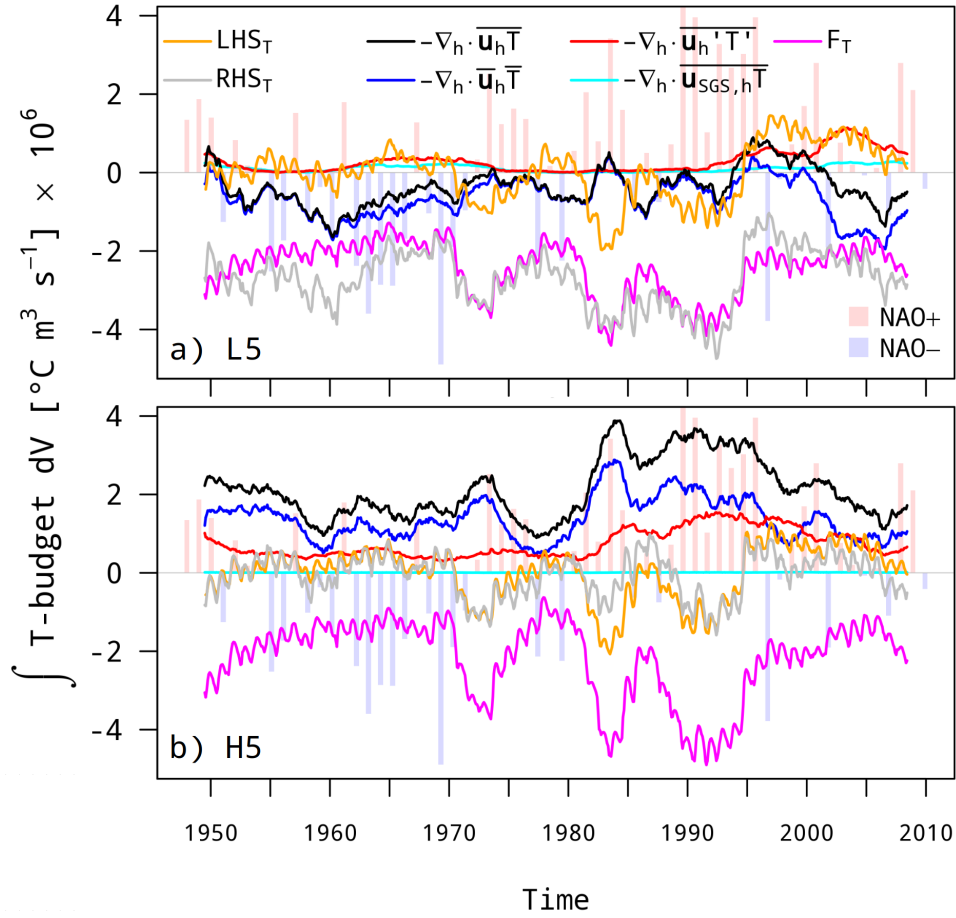


**Figure 4.3:** Temporal evolution of volume-integrated (index area shown in Fig. 4.1) temperature change  $\partial_t \int T dV$  (LHS, orange) of the low- (a) and high-resolution (b) models (positive values indicate a temperature gain in  $10^6 \text{ }^\circ\text{C m}^3 \text{ s}^{-1}$ ). The sum of the total (black) and sub-grid scale (SGS, cyan) horizontal temperature advection as well as the atmospheric forcing  $F_T$  (eq. 2.16, area-integrated, pink) is shown in gray (RHS). The total horizontal advection is given by mean (blue) and eddy (red) contributions as defined in section 2.3. A 3-year running mean is applied to all time series. Red (blue) bars in background indicate years with a positive (negative) NAO index on an arbitrary scale.

The strength of this eddy contribution varies similarly as the atmospheric sea surface temperature forcing  $F_T$  (pink lines in Fig. 4.3). The low-resolution eddy fluxes within the mixed layer, in contrast, do not balance the heat loss due to the mean circulation, also if the additional SGS fluxes are considered (Fig. 4.4 a).

Fig. 4.5 depicts the absolute eddy contribution as a fraction of the absolute total advection (in %), integrated over the whole volume (solid) and the mixed

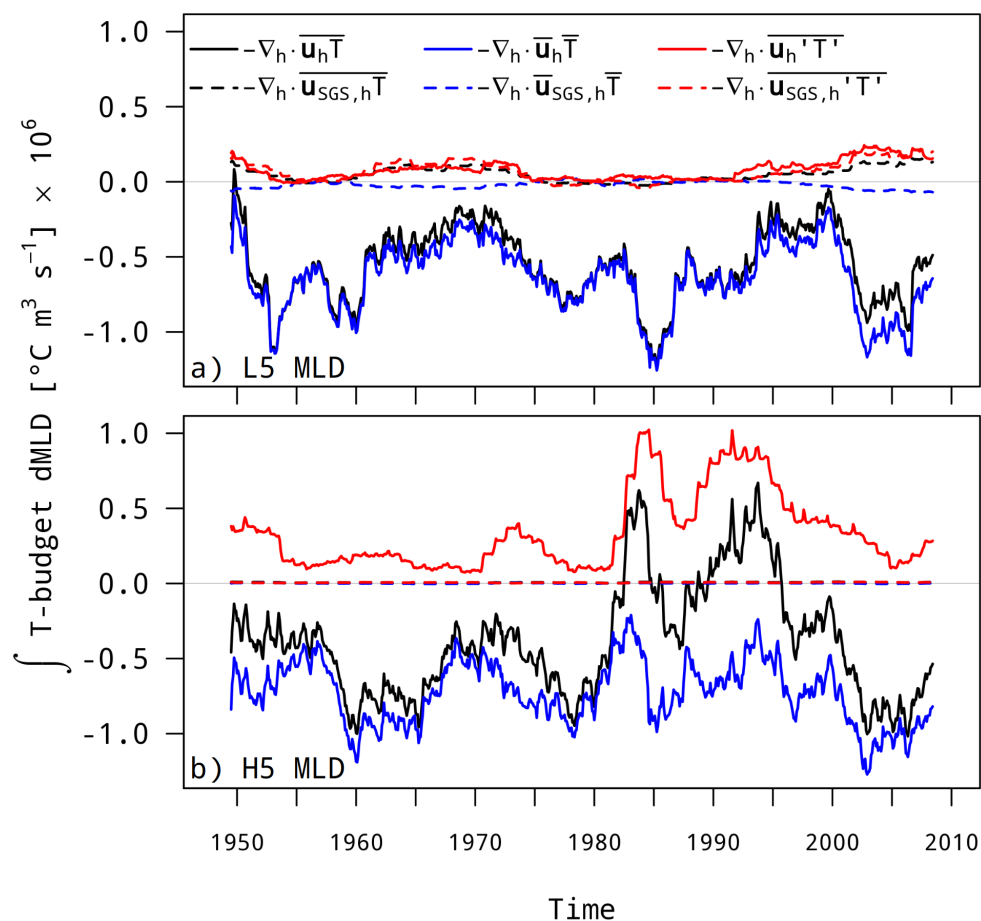


**Figure 4.4:** As Fig. 4.3 but integrated over the LS interior mixed layer only (index area shown in Fig. 4.1). Solid (dashed) black, blue and red lines show total, mean and eddy (SGS) advective terms, respectively.

layer (dotted lines). Around 1975 and 1985, during the mid- and late 1990s and early- to mid-2000s the high-resolution eddy fluxes contribute 40-60% to the total advection if integrated over the whole LS interior (solid red line in Fig. 4.5 b). During the mid-1950s, around 1970 and early 1980s, the contribution is smaller with  $\sim 20\%$ . The average LS interior winter (March) mixed layer exhibits a similar temporal evolution (black lines in Fig. 4.5, as in Fig. 3.17).

However, a temporal lag exists between the volume-integrated eddy advection contribution and winter MLD with an enhanced eddy activity several years after deep MLDs. If, in contrast, the advection terms are integrated over the mixed layer only, this lag vanishes and periods of large eddy advection contributions and deep winter MLDs are congruent (dotted red line in Fig. 4.5 b). During these events, the mixed layer-integrated high-resolution eddy

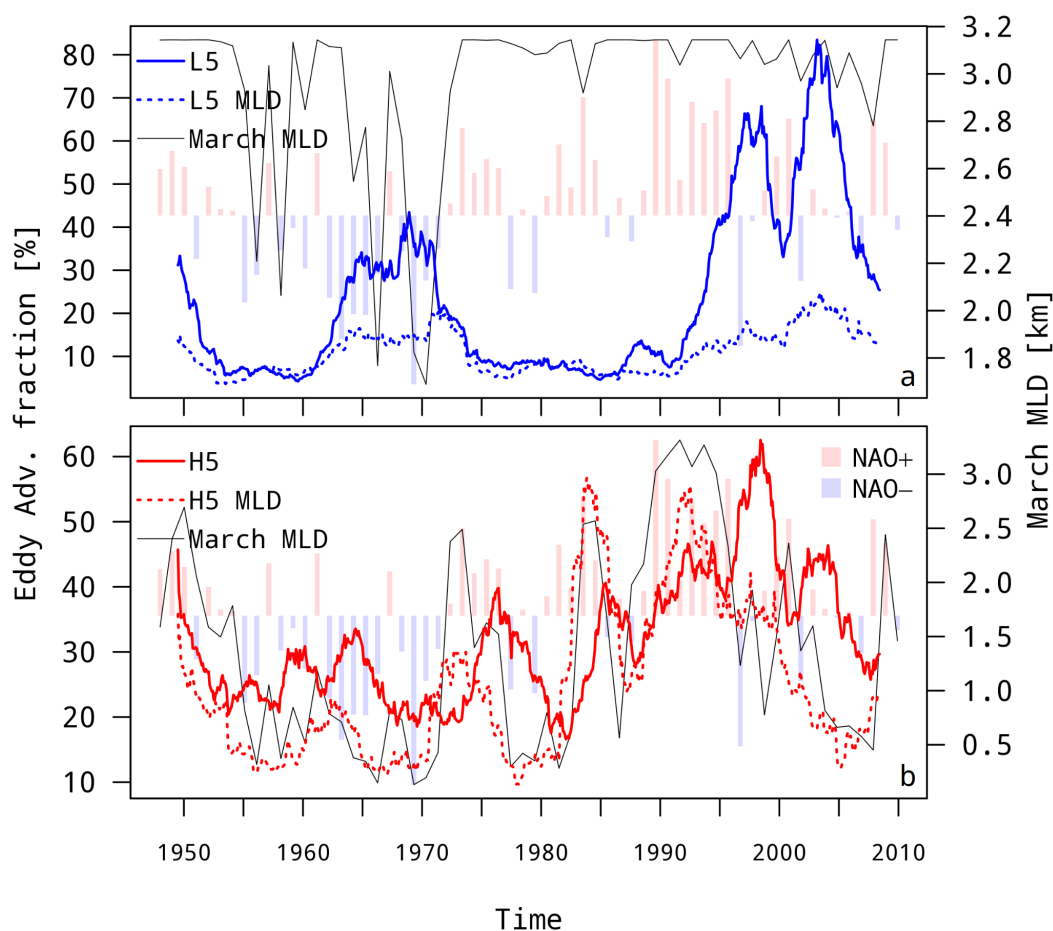


**Figure 4.5:** Temporal evolution of the eddy contribution to the total volume-integrated temperature advection in the Labrador Sea interior (in %, left axes) of low- (a) and high-resolution (b) models. Solid lines result from integration over the whole volume, dotted lines from integration over the mixed layer depth (MLD) only (index area shown in Fig. 4.1). Black lines show March MLDs (in km, right axes, same as in Fig. 3.17). A 3-year running mean is applied to the eddy fraction time series. Red (blue) bars in background indicate years with a positive (negative) NAO index on an arbitrary scale.

advection fraction ranges from  $\sim 30\%$  in the early 1970s to  $\sim 55\%$  around 1985 and in the early 1990s. During phases of shallow MLDs, integration over the mixed layer only yields eddy advection fractions of  $\sim 15\%$ , slightly lower compared to the full LS interior volume-integration.

In the low-resolution model, the eddy temperature flux generally contributes  $\sim 10\%$  to the total advection if integrated over the whole LS interior. However, from the early 1960s to early 1970s as well as during the late 1990s and early to mid-2000s the eddy fraction increases to 30-40% and 70-80%, respectively

(solid blue line in Fig. 4.5 a). During the former of these two periods, the low-resolution MLD is shallower compared to the remaining forcing period, hence showing the opposite behavior compared to the H5 run. During the second period of enhanced eddy fluxes, the MLD exhibits almost no variability and remains at large depths. Integration of the low-resolution advection terms over the mixed layer only yields no shift in time as seen in the high-resolution model. However, the magnitude of the eddy fraction during the two mentioned periods is strongly reduced to  $\sim 20\%$  (dotted blue line in Fig. 4.5 a).

## 4.2 Ambiguous salinity budget

The LS interior salinity  $S$  budget as derived for temperature outlined in the preceding section is shown in Fig. 4.6 for the high-resolution model run H5. In contrast to the atmospheric sea surface temperature forcing  $F_T$  (eq. 2.16), which leads to a cooling and hence an increased sea surface density throughout the forcing period (Fig. 4.3 b), the SSS forcing  $F_S$  (eq. 2.21) generally leads to a sea surface freshening and hence a reduction of the sea surface density (pink line in Fig. 4.6 b). This freshening results from the combined effect of precipitation, salinity relaxation and the (negligible) continental freshwater runoff, that exceeds the SSS increasing evaporation (see Fig. 2.9 for the individual components). As shown by the volume-integrated salinity change  $\partial_t \int S dV$  (LHS, orange lines in Fig. 4.6 b), periods of salinity gain/loss exist, similarly as for temperature. The total salinity advection divergence, however, is  $\sim 2$  orders of magnitude larger than the SSS forcing as well as the eddy advection and hence dominates the whole budget (RHS, gray line in Fig. 4.6 a). For clarity, the vertical mean salinity advection divergence is also shown here (blue dashed line). As a consequence, the remaining diffusion and non-local transport terms are supposed to balance the large mean salinity advection, although not playing a significant role for temperature (Fig. 4.3). Since these terms are not saved on disk, however, it remains unclear to us what causes this ambiguous salinity budget. Moreover, the density budget shows the similar imbalance between the forcing and total advection (not shown).

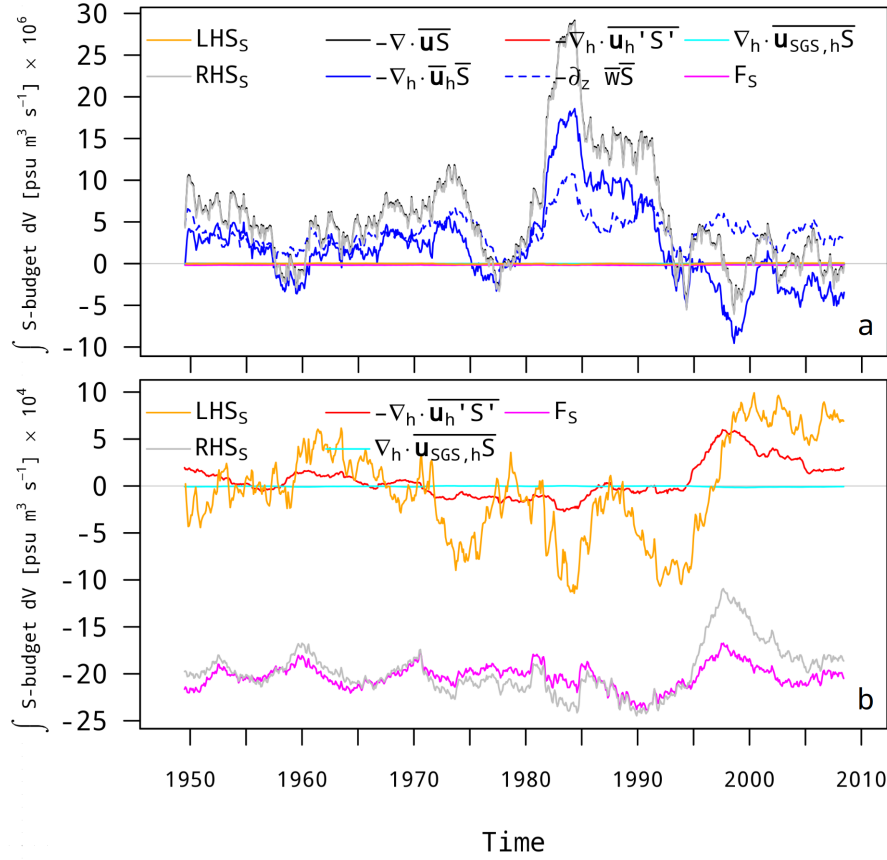


**Figure 4.6:** Temporal evolution of volume-integrated (index area shown in Fig. 4.1) salinity change  $\partial_t \int S dV$  (LHS, orange) of the high-resolution model (positive values indicate a salinity gain). The sum of the total (black) and horizontal sub-grid scale (SGS, cyan) salinity advection as well as the atmospheric forcing  $F_S$  (eq. 2.21, area-integrated, pink) is shown in gray (RHS). The total horizontal advection is given by mean (blue) and eddy (red) contributions as defined in section 2.3. The fluxes are given in  $10^6 \text{ psu m}^3 \text{ s}^{-1}$  (a) and in  $10^4 \text{ psu m}^3 \text{ s}^{-1}$  (b). A 3-year running mean is applied to all time series.

### 4.3 Discussion

The modeled small-scale temperature fluxes in the Labrador Sea exhibit a large variability in space and time, depending on the utilized model resolution. In the high-resolution run ( $\sim 5 \text{ km}$ ), eddies transport sufficient heat into the mixed layer to balance the temperature decreasing mean circulation. The eddy activity is further enhanced during periods of strong atmospheric forcing and deep convection (Fig. 4.3 b, 4.4 b and 4.5 b), in line with Labrador Sea water mass analyses and altimetry data (Yashayaev and Loder, 2016b; Zhang and

Yan, 2018). In the  $\sim 20$  km resolution control run, in contrast, the combined eddy and SGS fluxes are too weak to obtain this balance.

Other realistic ocean modeling studies utilizing a high horizontal resolution have shown a large eddy contribution to heat and freshwater convergence from the boundary current towards the Labrador Sea interior and associated restratification effects after deep convection events (Chanut et al., 2008; McGeehan and Maslowski, 2011; Saenko et al., 2014; Zhang and Yan, 2014; Kawasaki and Hasumi, 2014; Dukhovskoy et al., 2016). For example, multi-year average eddy advection contributions of 88 %, 86 % and 78 % in the LS interior are found by Chanut et al., 2008 (their Table 2), Saenko et al., 2014 (their Table 1, buoyancy is used as tracer) and Kawasaki and Hasumi, 2014 (their Table 1), respectively. Our high-resolution model run does not show this relatively high eddy contribution, which peaks at  $\sim 55$  % during periods of strong convection (dotted line in Fig. 4.5 b). Chanut et al. (2008) and Saenko et al. (2014) defined their eddy fluxes as deviations from a 5-year mean based on instantaneous fields every 2 days in the former and 2-day averages in the latter. These definitions yield eddy fluxes which represent rather an upper estimate since the variability from 2 days to 5 years is captured using these definitions. In contrast, our estimate includes the variability from the model time step to a month. As noted by Rieck (2014) and von Storch et al. (2012), and shown in section 2.3, these longer averaging periods likely yield higher eddy fluxes, and hence, their interpretation may be difficult. For example, our high-resolution total heat advection (around  $-0.5$  °C Sv, black line in Fig. 4.4 b) does not balance the stronger atmospheric forcing (around  $-3$  °C Sv, pink line Fig. 4.3 b) within the mixed layer, as it is the case in Saenko et al. (2014) (their Figure 10 a). This may originate from a lack of horizontal resolution since the utilized  $\sim 5$  km constitute rather the minimum possible resolution to capture submesoscale mixed layer instabilities on the order of  $O(1-10)$  km (Boccaletti et al., 2007, and chapter 5). However, how the eddy part is derived with respect to the mean, i.e. which temporal variability is captured, may be an important aspect, too.

As presented in chapter 3, the low-resolution mean circulation is in a different thermodynamic state compared to the high-resolution model run. Strong upper ocean salt transports into the LS interior yield too steep pycnoclines which prohibits mixed layer restratification (Fig. 3.14 and 3.18 in section 3.4). As such, these mean fluxes affect the volume-integrated tracer budgets. On average, the low-resolution mean circulation yields a temperature decrease, in

contrast to the temperature increasing high-resolution mean circulation (blue lines in Fig. 4.6). Observations indicate that eddies formed within or advected with the boundary current transport heat and salt (or freshwater) into the LS interior (Jones and Marshall, 1997; Lilly et al., 2003; Straneo, 2006; Rykova et al., 2009; de Jong et al., 2014; Rykova et al., 2015). This implies that the seawater properties of the boundary current directly set the restratification ability of the eddies. If no buoyant water is advected, as it is the case in our low-resolution model run, small scale fluxes may not contribute to restratification. This view is supported by model results of Gelderloos et al. (2011), Zhang and Yan (2014), Scholz et al. (2014) and de Jong et al. (2016), where, in the former two, a misplaced WGC leads to an underestimation of transports of heat into and convective water masses out of the LS interior by Irminger Rings. Hence, the limited capabilities of our low-resolution model to represent 1) small scale tracer fluxes and 2) the mixed layer restratification are due to a too large horizontal resolution of  $\sim 20$  km (Irminger Rings and boundary current eddies in this area were reported to exhibit radii of 11-50 km (Prater, 2002; Lilly et al., 2003; Hátún et al., 2007; Rykova et al., 2009; de Jong et al., 2014)) as well as the large-scale circulation upstream of the Labrador Sea that advects too dense water masses (see chapter 3).

The high-resolution boundary current, in contrast, provides buoyant seawater that can enter the LS interior via the mean flow and contribute to a temperature increase (Fig. 4.3 b), similarly as in Saenko et al. (2014). This balance between the atmospheric forcing and the modeled dynamics over the whole water column indicates a stabilizing effect from depths below the mixed layer. This is in contradiction to Kawasaki and Hasumi (2014) who find a destabilizing effect of mean heat fluxes when integrated over the whole water column. This may be explained through different index areas used for the budget calculation, as in our case a large negative contribution of the mean temperature advection between the index area and the 3 km isobath is excluded in the budget calculation (Fig. 4.2 b). This region of pronounced heat loss is also seen in Kawasaki and Hasumi (2014) and included in their heat budget for the LS interior (their Figure 8 b). Similar small-scale effects were found in Chanut et al. (2008), where the WGC bottom slope alone determined whether the mean heat advection leads to a heat gain or loss in the LS interior. Hence, vertical velocities near the steep bottom may be a potential explanation for the ambiguous salinity budget seen in our high-resolution model run (Fig. 4.6).

## 4.4 Conclusions

In this high-resolution ocean model study we show that the mean and small-scale eddy temperature fluxes contribute equally to the total temperature advection during phases of deep convection in the Labrador Sea interior. In addition, we find a large decadal variability of the eddy flux contribution, which was not simulated before with a realistic high-resolution ocean model on a  $\sim 5$  km horizontal resolution. Our results confirm earlier findings that the variability of the eddy strength is linked to the atmospheric forcing as well as the boundary current circulation upstream. The latter indicates that increasing the resolution locally may not be sufficient to model deep convection and restratification events and all involved dynamics. Instead, the boundary current needs to provide water masses buoyant enough to enable restratification when transported into the LS interior.

Following e.g. [von Storch et al. \(2012\)](#), we defined an eddy flux as the deviation from the mean, capturing the variability from the model time step (Tab. 2.1) to one month (see section 2.3). This methodological aspect may have a significant influence on the obtained eddy flux strength as shown by [Rieck \(2014\)](#) and noted by [von Storch et al. \(2012\)](#) and should be evaluated further in a systematic comparison in order to relate the involved spatial and temporal scales.

In addition, utilizing an ocean-only model configuration excludes important feedbacks between the ocean and the atmosphere. As shown recently, a decreased storm activity as expected through global warming leads to a reduction of sea surface heat loss and drastically reduced formation rates of water masses associated with deep convection in the Labrador Sea ([Garcia-Quintana et al., 2019](#)). Similarly, eddies affect the local atmospheric wind and precipitation conditions via turbulent heat fluxes in the eddy-rich Southern Ocean ([Frenger et al., 2013](#)). Hence, the interactions between the boundary current system and the LS interior during deep convection events will be investigated in a high-resolution coupled climate model study.

## 5 Eddy kinetic energy and mixed layer instabilities

In the last chapter significant contributions of small-scale temperature fluxes were identified in the high-resolution model run. The kinetic energy required to generate these small scale fluxes is provided through non-linear exchange processes across different spatio-temporal scales, referred to as the “inertial” range. Under the geostrophic assumption, when the flow is considered two-dimensional, two inertial ranges emerge for the conserved quantities energy and vorticity (or enstrophy, see section 11.3.2 of Vallis, 2017, and Fig. 5.1).

While the latter is carried from large to small scales within the vorticity inertial range due to turbulent interactions, the former is carried upscale from small to large scales within the energy inertial range. Vorticity, once arrived at very small scales, gets dissipated by molecular viscosity. At large scales, in contrast, energy is dissipated by friction. These aspects can be understood when considering the modeled vorticity and stream function in steady-state. While the former is represented by a large number of small-scale features which fill the ocean (see front-cover), the latter yields rather large circulation patterns such as gyres (see Fig. 3.1). Both represent, respectively, the “mesoscale” forward vorticity cascade and the inverse energy cascade, indicated by arrows pointing towards higher and lower wavenumbers in Fig. 5.1.

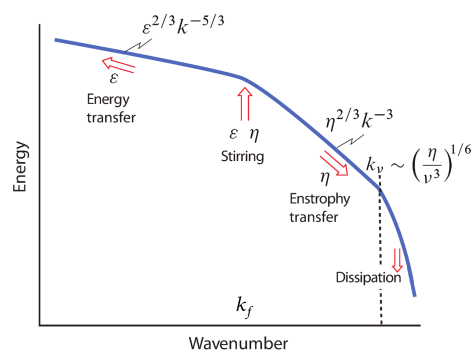


**Figure 5.1:** Energy spectrum according to two-dimensional turbulence: energy  $\epsilon$  and vorticity (or enstrophy)  $\eta$  are supplied at a forcing scale  $k_f^{-1}$  and subsequently transferred towards larger and smaller scales, respectively. Modified from Vallis (2017).

Based on this, different theories for quasi-geostrophic turbulence (QG) evolved, where the interior-QG (Charney, 1971) and the surface-QG (Blumen, 1978) are the most prominent. In the former, instabilities arise from potential vorticity gradients at depth. In the latter, they remain trapped to the surface in response to frontogenesis due to horizontal buoyancy gradients while maintaining a constant interior potential vorticity. Based on scaling laws, the kinetic energy spectrum as depicted in Fig. 5.1 rolls off proportional to the wavenumber  $k^{-3}$  in the interior-QG and proportional to  $k^{-3/5}$  in the surface-QG, i.e. flatter (Callies and Ferrari, 2013). Other sources of instability (or turbulence) exist, e.g. internal waves, tides, oscillations due to the planetary vorticity or turbulent flows within the mixed layer (mixed layer instabilities, MLIs). Approaching smaller scales, i.e. leaving the geostrophic regime towards Rossby

numbers  $Ro$  on the order of  $O(1)$ , routes to the “submesoscale” range. Recently, this most baroclinically unstable oceanic regime on the order of  $O(1-10)$  km is thought to play a key role in MLIs especially during winter, as observed by [D’Asaro et al. \(2011\)](#); [Callies and Ferrari \(2013\)](#); [Shcherbina et al. \(2013\)](#); [Callies et al. \(2015\)](#). Theoretical and modeling studies suggest that buoyancy gradients induce an ageostrophic circulation with high vertical velocities when isopycnals are sloped, which then lead to an efficient restratification of the mixed layer ([Haine and Marshall, 1998](#); [Lapeyre et al., 2006](#); [Boccaletti et al., 2007](#); [Fox-Kemper and Ferrari, 2008](#); [Capet et al., 2008](#); [Mensa et al., 2013](#); [Sasaki et al., 2014](#); [Brannigan et al., 2015](#)). In this sense, submesoscale dynamics represent the vertical counterpart to the mostly two-dimensional effects of mesoscale eddies as shown in chapter 4. In the following, the modeled kinetic energy spectrum of the Labrador Sea interior is derived and discussed in terms of the dominant processes which yield or remove eddy kinetic energy (EKE).

*Declaration: this chapter is in preparation for submission.*

## 5.1 Wavenumber Spectrum of a limited area

The spatial characteristics of a geophysical variable in wavenumber space provide insight about involved dynamics and quantify (non-linear) scale interactions, e.g. energy redistribution between different wavenumbers ([Nastrom and Gage, 1985](#); [Frisch, 1995](#); [Lindborg, 1999](#)). In addition, from a model perspective, resolved and unresolved processes can be distinguished ([Skamarock, 2004](#); [Olbers et al., 2012](#)). Different methods for obtaining one-dimensional (i.e. depending on a one-dimensional wavenumber  $k$ ) energy spectra  $S(k)$  were utilized before (see [Laprise, 2003](#), for an overview). Since we are interested in the kinetic energy spectrum of specific areas representing a dynamically consistent region (e.g. an ocean basin), we follow the limited area approach of [Errico \(1985\)](#) that was used in previous model studies (e.g. [Castro et al., 2005](#); [Bierdel et al., 2012](#); [Zentek et al., 2016](#)) and explained in the following section.

### 5.1.1 Spatial detrending

Let the two-dimensional variable  $\psi(x, y)$  along longitude  $x$  and latitude  $y$  directions be available on a regular grid  $a_{i,j}$  of dimension  $(n_x \times n_y)$  with  $i = (1, \dots, n_x)$ ,  $j = (1, \dots, n_y)$  and constant grid spacing  $\Delta$ . If  $a_{i,j}$  represents

a limited and not global domain, unresolved scales larger than the domain must be removed from the data to obtain a periodic boundary. This is done by the removal of spatial trends given by the boundary values of  $a_{i,j}$ . First, the spatial trend in  $y$ -direction,  $s_j$ , is removed from  $a_{i,j}$  for all longitudes so that

$$s_j = \frac{a_{n_x,j} - a_{1,j}}{n_x - 1}, \quad \tilde{a}_{i,j} = a_{i,j} - \frac{s_j}{2} (2i - n_x - 1). \quad (5.1)$$

Then, the spatial trend in  $x$ -direction,  $s_i$ , is removed from  $\tilde{a}_{i,j}$  for all latitudes:

$$s_i = \frac{\tilde{a}_{i,n_y} - \tilde{a}_{i,1}}{n_y - 1}, \quad \tilde{a}_{i,j} = \tilde{a}_{i,j} - \frac{s_i}{2} (2j - n_y - 1). \quad (5.2)$$

Note that  $a$  is replaced by the detrended field  $\tilde{a}$  from step 5.1 to 5.2.

### 5.1.2 One-dimensional wavenumber spectrum

The longitude  $x$  and latitude  $y$  directions can be represented by  $l_x = (0, \pm 1, \dots, \pm n_x/2)$  zonal and  $l_y = (0, \pm 1, \dots, \pm n_y/2)$  meridional wavenumbers  $p$  and  $q$ , evenly spaced by  $\Delta_p = 2\pi/[\Delta(n_x - 1)]$  and  $\Delta_q = 2\pi/[\Delta(n_y - 1)]$ , as

$$p = l_x \Delta_p, \quad q = l_y \Delta_q, \quad (5.3)$$

with the last  $n_x/2$  and  $n_y/2$  wavenumbers truncated in case of odd  $n_x$  or  $n_y$ . The discrete two-dimensional Fourier transform of  $\tilde{a}_{i,j}$  over  $p$  and  $q$  yields the two-dimensional spectral coefficients

$$c_{p,q} = \frac{1}{(n_x - 1)(n_y - 1)} \sum_{i=1}^{n_x-1} \sum_{j=1}^{n_y-1} \tilde{a}_{i,j} \exp\{-i\Delta[p(i-1) + q(j-1)]\}. \quad (5.4)$$

A common one-dimensional wavenumber  $k$  can be defined by the minimum fundamental ( $l = 1$ ) wavenumber  $\Delta_k = \min(\Delta_p, \Delta_q)$  such that  $k = l \Delta_k$  with  $l = (0, 1, \dots, n_x/2)$  if  $n_x \geq n_y$  or  $l = (0, 1, \dots, n_y/2)$  otherwise (last wavenumber truncated). The energy at a particular wavenumber  $S(k)$  can be inferred by summing the spectral coefficients  $c_{p,q}$  over discrete annuli  $A_k \in (k - 1/2 \Delta_k < (p^2 + q^2)^{1/2} < k + 1/2 \Delta_k)$  so that

$$S(k) = \sum_{p,q \in A_k} c_{p,q} c_{p,q}^*, \quad (5.5)$$

where  $*$  denotes the complex conjugate. The real part of  $S(k)$  represents the one-dimensional wavenumber spectrum of the two-dimensional variable

$\psi(x, y)$ . Then, following Lilly and Petersen (1983), the horizontal kinetic energy wavenumber spectrum is defined by the mean of the two zonal and meridional velocity wavenumber spectra  $S_u$  and  $S_v$  as  $S_{KE} = 1/2 (S_u + S_v)$ . Here, we use the monthly averaged horizontal surface velocity components  $u$  and  $v$  as modeled by FESOM to obtain  $S_{KE}$ .

### 5.1.3 Modeled kinetic energy wavenumber spectra

Fig. 5.2 shows the average (1961-2009) winter (March, solid) and summer (July, dashed lines) sea surface kinetic energy spectra  $S_{KE}$  as modeled by the low- and high-resolution models as well as inferred from observed geostrophic velocities (AVISO).

The high-resolution model exhibits two distinct regimes. First, a shallow spectrum proportional to  $k^{-5/3}$  on scales from  $\sim 300$ -100 km, with no seasonality. Then, from about 100 km, the spectrum continues steeper, following approximately the  $k^{-3}$  law towards smaller scales. In addition, a seasonality evolves with shallower slopes in winter compared to summer. At  $\sim 30$  km, the spectrum rolls off steeper than  $k^{-3}$ . The low-resolution kinetic energy spectrum, in contrast, does not show neither the  $k^{-5/3}$  nor the  $k^{-3}$  dependency, and is falling off steeper on all mentioned scales. A seasonality exists but is weaker in amplitude and appears throughout all spatial scales. The observed spectrum based on geostrophic velocities (AVISO) exhibits a  $k^{-5/3}$  spectrum at around 100-200 km and contains also higher energy levels than the low-resolution run. However, the energy is weaker compared to the H5 run and at around 100 km, the spectrum falls off steeper than both the H5 and the L5 runs.

The seasonal variability of the spectra is shown in Fig. 5.3. On scales smaller than 100 km, the H5 run exhibits spectral slopes shallower than  $-2.5$  in late winter (maximum in March-April), followed by steeper slopes around  $-3$  in summer (minimum in July), and a subsequent increase in autumn towards shallower slopes. The low-resolution spectrum falls off much steeper on these scales, proportional to  $k^{-4}$  in winter and  $k^{-4.5}$  in summer (the AVISO spectrum is even steeper and not shown here). If smaller scales are included in the linear regression to obtain the spectral slope (down to 25 km as indicated in Fig. 5.2), a drop towards steeper slopes is visible in the high-resolution spectrum and  $-3$  slopes are reached only in winter. The seasonality, however, remains (dashed and dotted lines in Fig. 5.3 a). Considering the whole forcing period, the high-resolution  $S_{KE}$  slopes are shallower during periods of enhanced

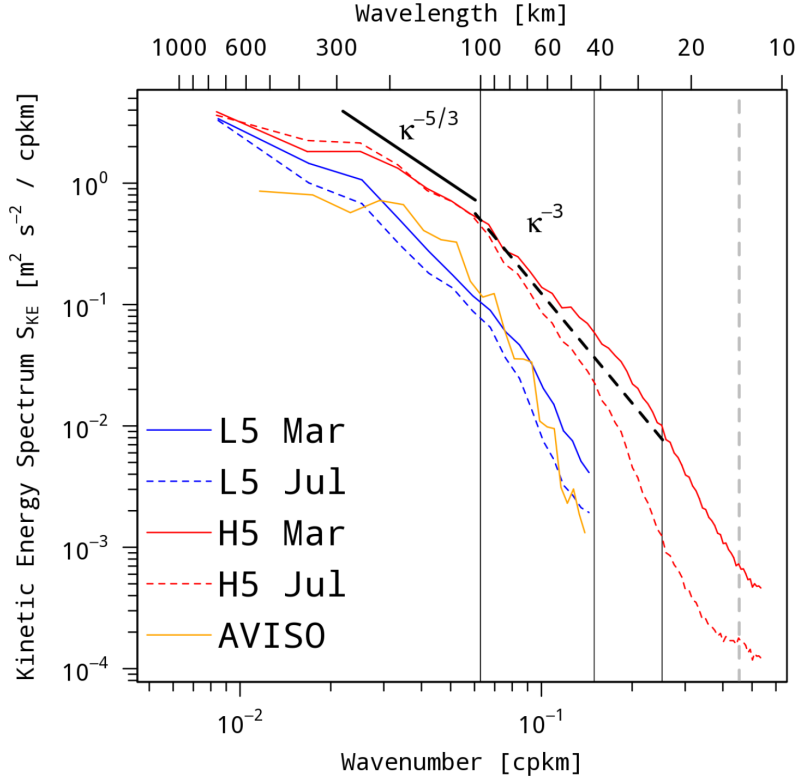


**Figure 5.2:** Average (1948-2009) March (solid) and July (dashed) sea surface kinetic energy wavenumber spectrum  $S_{KE}$  in the LS interior (index area shown in Fig. 4.1) of low- (black) and high-resolution (red) models. Blue lines shows average (1993-2009) spectrum derived from geostrophic velocities (AVISO). The spectrum is given in  $m^2 s^{-2}$  per cycles per km as a function of wavenumber  $k$  (in cycles per km, lower axis) and wavelength (in km, upper axis). Thick black solid and dashed lines indicate slopes of  $k^{-5/3}$  and  $k^{-3}$ , respectively. Vertical dashed gray line indicates the first baroclinic Rossby radius of deformation  $\lambda_{R,1} = (\pi |f|)^{-1} \int_{-H}^0 N(z) dz = 13.86$  km based on average (1955-2012) WOA 2013 data (Locarnini et al., 2013; Zweng et al., 2013). Vertical black lines show wavenumber ranges for linear regressions of  $S_{KE}$ .

atmospheric forcing and deep convection events. Thereby, the slopes approach  $-2$  in the early 1990s (Fig. 5.3 b; see chapters 3 and 4). This relation is not as pronounced in the low-resolution model. Including smaller scales around 25 km yields the same behavior as for the seasonal cycle. While the spectral slopes are well above  $-3$  on scales from 100 to  $\sim 40$  km during the whole forcing period, they continuously drop to steeper values below  $-3$  if scales around 25 km are included (dotted line in Fig. 5.3 b).

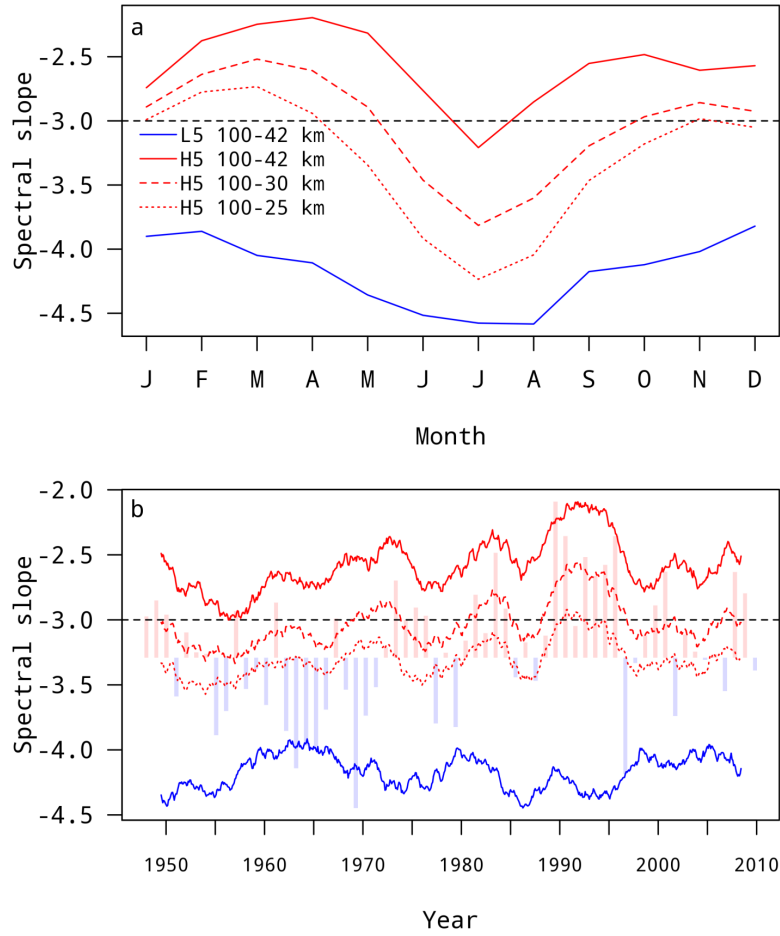


**Figure 5.3:** Average (1948-2009) annual cycle (a) and decadal evolution (b) of spectral slopes of the kinetic energy spectrum  $S_{KE}$  inferred by linear regression between the indicated scales for low- (blue) and high-resolution (red) models. Larger values indicate a shallower slope. Horizontal dashed lines mark the  $-3$  slope. A 3-year running mean is applied to the decadal time series. In b, red (blue) bars in background indicate years with a positive (negative) NAO index on an arbitrary scale.

## 5.2 EKE variability

While kinetic energy passes across scales as shown above, turbulent kinetic energy is generated or removed from the system. To identify the processes which determine the eddy kinetic energy (EKE), the Lorenz Energy Cycle (LEC, Lorenz, 1955) of the ocean was used in modeling studies by e.g. Marchesiello et al. (2003); von Storch et al. (2012); Renault et al. (2016); Wekerle et al. (2017). The volume-integrated EKE tendency equation, which can be derived

from the hydrostatic Boussinesq momentum balance (see chapter 12 of [Olbers et al., 2012](#)), yields the following four EKE conversion terms

$$F_e K_e = \frac{1}{\rho_0} (\overline{\mathbf{u}'_h \cdot \boldsymbol{\tau}'}) \quad (5.6)$$

$$HRS = -\overline{u'^2} \frac{\partial \bar{u}}{\partial x} - \overline{u'v'} \frac{\partial \bar{u}}{\partial y} - \overline{u'v'} \frac{\partial \bar{v}}{\partial x} - \overline{v'^2} \frac{\partial \bar{v}}{\partial y} \quad (5.7)$$

$$VRS = -\overline{u'w'} \frac{\partial \bar{u}}{\partial z} - \overline{v'w'} \frac{\partial \bar{v}}{\partial z} \quad (5.8)$$

$$P_e K_e = \overline{w'b'} = -\frac{g}{\rho_0} \overline{w'\rho'} \quad (5.9)$$

$F_e K_e$  represents eddy growth due to wind anomalies at the sea surface and can be understood as a mechanical source of instability. The horizontal and vertical Reynolds stresses  $HRS$  and  $VRS$  yield EKE from barotropic shear instabilities of the mean flow involving horizontal and vertical shear ( $VRS$  likewise represents Kelvin-Helmholtz instability). Formulated together,  $HRS$  and  $VRS$  yield the transfer from mean kinetic to eddy kinetic energy. The last term  $P_e K_e$  is associated to baroclinic instability through the exchange between turbulent potential and kinetic energy. These energy conversions are defined such that if positive, EKE is generated at the expense of the mean flow. In turn, if negative, EKE is transferred back to the mean flow by turbulence.

Fig. 5.4 shows the average (1948-2009) barotropic and baroclinic EKE generation terms in the LS interior as a function of depth (in  $10^{-10} \text{ m}^2 \text{ s}^{-3}$ ). Barotropic instability generally removes turbulent kinetic energy, especially near the surface. The high-resolution  $HRS$  is additionally intensified near the bottom. In the low-resolution model, in contrast, this term yields weak EKE generation between surface and bottom (blue line in Fig. 5.4 b). The horizontal shear leads to a stronger EKE removal by 1-2 orders of magnitude compared to the vertical counterpart in both models. The depth-integrated barotropic instability is several times large in the high- compared to the low-resolution model run (Fig. 5.4 b, d). Baroclinic instability, in contrast, generates EKE throughout the water column in both models. In addition to large values near the surface,  $\overline{w'b'}$  is also enhanced in the upper 1-2 km depth. This aspect is pronounced much more in the high-resolution run. Hence, depth-integrated values of baroclinic instability are much larger in magnitude compared to the barotropic instabilities (Fig. 5.4 f).

The wind generates a large amount of turbulent kinetic energy, especially during winter in both models (Fig. 5.5 a). The interactions between the sea

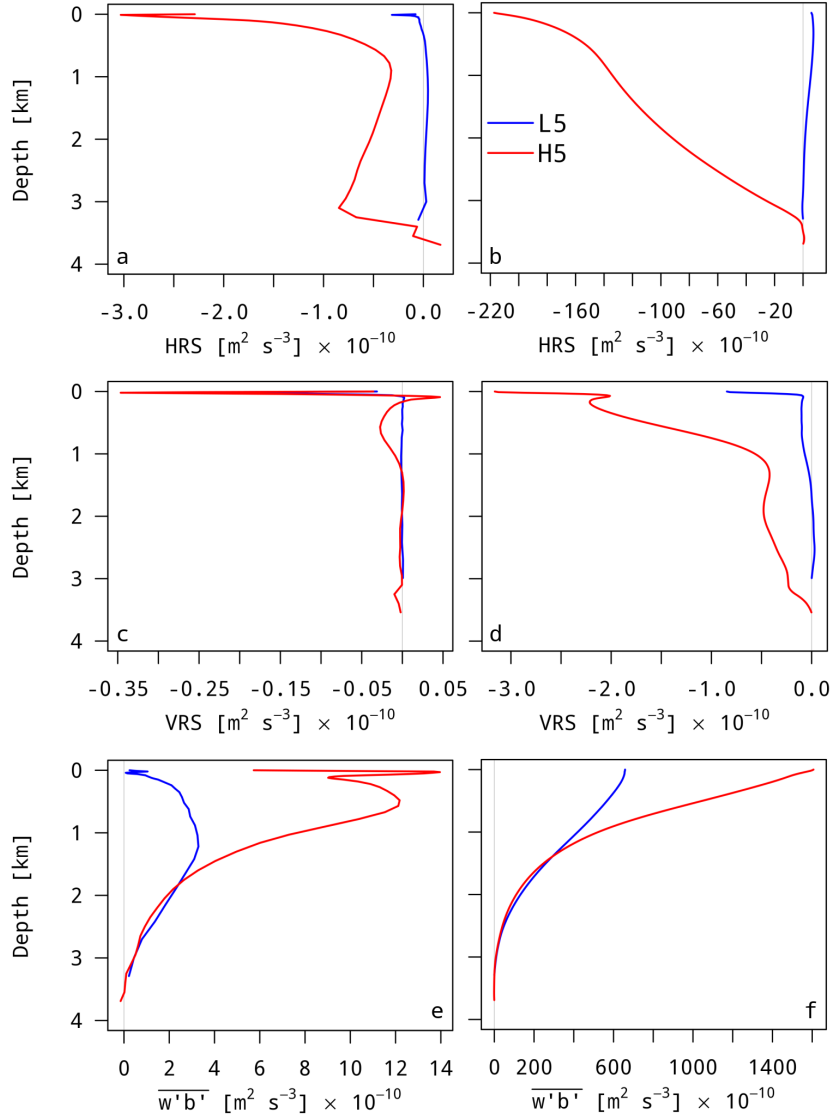


**Figure 5.4:** Average (1948-2009) barotropic horizontal ( $HRS$ , eq. 5.7, a-b) and vertical ( $VRS$ , eq. 5.8, c-d) Reynolds stresses and baroclinic instabilities ( $P_e K_e$ , eq. 5.9, e-f, all in  $10^{-10} \text{ m}^2 \text{ s}^{-3}$ ) of low- (blue) and high-resolution (red) models, area-averaged over the LS interior (index area shown in Fig. 4.1) as a function depth (left) and integrated from the bottom (right). A positive term generates EKE at the expense of the mean flow. Note the different scales.

surface and variable winds lead to an enhanced EKE generation in the high-resolution model in early to late winter (January to March). This effect is not present in late autumn. In contrast, the high-resolution depth-integrated barotropic and baroclinic conversion terms are enhanced only in late winter, mainly March, while remaining at lower levels during the rest of the year.

This aspect is almost absent in the low-resolution control run (Fig. 5.5 c, e, g). Likewise, this is the case over the whole forcing period from 1948 to 2009. The depth-integrated high-resolution barotropic and baroclinic instability terms are strongly enhanced during phases of intensified atmospheric forcing and deep convection in the early 1970s, mid-1980s and early to mid-1990s (Fig. 5.5 d, f, h; see Fig. 5.3 and Fig. 3.17 for comparison). The EKE generation through variable winds, on the other hand, does not show these pronounced events (Fig. 5.5 b). Here, moreover, the differences between the models are small, in contrast to all other terms. The combined EKE generating effects of mechanic and baroclinic instabilities are by far larger than the EKE removing barotropic instabilities *HRS* and *VRS* in both models.

### 5.3 Discussion

In accordance with two-dimensional turbulence theory the kinetic energy spectra as modeled with FESOM yield two distinct inertial ranges in the dynamically active Labrador Sea interior. The high-resolution ( $\sim 5$  km) spectrum exhibits a wavenumber  $k^{-5/3}$  dependency on scales of  $O(100)$  km. Hence, these scales are characterized by surface-QG turbulence associated with surface-intensified fronts induced through mesoscale eddies, which act to restratify the mixed layer (Lapeyre and Klein, 2006; Lapeyre et al., 2006). On smaller scales from 100 to  $\sim 25$  km the kinetic energy spectrum is proportional to  $k^{-3}$ , thereby representing interior-QG turbulence. Here the spectrum exhibits a pronounced seasonality, with shallower slopes during winter, in line with in-situ observations from dynamically active regions in the vicinity of the Kuroshio and Gulf Stream (D’Asaro et al., 2011; Callies and Ferrari, 2013; Callies et al., 2015) as well as high-resolution model studies (Mensa et al., 2013; Sasaki et al., 2014; Brannigan et al., 2015; Renault et al., 2016). This feature is associated with submesoscale turbulence and distinct from surface-QG turbulence (Callies et al., 2015). The shallower winter kinetic energy spectral slopes exhibit values around  $-2.5$  and approach  $-2$  during periods of strong convection (Fig. 5.3). This was also observed by Callies and Ferrari (2013); Callies et al. (2015). The reason for these shallower slopes, however, remain unclear. LaCasce (2012) infers a  $-2$  slope for surface-QG flow with constant stratification. This could be a similar case here since the mixed layer in the Labrador Sea interior yield a deep near-constant stratification. Ageostrophic velocities, on the other hand, are not considered in two-dimensional turbulence and may

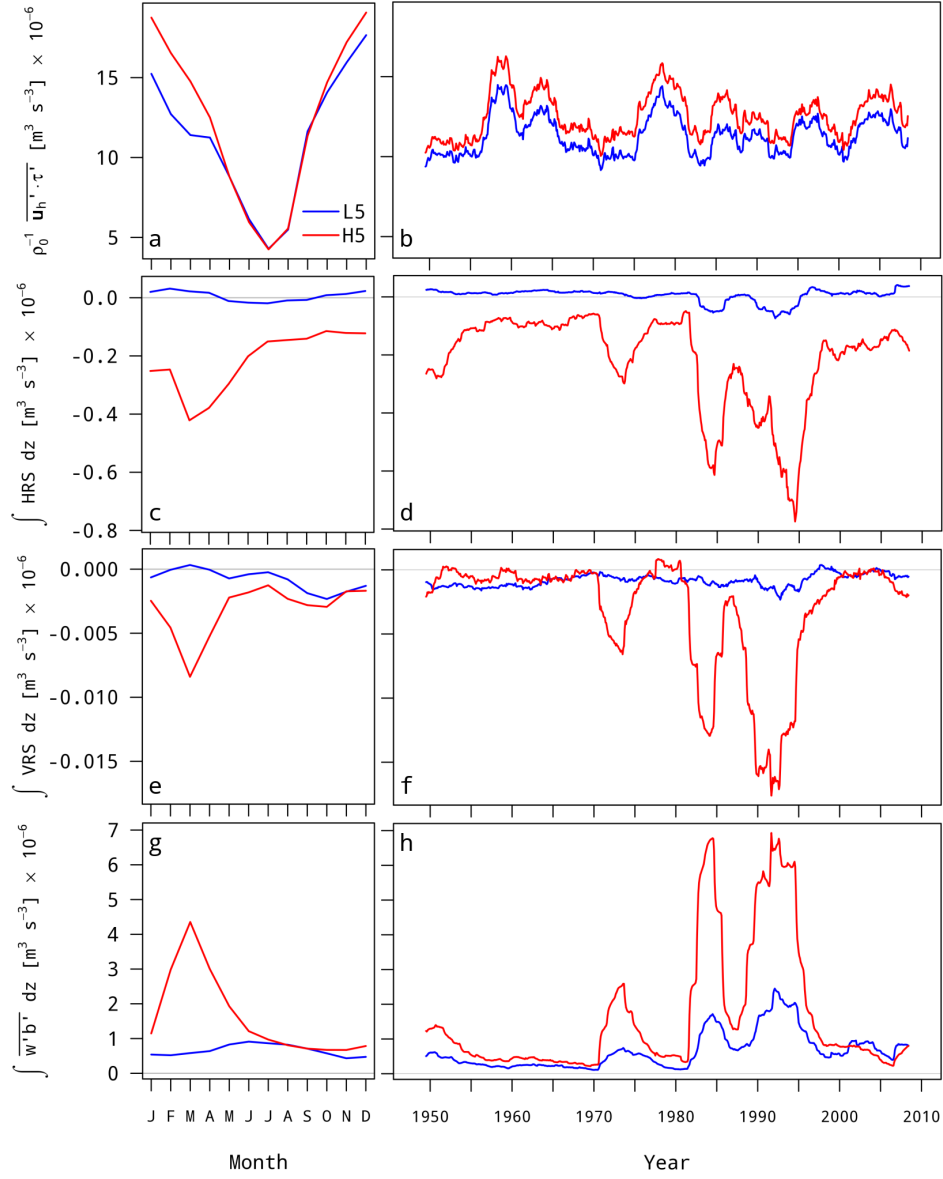


**Figure 5.5:** Average (1948-2009) annual cycle (left) and decadal evolution (right) of eddy wind work at the sea surface ( $F_e K_e$ , eq. 5.6, a-b) and depth-integrated barotropic horizontal ( $HRS$ , eq. 5.7, c-d) and vertical ( $VRS$ , eq. 5.8, e-f) Reynolds stresses and baroclinic instabilities ( $P_e K_e$ , eq. 5.9, g-h, all in  $10^{-6} \text{ m}^3 \text{ s}^{-3}$ ) of low- (blue) and high-resolution (red) models, area-averaged over the LS interior (index area shown in Fig. 4.1). A positive term generates EKE at the expense of the mean flow. A 3-year running mean is applied to the decadal time series. Note the different scales.

be a potential explanation for the obtained  $-2$  slope in the quasi-QG regime (Callies and Ferrari, 2013). Here, the spatial range of enhanced turbulence

is restricted to scales rather larger than the  $O(1-10)$  km associated with the submesoscale. The spectral slopes fall off steeper when increasingly smaller scales are included, yielding the quasi-QG regime (red lines in Fig. 5.3).

Intensified turbulence contributes to the kinetic energy cascade and leads to higher energy levels to during winter compared to summer (solid lines in Fig. 5.2). Baroclinic instabilities are identified as the main driver of this additional EKE generation during winter, representing by far the largest internal contribution (Fig. 5.4 and 5.5). Wind anomalies excited at the sea surface provide more EKE (Renault et al., 2016), however, these contributions are nearly equal in the low- and high-resolution model solutions. Barotropic instabilities associated with horizontal and vertical shear, in contrast, are orders of magnitude smaller than the baroclinic contribution, likely due to the homogenized mixed layer with small, especially vertical, shear. The baroclinic instabilities yield large vertical velocities during deep convection, converting potential energy stored in steep isopycnals into EKE. As reported, these instabilities occur on the order of  $O(1-10)$  km (Haine and Marshall, 1998; Boccaletti et al., 2007). Here, however, the range of the shallower winter kinetic energy spectra with slopes approaching  $-2$  during phases of strong convection (Fig. 5.3 b) is located between 25 and 100 km. Since MLIs scale with the actual MLD (Callies et al., 2015), instabilities grow large in deep mixed layers. Hence, since the modeled winter MLD is generally rather deep (in both models, Fig. 3.17), MLIs may grow large and yield amplifications in the kinetic energy spectrum at scales on the order of  $O(10-100)$  km.

Through the coarser resolution ( $\sim 20$  km) in the low-resolution model, these aspects are not seen as the kinetic energy spectrum falls off much steeper due to missing baroclinic instability. Even on large scales on order of  $O(100)$  km, where the geostrophic regime yields surface-QG turbulence in the high-resolution model as well as in geostrophic altimeter derived velocities (Fig. 5.2), the circulation is not energetic enough. In addition, the broad low-resolution boundary current as shown in Fig. 4.1 e) may imprint on the EKE budget as indicated by the weak but positive *HRS* contribution. Although the AVISO data and the low-resolution model exhibit approximately the same horizontal resolution, spatial filtering during the gridding of along track data likely removes energy which leads to the steeper spectrum (Callies and Ferrari, 2013). Moreover, the Labrador Sea interior may represent a distinct dynamic regime, since spectral slopes of  $-3$  were reported by Wang et al. (2010); Khatri et al. (2018) for the Gulf Stream. This, in turn, could be related to the large

ageostrophic velocities whose imprint on the sea surface height field may not be captured by altimetry.

## 5.4 Conclusions

EKE budget analyses of the high-resolution FESOM ocean model supports recent findings that submesoscale baroclinic mixed layer instabilities (MLIs) are essential for restratifying the water column after convection. Baroclinic instability induced through large ageostrophic velocities draws turbulent potential energy from steep isopycnals, which thereby flatten.

This represents an important process since the large vertical tracer exchange between the deep and surface waters may yield different distributions of nutrients which could e.g. affect the oceanic primary production ([Lévy et al., 2010](#)). However, the Labrador Sea is a region of very deep convection and prone to numerical errors due to steep bottom slopes. Thereby, FESOMs ability of local mesh refinement enables us to identify the involved dynamics across all spatial scales. A multi-resolution sensitivity study would be the next step in order to relate instabilities from the mesoscale and the submesoscale.

## 6 Conclusions & Outlook

This study investigated the effects of a high spatial ocean model resolution on the order of the first baroclinic Rossby radius of deformation on the modeled North Atlantic dynamics and thermodynamics in comparison to a  $\sim 1^\circ$  control run. The following conclusions were made, from large to small spatial scales:

- The high-resolution ocean model needs a considerably longer time to adjust from initial conditions in order to reach a quasi-equilibrium mean state, likely through long baroclinic Rossby waves that affect the model spinup adjustment on basin scales.
- Vivid interactions between the boundary current and mesoscale eddies contribute a significant amount of horizontal tracer fluxes. These fluctuations were shown to contribute to restratification after deep convection events in the Labrador Sea.
- Turbulent kinetic energy exchanged across spatial scales from 5 to 300 km yields an additional way of model adjustment to forcing. Large ageostrophic velocities were seen to add an important contribution to baroclinically unstable conditions.

These aspects must be studied in greater detail in future to obtain better numerical representations of the world ocean. For this, research programs should focus on improved physical parameterizations of low-resolution ocean (and climate) models. Increasing the resolution certainly is not the only route of progress. Moreover, increasing the resolution on a large scale as done in this study imposes difficulties in separating effects on different spatial and temporal scales. The transition from the low- to the high-resolution mesh, for example in terms of the used 3D mesh nodes (Tab. 2.1), yields an increase of the degrees of freedom of factor  $\sim 30$ , which certainly induces ambiguities. Moreover, all derived results and conclusions only hold in an ocean-only world. Consideration of global coupled climate models, and, most importantly, real observations, is crucial for understanding.



## Bibliography

- Abe, H., Y. Tanimoto, T. Hasegawa, and N. Ebuchi, 2016: Oceanic Rossby Waves over Eastern Tropical Pacific of Both Hemispheres Forced by Anomalous Surface Winds after Mature Phase of ENSO. *JPO*, **46** (11), 3397–3414, doi:10.1175/JPO-D-15-0118.1.
- Alvera-Azcárate, A., A. Barth, and R. H. Weisberg, 2009: The Surface Circulation of the Caribbean Sea and the Gulf of Mexico as Inferred from Satellite Altimetry. *JPO*, **39** (3), 640–657, doi:10.1175/2008JPO3765.1.
- Amante, C., and B. W. Eakins, 2009: ETOPO1 1 Arc-Minute Global Relief Model: Procedures, Data Sources and Analysis. NOAA Technical Memorandum NESDIS NGDC-24, NOAA. doi:10.7289/V5C8276M, [July 15 2015].
- Batchelor, G. K., 2000: *An Introduction to Fluid Dynamics*. Cambridge University Press, 615 pp.
- Bierdel, L., P. Friederichs, and S. Bentzien, 2012: Spatial kinetic energy spectra in the convection-permitting limited-area nwp model cosmo-de. *Meteorologische Zeitschrift*, **21** (3), 245–258, doi:10.1127/0941-2948/2012/0319.
- Blumen, W., 1978: Uniform Potential Vorticity Flow: Part I. Theory of Wave Interactions and Two-Dimensional Turbulence. *Journal of the Atmospheric Sciences*, **35** (5), 774–783, doi:10.1175/1520-0469(1978)035<0774:UPVFPI>2.0.CO;2.
- Boccaletti, G., R. Ferrari, and B. Fox-Kemper, 2007: Mixed Layer Instabilities and Restratification. *Journal of Physical Oceanography*, **37** (9), 2228–2250, doi:10.1175/JPO3101.1.
- Brandt, P., A. Funk, L. Czeschel, C. Eden, and C. W. Böning, 2007: Ventilation and Transformation of Labrador Sea Water and Its Rapid Export in the Deep Labrador Current. *J. Phys. Oceanogr.*, **37** (4), 946–961, doi:10.1175/JPO3044.1.
- Brannigan, L., D. P. Marshall, A. Naveira-Garabato, and A. G. Nurser, 2015: The seasonal cycle of submesoscale flows. *Ocean Modelling*, **92**, 69 – 84, doi:https://doi.org/10.1016/j.ocemod.2015.05.002.
- Bryan, F. O., M. W. Hecht, and R. D. Smith, 2007: Resolution convergence and sensitivity studies with North Atlantic circulation models. Part I: The western boundary current system. *Ocean Modelling*, **16** (3), 141–159, doi:10.1016/j.ocemod.2006.08.005.

- Callies, J., and R. Ferrari, 2013: Interpreting Energy and Tracer Spectra of Upper-Ocean Turbulence in the Submesoscale Range (1–200 km). *Journal of Physical Oceanography*, **43** (11), 2456–2474, doi:10.1175/JPO-D-13-063.1.
- Callies, J., R. Ferrari, J. M. Klymak, and J. Gula, 2015: Seasonality in submesoscale turbulence. *Nature Communications*, **6** (6862), doi:10.1038/ncomms7862.
- Capet, X., P. Klein, B. L. Hua, G. Lapeyre, and J. C. McWilliams, 2008: Surface kinetic energy transfer in surface quasi-geostrophic flows. *Journal of Fluid Mechanics*, **604**, 165–174, doi:10.1017/S0022112008001110.
- Castro, C. L., R. A. Pielke, and G. Leoncini, 2005: Dynamical downscaling: Assessment of value retained and added using the regional atmospheric modeling system (rams). *Journal of Geophysical Research: Atmospheres*, **110** (D5), doi:10.1029/2004JD004721.
- Cavalieri, D. J., C. L. Parkinson, P. Gloersen, and H. J. Zwally, 1996: Sea Ice Concentrations from Nimbus-7 SMMR and DMSP SSM/I-SSMIS Passive Microwave Data, Version 1. Boulder, Colorado USA. NASA National Snow and Ice Data Center Distributed Active Archive Center. doi: 10.5067/8GQ8LZQVL0VL, updated yearly, [July 15 2015].
- Chanut, J., B. Barnier, W. Large, L. Debreu, T. Penduff, J. M. Molines, and P. Mathiot, 2008: Mesoscale Eddies in the Labrador Sea and Their Contribution to Convection and Restratification. *J. Phys. Oceanogr.*, **38** (8), 1617–1643, doi:10.1175/2008JPO3485.1.
- Charney, J. G., 1971: Geostrophic Turbulence. *Journal of the Atmospheric Sciences*, **28** (6), 1087–1095, doi:10.1175/1520-0469(1971)028<1087:GT>2.0.CO;2.
- Chelton, D. B., R. A. deSzoeke, M. G. Schlax, K. E. Naggar, and N. Siwertz, 1998: Geographical Variability of the First Baroclinic Rossby Radius of Deformation. *J. Phys. Oceanogr.*, **28** (3), 433–460, doi:10.1175/1520-0485(1998)028<0433:GVOTFB>2.0.CO;2.
- Chelton, D. B., and M. G. Schlax, 1996: Global Observations of Oceanic Rossby Waves. *Science*, **272** (5259), 234–238, doi:10.1126/science.272.5259.234.
- Chelton, D. B., M. G. Schlax, and R. M. Samelson, 2011: Global observations of nonlinear mesoscale eddies. *Progress in Oceanography*, **91** (2), 167–216, doi:10.1016/j.pocean.2011.01.002.

- Cherniawsky, J., and L. Mysak, 1989: Baroclinic adjustment in coarse-resolution numerical ocean models. *Atmos.–Ocean*, **27** (2), 306–326, doi:10.1080/07055900.1989.9649338.
- Clément, L., E. Frajka-Williams, Z. B. Szuts, and S. A. Cunningham, 2014: Vertical structure of eddies and rossby waves, and their effect on the atlantic meridional overturning circulation at 26.5°N. *J. Geophys. Res. Oceans*, **119** (9), 6479–6498, doi:10.1002/2014JC010146.
- Courtois, P., X. Hu, C. Pennelly, P. Spence, and P. G. Myers, 2017: Mixed layer depth calculation in deep convection regions in ocean numerical models. *Ocean Modelling*, **120**, 60–78, doi:10.1016/j.ocemod.2017.10.007.
- Dai, A., T. Qian, K. E. Trenberth, and J. D. Milliman, 2009: Changes in continental freshwater discharge from 1948 to 2004. *Journal of Climate*, **22** (10), 2773–2792, doi:10.1175/2008JCLI2592.1.
- Danabasoglu, G., J. C. McWilliams, and P. R. Gent, 1994: The role of mesoscale tracer transports in the global ocean circulation. *Science*, **264** (5162), 1123–1126, doi:10.1126/science.264.5162.1123.
- Danabasoglu, G., J. C. McWilliams, and W. G. Large, 1996: Approach to Equilibrium in Accelerated Global Oceanic Models. *J. Climate*, **9** (5), 1092–1110, doi:10.1175/1520-0442(1996)009<1092:ATEIAG>2.0.CO;2.
- Danabasoglu, G., and Coauthors, 2014: North Atlantic simulations in Coordinated Ocean-ice Reference Experiments phase II (CORE-II). Part I: Mean states. *Ocean Modelling*, **73**, 76–107, doi:10.1016/j.ocemod.2013.10.005.
- Danabasoglu, G., and Coauthors, 2016: North Atlantic simulations in Coordinated Ocean-ice Reference Experiments phase II (CORE-II). Part II: Interannual to decadal variability. *Ocean Modelling*, **97**, 65–90, doi:10.1016/j.ocemod.2015.11.007.
- Danek, C., P. Scholz, and G. Lohmann, 2019: Effects of High Resolution and Spinup Time on Modeled North Atlantic Circulation. *Journal of Physical Oceanography*, **49** (5), 1159–1181, doi:10.1175/JPO-D-18-0141.1.
- Danilov, S., 2013: Ocean modeling on unstructured meshes. *Ocean Modelling*, **69**, 195 – 210, doi:https://doi.org/10.1016/j.ocemod.2013.05.005.
- Danilov, S., G. Kivman, and J. Schröter, 2004: A finite-element ocean model: principles and evaluation. *Ocean Modelling*, **6** (2), 125–150, doi:10.1016/S1463-5003(02)00063-X.

- Danilov, S., G. Kivman, and J. Schröter, 2005: Evaluation of an eddy-permitting finite-element ocean model in the north atlantic. *Ocean Modelling*, **10**, 35–49.
- D’Asaro, E., C. Lee, L. Rainville, R. Harcourt, and L. Thomas, 2011: Enhanced Turbulence and Energy Dissipation at Ocean Fronts. *Science*, **332 (6027)**, 318–322, doi:10.1126/science.1201515.
- de Jong, M. F., A. S. Bower, and H. H. Furey, 2014: Two Years of Observations of Warm-Core Anticyclones in the Labrador Sea and Their Seasonal Cycle in Heat and Salt Stratification. *Journal of Physical Oceanography*, **44 (2)**, 427–444, doi:10.1175/JPO-D-13-070.1.
- de Jong, M. F., A. S. Bower, and H. H. Furey, 2016: Seasonal and Inter-annual Variations of Irminger Ring Formation and Boundary–Interior Heat Exchange in FLAME. *Journal of Physical Oceanography*, **46 (6)**, 1717–1734, doi:10.1175/JPO-D-15-0124.1.
- Dukhovskoy, D. S., and Coauthors, 2016: Greenland freshwater pathways in the sub-Arctic seas from model experiments with passive tracers. *Journal of Geophysical Research: Oceans*, **121 (1)**, 877–907, doi:10.1002/2015JC011290.
- Dupont, F., and Coauthors, 2015: A high-resolution ocean and sea-ice modelling system for the Arctic and North Atlantic oceans. *Geoscientific Model Development*, **8 (5)**, 1577–1594, doi:10.5194/gmd-8-1577-2015.
- Eden, C., and C. Böning, 2002: Sources of eddy kinetic energy in the Labrador Sea. *Journal of physical oceanography*, **32 (12)**, 3346–3363.
- Errico, R. M., 1985: Spectra computed from a limited area grid. *Monthly Weather Review*, **113 (9)**, 1554–1562, doi:10.1175/1520-0493(1985)113<1554:SCFALA>2.0.CO;2.
- Fan, J., and I. Gijbels, Eds., 1996: *Local polynomial modelling and its applications, Monographs on Statistics and Applied Probability*, Vol. 66. Chapman & Hall.
- Fofonoff, N. P., and R. C. J. Millard, 1983: *Algorithms for computation of fundamental properties of seawater*. No. 44, Unesco technical papers in marine science, UNESCO.

- Fox-Kemper, B., and R. Ferrari, 2008: Parameterization of mixed layer eddies. part ii: Prognosis and impact. *Journal of Physical Oceanography*, **38** (6), 1166–1179, doi:10.1175/2007JPO3788.1.
- Fox-Kemper, B., R. Ferrari, and R. Hallberg, 2008: Parameterization of Mixed Layer Eddies. Part I: Theory and Diagnosis. *J. Phys. Oceanogr.*, **38** (6), 1145–1165, doi:10.1175/2007JPO3792.1.
- Fox-Kemper, B., R. Ferrari, and J. Pedlosky, 2003: On the Indeterminacy of Rotational and Divergent Eddy Fluxes. *Journal of Physical Oceanography*, **33** (2), 478–483, doi:10.1175/1520-0485(2003)033<0478:OTIORA>2.0.CO;2.
- Frajka–Williams, E., 2015: Estimating the Atlantic overturning at 26°N using satellite altimetry and cable measurements. *Geophys. Res. Lett.*, **42** (9), 3458–3464, doi:10.1002/2015GL063220.
- Frenger, I., N. Gruber, R. Knutti, and M. Münnich, 2013: Imprint of Southern Ocean eddies on winds, clouds and rainfall. *Nature Geoscience*, **6** (608), doi:10.1038/ngeo1863.
- Frisch, U., 1995: *Turbulence: The Legacy of A.N. Kolmogorov*. Cambridge University Press.
- Ganachaud, A., and C. Wunsch, 2003: Large-Scale Ocean Heat and Freshwater Transports during the World Ocean Circulation Experiment. *J. Climate*, **16** (4), 696–705, doi:10.1175/1520-0442(2003)016<0696:LSOHAF>2.0.CO;2.
- Garcia-Quintana, Y., P. Courtois, X. Hu, C. Pennelly, D. Kieke, and P. G. Myers, 2019: Sensitivity of Labrador Sea Water Formation to Changes in Model Resolution, Atmospheric Forcing, and Freshwater Input. *Journal of Geophysical Research: Oceans*, **124** (3), 2126–2152, doi:10.1029/2018JC014459.
- Gelderloos, R., C. A. Katsman, and S. S. Drijfhout, 2011: Assessing the Roles of Three Eddy Types in Restratifying the Labrador Sea after Deep Convection. *Journal of Physical Oceanography*, **41** (11), 2102–2119, doi:10.1175/JPO-D-11-054.1.
- Gent, P. R., and J. C. McWilliams, 1990: Isopycnal Mixing in Ocean Circulation Models. *J. Phys. Oceanogr.*, **20** (1), 150–155, doi:10.1175/1520-0485(1990)020<0150:IMIOCM>2.0.CO;2.
- Gill, A. E., 1982: *Atmosphere–Ocean Dynamics*. Academic Press.

- Good, S. A., M. J. Martin, and N. A. Rayner, 2013: EN4: Quality controlled ocean temperature and salinity profiles and monthly objective analyses with uncertainty estimates. *J. Geophys. Res. Oceans*, **118**, doi:10.1002/2013JC009067.
- Griffies, S. M., 1998: The Gent–McWilliams Skew Flux. *Journal of Physical Oceanography*, **28** (5), 831–841, doi:10.1175/1520-0485(1998)028<0831:TGMSF>2.0.CO;2.
- Griffies, S. M., and A. J. Adcroft, 2008: Formulating the Equations of Ocean Models. *Ocean Modeling in an Eddying Regime*, Hecht, M. W. and Hasumi, H., 281–317, doi:10.1029/177GM18.
- Griffies, S. M., A. Gnanadesikan, R. C. Pacanowski, V. D. Larichev, J. K. Dukowicz, and R. D. Smith, 1998: Isonutral Diffusion in a z-Coordinate Ocean Model. *J. Phys. Oceanogr.*, **28** (5), 805–830, doi:10.1175/1520-0485(1998)028<0805:IDIAZC>2.0.CO;2.
- Griffies, S. M., M. Winton, B. Samuels, G. Danabasoglu, S. G. Yeager, S. J. Marsland, H. Drange, and M. Bentsen, 2012: Datasets and protocol for the CLIVAR WGOMD Coordinated Ocean-sea ice Reference Experiments (COREs). WCRP Report No. 21/2012.
- Griffies, S. M., and Coauthors, 2015: Impacts on Ocean Heat from Transient Mesoscale Eddies in a Hierarchy of Climate Models. *J. Climate*, **28** (3), 952–977, doi:10.1175/JCLI-D-14-00353.1.
- Haarsma, R. J., and Coauthors, 2016: High Resolution Model Intercomparison Project (HighResMIP v1.0) for CMIP6. *Geoscientific Model Development*, **9** (11), 4185–4208, doi:10.5194/gmd-9-4185-2016.
- Haine, T. W. N., and J. Marshall, 1998: Gravitational, Symmetric, and Baroclinic Instability of the Ocean Mixed Layer. *Journal of Physical Oceanography*, **28** (4), 634–658, doi:10.1175/1520-0485(1998)028<0634:GSABIO>2.0.CO;2.
- Han, Z., F. Luo, S. Li, Y. Gao, T. Furevik, and L. Svendsen, 2016: Simulation by CMIP5 models of the atlantic multidecadal oscillation and its climate impacts. *Advances in Atmospheric Sciences*, **33** (12), 1329–1342, doi:10.1007/s00376-016-5270-4.
- He, Y.-C., H. Drange, Y. Gao, and M. Bentsen, 2016: Simulated Atlantic Meridional Overturning Circulation in the 20th century with an ocean model

- forced by reanalysis-based atmospheric data sets. *Ocean Modelling*, **100**, 31–48, doi:10.1016/j.ocemod.2015.12.011.
- Heuzé, C., 2017: North Atlantic deep water formation and AMOC in CMIP5 models. *Ocean Science*, **13** (4), 609–622, doi:10.5194/os-13-609-2017.
- Hewitt, H. T., and Coauthors, 2016: The impact of resolving the Rossby radius at mid-latitudes in the ocean: results from a high-resolution version of the Met Office GC2 coupled model. *Geoscientific Model Development*, **9** (10), 3655–3670, doi:10.5194/gmd-9-3655-2016.
- Holte, J., and L. Talley, 2009: A New Algorithm for Finding Mixed Layer Depths with Applications to Argo Data and Subantarctic Mode Water Formation. *J. Atmos. Oceanic Technol.*, **26** (9), 1920–1939, doi:10.1175/2009JTECHO543.1.
- Hurlburt, H. E., and P. J. Hogan, 2000: Impact of  $1/8^\circ$  to  $1/64^\circ$  resolution on Gulf Stream model–data comparisons in basin-scale subtropical Atlantic Ocean models. *Dyn. Atmos. Oceans*, **32** (3), 283–329, doi:10.1016/S0377-0265(00)00050-6.
- Hurrell, J. H., 2003: NAO Index Data. *NAO Index Data provided by the Climate Analysis Section, NCAR, Boulder, USA*, URL <https://climatedataguide.ucar.edu/climate-data/hurrell-north-atlantic-oscillation-nao-index-station-based>.
- Hátún, H., C. C. Eriksen, and P. B. Rhines, 2007: Buoyant Eddies Entering the Labrador Sea Observed with Gliders and Altimetry. *Journal of Physical Oceanography*, **37** (12), 2838–2854, doi:10.1175/2007JPO3567.1.
- IOC, SCOR, and IAPSO, 2010: *The international thermodynamic equation of seawater – 2010: Calculation and use of thermodynamic properties*. No. 56, Intergovernmental Oceanographic Commission, Manuals and Guides, UNESCO.
- Ionita, M., P. Scholz, G. Lohmann, M. Dima, and M. Prange, 2016: Linkages between atmospheric blocking, sea ice export through Fram Strait and the Atlantic Meridional Overturning Circulation. *Scientific Reports*, **6** (32881), 1–10, doi:10.1038/srep32881.
- Iovino, D., S. Masina, A. Storto, A. Cipollone, and V. N. Stepanov, 2016: A  $1/16^\circ$  eddy simulation of the global NEMO sea-ice–ocean system. *Geoscientific Model Development*, **9** (8), 2665–2684, doi:10.5194/gmd-9-2665-2016.

- Jayne, S. R., and J. Marotzke, 2002: The Oceanic Eddy Heat Transport. *Journal of Physical Oceanography*, **32** (12), 3328–3345, doi:10.1175/1520-0485(2002)032<3328:TOEHT>2.0.CO;2.
- Jochumsen, K., M. Moritz, N. Nunes, D. Quadfasel, K. M. H. Larsen, B. Hansen, H. Valdimarsson, and S. Jonsson, 2017: Revised transport estimates of the Denmark Strait overflow. *J. Geophys. Res. Oceans*, **122**, doi:10.1002/2017JC012803.
- Johns, W. E., and Coauthors, 2011: Continuous, Array-Based Estimates of Atlantic Ocean Heat Transport at 26.5°N. *J. Climate*, **24** (10), 2429–2449, doi:10.1175/2010JCLI3997.1.
- Jones, H., and J. Marshall, 1997: Restratification after Deep Convection. *Journal of Physical Oceanography*, **27** (10), 2276–2287, doi:10.1175/1520-0485(1997)027<2276:RADC>2.0.CO;2.
- Josey, S. A., 2003: Changes in the heat and freshwater forcing of the eastern mediterranean and their influence on deep water formation. *JGR*, **108**, 1–15.
- Karspeck, A. R., and Coauthors, 2017: Comparison of the Atlantic meridional overturning circulation between 1960 and 2007 in six ocean reanalysis products. *Climate Dyn.*, **49** (3), 957–982, doi:10.1007/s00382-015-2787-7.
- Kawasaki, T., and H. Hasumi, 2014: Effect of freshwater from the west greenland current on the winter deep convection in the labrador sea. *Ocean Modelling*, **75**, 51 – 64, doi:https://doi.org/10.1016/j.ocemod.2014.01.003.
- Kessler, W. S., 1990: Observations of long Rossby waves in the northern tropical Pacific. *Journal of Geophysical Research: Oceans*, **95** (C4), 5183–5217, doi:10.1029/JC095iC04p05183.
- Khatri, H., J. Sukhatme, A. Kumar, and M. K. Verma, 2018: Surface Ocean Enstrophy, Kinetic Energy Fluxes, and Spectra From Satellite Altimetry. *Journal of Geophysical Research: Oceans*, **123** (5), 3875–3892, doi:10.1029/2017JC013516.
- Kieke, D., M. Rhein, L. Stramma, W. M. Smethie, J. L. Bullister, and D. A. LeBel, 2007: Changes in the pool of Labrador Sea Water in the subpolar North Atlantic. *Geophys. Res. Lett.*, **34** (6), doi:10.1029/2006GL028959.
- LaCasce, J. H., 2012: Surface Quasigeostrophic Solutions and Baroclinic Modes with Exponential Stratification. *Journal of Physical Oceanography*, **42** (4), 569–580, doi:10.1175/JPO-D-11-0111.1.

- Lagrange, J. L., 1781: Mémoire sur la théorie du mouvement des fluides. (*Œuvres des Lagrange*, No. 4, Nouveaux Mémoires de l'Académie Royale des Sciences et Belles-Lettres, Serret, M. J.-A, 695–748.
- Lamb, H., 1916: *Hydrodynamics*. Cambridge University Press, 706 pp.
- Lapeyre, G., and P. Klein, 2006: Dynamics of the Upper Oceanic Layers in Terms of Surface Quasigeostrophy Theory. *Journal of Physical Oceanography*, **36** (2), 165–176, doi:10.1175/JPO2840.1.
- Lapeyre, G., P. Klein, and B. L. Hua, 2006: Oceanic Restratification Forced by Surface Frontogenesis. *Journal of Physical Oceanography*, **36** (8), 1577–1590, doi:10.1175/JPO2923.1.
- Laprise, R., 2003: Resolved scales and nonlinear interactions in limited-area models. *Journal of the Atmospheric Sciences*, **60** (5), 768–779, doi:10.1175/1520-0469(2003)060<0768:RSANII>2.0.CO;2.
- Large, W. G., J. C. McWilliams, and S. C. Doney, 1994: Oceanic vertical mixing: A review and a model with a nonlocal boundary layer parameterization. *Rev. Geophys.*, **32** (4), 363–403, doi:10.1029/94RG01872.
- Large, W. G., and S. G. Yeager, 2004: Diurnal to decadal global forcing for ocean and sea-ice models: The data sets and flux climatologies. NCAR Technical Note NCAR/TN-460+STR. doi:10.5065/D6KK98Q6.
- Large, W. G., and S. G. Yeager, 2009: The global climatology of an interannually varying air–sea flux data set. *J. Climate*, **33** (341), doi:10.1007/s00382-008-0441-3.
- Lilly, D. K., and E. L. Petersen, 1983: Aircraft measurements of atmospheric kinetic energy spectra. *Tellus A*, **35A** (5), 379–382, doi:10.1111/j.1600-0870.1983.tb00212.x.
- Lilly, J. M., P. B. Rhines, F. Schott, K. Lavender, J. R. N. Lazier, and U. Send, 2003: Observations of the Labrador Sea Eddy Field. *Process in Oceanography*, **59** (1), 75–176.
- Lindborg, E., 1999: Can the atmospheric kinetic energy spectrum be explained by two-dimensional turbulence? *Journal of Fluid Mechanics*, **388**, 259–288, doi:10.1017/S0022112099004851.
- Locarnini, R. A., and Coauthors, 2013: *World Ocean Atlas 2013, Volume 1: Temperature*. S. Levitus. Ed., A. Mishonov technical editor, NOAA Atlas NESDIS 73.

- Lohmann, K., H. Drange, and M. Bentsen, 2009: Response of the North Atlantic subpolar gyre to persistent North Atlantic oscillation like forcing. *Climate Dyn.*, **32** (2), 273–285, doi:10.1007/s00382-008-0467-6.
- Lorenz, E. N., 1955: Available Potential Energy and the Maintenance of the General Circulation. *Tellus*, **7** (2), 157–167, doi:10.1111/j.2153-3490.1955.tb01148.x.
- Lévy, M., P. Klein, A.-M. Tréguier, D. Iovino, G. Madec, S. Masson, and K. Takahashi, 2010: Modifications of gyre circulation by sub-mesoscale physics. *Ocean Modelling*, **34** (1), 1 – 15, doi:https://doi.org/10.1016/j.ocemod.2010.04.001.
- Marchesiello, P., J. C. McWilliams, and A. Shchepetkin, 2003: Equilibrium structure and dynamics of the California current system. *Journal of Physical Oceanography*, **33** (4), 753–783, doi:10.1175/1520-0485(2003)33<753:ESADOT>2.0.CO;2.
- Marsh, R., D. Desbruyères, J. L. Bamber, B. A. de Cuevas, A. C. Coward, and Y. Aksenov, 2010: Short-term impacts of enhanced Greenland freshwater fluxes in an eddy-permitting ocean model. *Ocean Science*, **6** (3), 749–760, doi:10.5194/os-6-749-2010.
- Marshall, J., C. Hill, L. Perelman, and A. Adcroft, 1997: Hydrostatic, quasi-hydrostatic, and nonhydrostatic ocean modeling. *Journal of Geophysical Research: Oceans*, **102** (C3), 5733–5752, doi:10.1029/96JC02776.
- Marshall, J., and G. Shutts, 1981: A Note on Rotational and Divergent Eddy Fluxes. *Journal of Physical Oceanography*, **11** (12), 1677–1680, doi:10.1175/1520-0485(1981)011<1677:ANORAD>2.0.CO;2.
- Marzocchi, A., J. J.-M. Hirschi, N. P. Holliday, S. A. Cunningham, A. T. Blaker, and A. C. Coward, 2015: The North Atlantic subpolar circulation in an eddy-resolving global ocean model. *J. Mar. Syst.*, **142**, 126–143, doi:10.1016/j.jmarsys.2014.10.007.
- McGeehan, T., and W. Maslowski, 2011: Impact of Shelf–Basin Freshwater Transport on Deep Convection in the Western Labrador Sea. *Journal of Physical Oceanography*, **41** (11), 2187–2210, doi:10.1175/JPO-D-11-01.1.
- McWilliams, J. C., 1998: Oceanic general circulation models. *Ocean Modeling and Parameterization*, E. P. Chassignet, and J. Verron, Eds., NATO Science Series, Vol. 16, Springer Science+Business Media, B.V., 1–44.

- McWilliams, J. C., 2008: The Nature and Consequences of Oceanic Eddies. *Ocean Modeling in an Eddying Regime*, No. 177, Geophysical Monograph Series, M. W. Hecht and H. Hasumi, 5–17.
- Menary, M. B., D. L. R. Hodson, J. I. Robson, R. T. Sutton, R. A. Wood, and J. A. Hunt, 2015: Exploring the impact of CMIP5 model biases on the simulation of North Atlantic decadal variability. *Geophys. Res. Lett.*, **42** (14), 5926–5934, doi:10.1002/2015GL064360.
- Mensa, J. A., Z. Garraffo, A. Griffa, T. M. Özgökmen, A. Haza, and M. Veneziani, 2013: Seasonality of the submesoscale dynamics in the gulf stream region. *Ocean Dynamics*, **63** (8), 923–941, doi:10.1007/s10236-013-0633-1.
- Monterey, G. I., and L. M. deWitt, 2000: Seasonal variability of global mixed layer depth from WOD98 temperature and salinity profiles. NOAA Technical Memorandum NMFS NOAA-TM-NMFS-SWFSC-296, NOAA.
- Nastrom, G. D., and K. S. Gage, 1985: A climatology of atmospheric wavenumber spectra of wind and temperature observed by commercial aircraft. *Journal of the Atmospheric Sciences*, **42** (9), 950–960, doi:10.1175/1520-0469(1985)042<0950:ACOAWS>2.0.CO;2.
- Olbers, D., J. Willebrand, and C. Eden, 2012: *Ocean Dynamics*. Springer, Berlin, Heidelberg, doi:https://doi.org/10.1007/978-3-642-23450-7.
- Ortega, P., J. Robson, R. T. Sutton, and M. B. Andrews, 2017: Mechanisms of decadal variability in the Labrador Sea and the wider North Atlantic in a high-resolution climate model. *Climate Dyn.*, **49** (7), 2625–2647, doi:10.1007/s00382-016-3467-y.
- Oschlies, A., 2002: Improved Representation of Upper-Ocean Dynamics and Mixed Layer Depths in a Model of the North Atlantic on Switching from Eddy-Permitting to Eddy-Resolving Grid Resolution. *J. Phys. Oceanogr.*, **32** (8), 2277–2298, doi:10.1175/1520-0485(2002)032<2277:IROUOD>2.0.CO;2.
- Penduff, T., B. Barnier, W. K. Dewar, and J. J. O’Brien, 2004: Dynamical Response of the Oceanic Eddy Field to the North Atlantic Oscillation: A Model–Data Comparison. *Journal of Physical Oceanography*, **34** (12), 2615–2629, doi:10.1175/JPO2618.1.

- Prater, M. D., 2002: Eddies in the Labrador Sea as Observed by Profiling RAFOS Floats and Remote Sensing. *Journal of Physical Oceanography*, **32** (2), 411–427, doi:10.1175/1520-0485(2002)032<0411:EITLSA>2.0.CO;2.
- Rattan, S., P. G. Myers, A.-M. Treguier, S. Theetten, A. Biastoch, and C. Böning, 2010: Towards an understanding of Labrador Sea salinity drift in eddy-permitting simulations. *Ocean Modelling*, **35** (1), 77–88, doi:10.1016/j.ocemod.2010.06.007.
- Redi, M. H., 1982: Oceanic Isopycnal Mixing by Coordinate Rotation. *J. Phys. Oceanogr.*, **12** (10), 1154–1158, doi:10.1175/1520-0485(1982)012<1154:OIMBCR>2.0.CO;2.
- Renault, L., M. J. Molemaker, J. C. McWilliams, A. F. Shchepetkin, F. Lemarié, D. Chelton, S. Illig, and A. Hall, 2016: Modulation of Wind Work by Oceanic Current Interaction with the Atmosphere. *Journal of Physical Oceanography*, **46** (6), 1685–1704, doi:10.1175/JPO-D-15-0232.1.
- Rhein, M., and Coauthors, 2011: Deep water formation, the subpolar gyre, and the meridional overturning circulation in the subpolar North Atlantic. *Deep Sea Research Part II: Topical Studies in Oceanography*, **58** (17), 1819–1832, doi:10.1016/j.dsr2.2010.10.061.
- Rieck, J. K., 2014: Temporal Variability of Oceanic Eddy Kinetic Energy: A High Resolution Model Analysis. M.S. thesis, Faculty of Mathematics and Natural Sciences, Christian-Albrechts-Universität zu Kiel, 80 pp.
- Robinson, I. S., 2010: *Discovering the Ocean from Space – The unique applications of satellite oceanography*. Springer-Verlag.
- Rykova, T., F. Straneo, and A. S. Bower, 2015: Seasonal and interannual variability of the West Greenland Current System in the Labrador Sea in 1993–2008. *Journal of Geophysical Research: Oceans*, **120** (2), 1318–1332, doi:10.1002/2014JC010386.
- Rykova, T., F. Straneo, J. M. Lilly, and I. Yashayaev, 2009: Irminger current anticyclones in the Labrador sea observed in the hydrographic record, 1990–2004. *Journal of Marine Research*, **67** (3), 361–384, doi:10.1357/002224009789954739.
- Saenko, O. A., F. Dupont, D. Yang, P. G. Myers, I. Yashayaev, and G. C. Smith, 2014: Role of Resolved and Parameterized Eddies in the Labrador Sea

- 
- Balance of Heat and Buoyancy. *Journal of Physical Oceanography*, **44** (12), 3008–3032, doi:10.1175/JPO-D-14-0041.1.
- Sarafanov, A., and Coauthors, 2012: Mean full-depth summer circulation and transports at the northern periphery of the Atlantic Ocean in the 2000s. *J. Geophys. Res. Oceans*, **117** (C1), doi:10.1029/2011JC007572.
- Sasaki, H., P. Klein, B. Qiu, and Y. Sasai, 2014: Impact of oceanic-scale interactions on the seasonal modulation of ocean dynamics by the atmosphere. *Nature Communications*, **5** (5636), doi:10.1038/ncomms6636.
- Scaife, A. A., and Coauthors, 2014: Skillful long-range prediction of European and North American winters. *Geophys. Res. Lett.*, **41** (7), 2514–2519, doi:10.1002/2014GL059637.
- Scholz, P., 2012: A global Finite-Element Sea-Ice ocean model focussed on deep water formation areas: Variability of North Atlantic deep water formation and interannual to decadal climate modes. Ph.D. thesis, University of Bremen, 143 pp.
- Scholz, P., D. Kieke, G. Lohmann, M. Ionita, and M. Rhein, 2014: Evaluation of Labrador Sea Water formation in a global Finite-Element Sea-Ice Ocean Model setup, based on a comparison with observational data. *J. Geophys. Res. Oceans*, **119** (3), 1644–1667, doi:10.1002/2013JC009232.
- Scholz, P., G. Lohmann, Q. Wang, and S. Danilov, 2013: Evaluation of a Finite-Element Sea-Ice Ocean Model (FESOM) set-up to study the interannual to decadal variability in the deep-water formation rates. *Ocean Dynamics*, **63** (4), 347–370, doi:10.1007/s10236-012-0590-0.
- Schourup-Kristensen, V., D. Sidorenko, D. A. Wolf-Gladrow, and C. Völker, 2014: A skill assessment of the biogeochemical model REcoM2 coupled to the Finite Element Sea Ice-Ocean Model (FESOM 1.3). *Geoscientific Model Development*, **7** (6), 2769–2802, doi:10.5194/gmd-7-2769-2014.
- Sein, D. V., and Coauthors, 2017: Ocean Modeling on a Mesh With Resolution Following the Local Rossby Radius. *Journal of Advances in Modeling Earth Systems*, **9**, 1–14, doi:10.1002/2017MS001099.
- Shcherbina, A. Y., E. A. D’Asaro, C. M. Lee, J. M. Klymak, M. J. Molemaker, and J. C. McWilliams, 2013: Statistics of vertical vorticity, divergence, and strain in a developed submesoscale turbulence field. *Geophysical Research Letters*, **40** (17), 4706–4711, doi:10.1002/grl.50919.

- Sidorenko, D., S. Danilov, Q. Wang, A. Huerta-Casas, and J. Schröter, 2009: On computing transports in finite-element models. *Ocean Modelling*, **28** (1), 60 – 65, doi:<https://doi.org/10.1016/j.ocemod.2008.09.001>, the Sixth International Workshop on Unstructured Mesh Numerical Modelling of Coastal, Shelf and Ocean Flows.
- Sidorenko, D., Q. Wang, S. Danilov, and J. Schröter, 2011: FESOM under coordinated ocean-ice reference experiment forcing. *Ocean Dynamics*, **61** (7), 881–890, doi:[10.1007/s10236-011-0406-7](https://doi.org/10.1007/s10236-011-0406-7).
- Skamarock, W. C., 2004: Evaluating mesoscale nwp models using kinetic energy spectra. *Monthly Weather Review*, **132** (12), 3019–3032, doi:[10.1175/MWR2830.1](https://doi.org/10.1175/MWR2830.1).
- Smagorinsky, J., 1963: General Circulation Experiments with the Primitive Equations. *Mon. Wea. Rev.*, **91** (3), 99–164, doi:[10.1175/1520-0493\(1963\)091<0099:GCEWTP>2.3.CO;2](https://doi.org/10.1175/1520-0493(1963)091<0099:GCEWTP>2.3.CO;2).
- Smeed, D., G. McCarthy, D. Rayner, B. Moat, W. Johns, M. Baringer, and C. Meinen, 2017: Atlantic meridional overturning circulation observed by the RAPID-MOCHA-WBTS (RAPID-Meridional Overturning Circulation and Heatflux Array-Western Boundary Time Series) array at 26N from 2004 to 2017. British Oceanographic Data Centre - Natural Environment Research Council, UK. doi:[10.5285/5acfd143-1104-7b58-e053-6c86abc0d94b](https://doi.org/10.5285/5acfd143-1104-7b58-e053-6c86abc0d94b).
- Spall, M. A., 2004: Boundary Currents and Watermass Transformation in Marginal Seas\*. *Journal of Physical Oceanography*, **34** (5), 1197–1213.
- Stammer, D., 1997: Global characteristics of ocean variability estimated from regional TOPEX/POSEIDON altimeter measurements. *Journal of Physical Oceanography*, **27** (8), 1743–1769.
- Stammer, D., and C. Wunsch, 1999: Temporal changes in eddy energy of the oceans. *Deep Sea Research Part II: Topical Studies in Oceanography*, **46** (1), 77 – 108, doi:[https://doi.org/10.1016/S0967-0645\(98\)00106-4](https://doi.org/10.1016/S0967-0645(98)00106-4).
- Steele, M., R. Morley, and W. Ermold, 2001: PHC: A Global Ocean Hydrography with a High-Quality Arctic Ocean. *J. Climate*, **14** (9), 2079–2087, doi:[10.1175/1520-0442\(2001\)014<2079:PAGOHW>2.0.CO;2](https://doi.org/10.1175/1520-0442(2001)014<2079:PAGOHW>2.0.CO;2).
- Stewart, K., A. Hogg, S. Griffies, A. Heerdegen, M. Ward, P. Spence, and M. England, 2017: Vertical resolution of baroclinic modes in global ocean models. *Ocean Modelling*, **113**, 50–65, doi:<https://doi.org/10.1016/j.ocemod.2017.03.012>.

- 
- Stokes, G. G., 1845: On the Theories of the Internal friction of Fluids in Motion, and of the Equilibrium and Motion of Elastic Solids. *Transactions of the Cambridge Philosophical Society*, **8**, 287–305.
- Straneo, F., 2006: Heat and Freshwater Transport through the Central Labrador Sea\*. *Journal of Physical Oceanography*, **36** (4), 606–628.
- Talandier, C., and Coauthors, 2014: Improvements of simulated Western North Atlantic current system and impacts on the AMOC. *Ocean Modelling*, **76**, 1–19, doi:10.1016/j.ocemod.2013.12.007.
- Timmermann, R., S. Danilov, J. Schröter, C. Böning, D. Sidorenko, and K. Rollenhagen, 2009: Ocean circulation and sea ice distribution in a finite element global sea ice-ocean model. *Ocean Modelling*, **27** (3), 114–129, doi:10.1016/j.ocemod.2008.10.009.
- Treguier, A. M., S. Theetten, E. P. Chassignet, T. Penduff, R. Smith, L. Talley, J. O. Beismann, and C. Böning, 2005: The North Atlantic Subpolar Gyre in Four High-Resolution Models. *J. Phys. Oceanogr.*, **35** (5), 757–774, doi:10.1175/JPO2720.1.
- Vallis, G. K., 2017: *Atmospheric and Oceanic Fluid Dynamics – Fundamentals and Large-Scale Circulation*. 2nd ed., Cambridge University Press.
- von Storch, J.-S., C. Eden, I. Fast, H. Haak, D. Hernández-Deckers, E. Maier-Reimer, J. Marotzke, and D. Stammer, 2012: An Estimate of the Lorenz Energy Cycle for the World Ocean Based on the STORM/NCEP simulation. *Journal of Physical Oceanography*, **42** (12), 2185–2205, doi:10.1175/JPO-D-12-079.1.
- von Storch, J.-S., H. Sasaki, and J. Marotzke, 2007: Wind-Generated Power Input to the Deep Ocean: An Estimate Using a  $1/10^\circ$  General Circulation Model. *Journal of Physical Oceanography*, **37** (3), 657–672, doi:10.1175/JPO3001.1.
- Wang, C., L. Zhang, S.-K. Lee, L. Wu, and C. R. Mechoso, 2014a: A global perspective on CMIP5 climate model biases. *Nature Climate Change*, **4**, 201–205, doi:10.1038/nclimate2118.
- Wang, Q., 2007: The Finite Element Ocean Model and its aspect of vertical discretization. Ph.D. thesis, University of Bremen, 151 pp.

- Wang, Q., S. Danilov, H. H. Hellmer, and J. Schröter, 2010: Overflow dynamics and bottom water formation in the western Ross Sea: Influence of tides. *J. Geophys. Res. Oceans*, **115** (C10), 1–16, doi:10.1029/2010JC006189.
- Wang, Q., S. Danilov, and J. Schröter, 2008: Finite element ocean circulation model based on triangular prismatic elements, with application in studying the effect of topography representation. *J. Geophys. Res. Oceans*, **113** (C5), 1–21, doi:10.1029/2007JC004482.
- Wang, Q., S. Danilov, D. Sidorenko, R. Timmermann, C. Wekerle, X. Wang, T. Jung, and J. Schröter, 2014b: The Finite Element Sea Ice-Ocean Model (FESOM) v.1.4: formulation of an ocean general circulation model. *Geoscientific Model Development*, **7** (2), 663–693, doi:10.5194/gmd-7-663-2014.
- Wang, Q., C. Wekerle, S. Danilov, X. Wang, and T. Jung, 2018: A 4.5 km resolution Arctic Ocean simulation with the global multi-resolution model FESOM 1.4. *Geoscientific Model Development*, **11** (4), 1229–1255, doi:10.5194/gmd-11-1229-2018.
- Wang, X., Q. Wang, D. Sidorenko, S. Danilov, J. Schröter, and T. Jung, 2012: Long-term ocean simulations in FESOM: evaluation and application in studying the impact of Greenland Ice Sheet melting. *Ocean Dynamics*, **62** (10), 1471–1486, doi:10.1007/s10236-012-0572-2.
- Weese, S. R., and F. O. Bryan, 2006: Climate impacts of systematic errors in the simulation of the path of the North Atlantic Current. *Geophys. Res. Lett.*, **33** (19), doi:10.1029/2006GL027669.
- Wekerle, C., 2013: Dynamics of the Canadian Arctic Archipelago throughflow: A numerical study with a finite element sea ice and ocean model. Ph.D. thesis, University of Bremen, 119 pp.
- Wekerle, C., Q. Wang, W.-J. von Appen, S. Danilov, V. Schourup-Kristensen, and T. Jung, 2017: Eddy-resolving simulation of the atlantic water circulation in the fram strait with focus on the seasonal cycle. *Journal of Geophysical Research: Oceans*, **122** (11), 8385–8405, doi:10.1002/2017JC012974.
- Wekerle, C., W. Wang, S. Danilov, T. Jung, and J. Schröter, 2013: The Canadian Arctic Archipelago throughflow in a multiresolution global model: Model assessment and the driving mechanism of interannual variability. *J. Geophys. Res. Oceans*, **118** (9), 4525–4541, doi:10.1002/jgrc.20330.

- White, L., V. Legat, and E. Deleersnijder, 2008: Tracer Conservation for Three-Dimensional, Finite-Element, Free-Surface, Ocean Modeling on Moving Prismatic Meshes. *Monthly Weather Review*, **136** (2), 420–442, doi:10.1175/2007MWR2137.1.
- Willis, J. K., 2010: Can in situ floats and satellite altimeters detect long-term changes in Atlantic Ocean overturning? *Geophys. Res. Lett.*, **37** (6), doi:10.1029/2010GL042372.
- Wunsch, C., 1997: The Vertical Partition of Oceanic Horizontal Kinetic Energy. *J. Phys. Oceanogr.*, **27** (8), 1770–1794, doi:10.1175/1520-0485(1997)027<1770:TVPOOH>2.0.CO;2.
- Xu, X., H. E. Hurlburt, W. J. Schmitz, R. Zantopp, J. Fischer, and P. J. Hogan, 2013: On the currents and transports connected with the atlantic meridional overturning circulation in the subpolar North Atlantic. *J. Geophys. Res. Oceans*, **118** (1), 502–516, doi:10.1002/jgrc.20065.
- Yashayaev, I., and J. W. Loder, 2016a: Further intensification of deep convection in the Labrador Sea in 2016. *Geophys. Res. Lett.*, **44** (3), 1429–1438, doi:10.1002/2016GL071668.
- Yashayaev, I., and J. W. Loder, 2016b: Recurrent replenishment of Labrador Sea Water and associated decadal-scale variability. *Journal of Geophysical Research: Oceans*, **121** (11), 8095–8114, doi:10.1002/2016JC012046.
- Zdunkowski, W., and A. Bott, 2003: *The Helmholtz theorem*, 214–217. Cambridge University Press, doi:10.1017/CBO9780511805462.014.
- Zentek, R., G. Heinemann, and E. Sachs, 2016: Climatology of wind, kinetic energy, and temperature spectra using a high-resolution climate model for mid-europe. *Journal of Climate*, **29** (3), 963–974, doi:10.1175/JCLI-D-15-0540.1.
- Zhang, R., T. L. Delworth, A. Rosati, W. G. Anderson, K. W. Dixon, H. Lee, and F. Zeng, 2011: Sensitivity of the North Atlantic Ocean Circulation to an abrupt change in the Nordic Sea overflow in a high resolution global coupled climate model. *J. Geophys. Res. Oceans*, **116** (C12), doi:10.1029/2011JC007240.
- Zhang, W., and X.-H. Yan, 2014: Lateral Heat Exchange after the Labrador Sea Deep Convection in 2008. *Journal of Physical Oceanography*, **44** (12), 2991–3007, doi:10.1175/JPO-D-13-0198.1.

- Zhang, W., and X.-H. Yan, 2018: Variability of the Labrador Sea Surface Eddy Kinetic Energy Observed by Altimeter From 1993 to 2012. *Journal of Geophysical Research: Oceans*, **123** (1), 601–612, doi:10.1002/2017JC013508.
- Zhang, Z., W. Wang, and B. Qiu, 2014: Oceanic mass transport by mesoscale eddies. *Science*, **345** (6194), 322–324, doi:10.1126/science.1252418.
- Zweng, M. M., and Coauthors, 2013: *World Ocean Atlas 2013, Volume 2: Salinity*. S. Levitus. Ed., A. Mishonov technical editor, NOAA Atlas NESDIS 74.





## Acknowledgments

I would like to thank Dr. Paul Gierz and Nadezhda Sokolova for their constant support as colleagues and friends, as well as Prof. Gerrit Lohmann for his patience and assistance. Further I am thankful for all the help I received by Dr. Patrick Scholz and Dr. Dmitry Sidorenko to not to get lost in an irregular mesh. In addition, all the colleagues I got in touch with I wish to thank for their open doors and ears so that knowledge can spread across scales.

Software-wise, this work was accomplished nearly without any proprietary products but almost only with open source. I wish to keep that as it is as a way towards the future. Thereby I would like to thank everybody who contributes to open source.

Last but not least, thanks to all the important people around me who share their time with me and never stopped telling me that I will finish on some point. It worked!





